ANL–02/03

ARGONNE NATIONAL LABORATORY
9700 South Cass Avenue
Argonne, Illinois 60439

PRACTICAL SUPERCONDUCTOR DEVELOPMENT FOR ELECTRICAL POWER APPLICATIONS

ANNUAL REPORT FOR FY 2001

U. Balachandran

Contributors:

Y. S. Cha
S. E. Dorris
J. T. Dusek
J. E. Emerson
R. A. Erck
B. L. Fisher
K. C. Goretta
K. E. Gray†
J. R. Hull
Y. Jee
R. E. Koritala
M. Li
J. W. Lucas
B. Ma
V. A. Maroni††
R. L. McDaniel
D. J. Miller†
J.-H. Park
J. J. Picciolo
J. P. Singh

Energy Technology Division

April 2002

Work supported by

U.S. DEPARTMENT OF ENERGY
Office of Energy Efficiency and Renewable Energy

†Materials Science Division.
††Chemical Technology Division.

Contents

Abstract 1

1 Introduction 1

2 Technical Progress in 2000-2001 2

2.1 Y-Ba-Cu-O Coated Conductors 2

2.1.1 Substrate Development for Coated Conductors 2

2.1.2 Pulsed Laser Deposition of YBCO 15

2.1.3 YBCO Films from a Solution Process 26

2.1.4 Current Transport across YBCO Grain Boundaries 38

2.1.5 Characterization of Coated-Conductor Composition and Microstructure 40

2.1.6 Residual Stress Analysis 54

2.1.7 Oxidation of Hastelloy C276 55

2.2 Bi-Pb-Sr-Ca-Cu-O Conductors 59

2.3 Applications and Devices 61

References 71

Patents: 1999-2001 73

Publications: FY2001 74

Figures

1 Experimental arrangement for inclined substrate deposition of MgO on HC substrate 3

2 MgO and MgO pole figures 4

3 X-ray diffraction data for ISD MgO deposited at $\alpha = 55°$ 5

4 Effect of inclination, α, on FWHM values of ϕ- and ω-scans 5

5 SEM photomicrographs of ISD MgO film 7

6 SEM photomicrographs of ISD MgO + e-beam MgO film 8

7 Facet of plane on top of MgO columnar grain and corresponding SAD pattern 9

8 Illustration of ISD MgO growth mechanism due to shadowing effect 10

9 Experimental setup for the inclined substrate deposition of YBCO films directly on Ag substrates 11

10 YSZ pole figure of IBAD YSZ film deposited on HC substrate with 300 eV ion beam energy at substrate temperature of 90°C 13

11 In-plane texture of IBAD YSZ film deposited on HC substrate with 55° bombardment angle, 300 eV beam energy and substrate temperature of 90°C 13

12 Out-of-plane texture of IBAD YSZ film deposited on HC substrate with 55° bombardment angle, 300 ev beam energy, and substrate temperature of 90°C 14

13 FWHM of YSZ ϕ-scan for IBAD YSZ films deposited at various substrate temperatures 14

14 AFM image of top surface of IBAD YSZ film deposited with 300 eV beam energy at 90°C substrate temperature 15

15 Cross-sectional TEM and SAD patterns of IBAD YSZ at four distances from the substrate 16

16 Inductive voltage vs. drive current for YBCO film on LAO 17

17 Plot of current vs. voltage at 77 K for YBCO film on STO crystal 18

18 ϕ-scans of MgO and YBCO showing epitaxial growth 19

19 Critical-temperature transition curve for YBCO film deposited on

21 Secondary electron image of a YBCO film deposited directly on Ag substrate at 755°C with inclination of 55° 21

22 A 2-Θ X-ray diffraction pattern for the YBCO film deposited directly on polished Ag substrate 21

23 Raman spectrum of a YBCO thin film deposited directly on Ag substrate 22

24 YBCO pole figure of a YBCO thin film deposited directly on Ag substrate 22

25 Cross-sectional view of YBCO deposited directly on Ag substrate at 755°C with an inclination of 55° 23

26 TEM EDS spectra of YBCO film deposited directly on Ag and an amorphous layer between Ag and YBCO 24

27 Superconducting transition for YBCO deposited directly on Ag at 755°C, as determined by inductive method 24

28 J_c transition curve in self-field for a YBCO film deposited directly on Ag at 755°C 25

29 Critical transition temperature, T_c, of YBCO films on silver as a function of substrate inclination 25

30 XRD patterns of YBCO deposited by PLD on IBAD-YSZ-buffered HC substrates 27

31 X-ray ϕ-scan patterns of YBCO, CeO_2, and YSZ, showing epitaxial growth 27

32 Critical-temperature transition curve for YBCO film deposited on CeO_2-buffered IBAD-YSZ on HC substrate 28

33 SEM photomicrographs of YBCO films made by the TFA process at 720, 740, 750, 760, and 780°C during the second heat treatment 30

34 ϕ-scan of YBCO film heat treated at 750°C 32

35 FWHMs of ϕ-scan vs. temperature during second heat treatment of samples made by the TFA process 33

36 FWHMs of samples made by the TFA process vs. temperature during second heat treatment 34

37 Raman spectra for YBCO films made by the TFA process at the second heat-treatment temperatures shown 35

38 Inductive J_c of YBCO made by TFA process vs. processing temperature 37

41 Critical current values for bicrystal grain boundaries at 35 K 41

42 Raman microprobe spectra of $YBa_2Cu_{3-z}Al_zO_x$ single crystals with z = 0.0, 0.2, and 0.35 43

43 Imaging Raman microprobe results for TFA-type YBCO film on CeO_2-buffered YSZ single crystal 44

44 Imaging Raman microprobe results for TFA-type YBCO film on an unbuffered $LaAlO_3$ single crystal 45

45 Raman microprobe spectra of PLD-YBCO film on single-crystal YSZ before and after removing sputter-deposited silver contact layer by soaking in ammoniacal peroxide solution 46

46 Raman spectra of ≈200-nm-thick, e-beam-deposited CeO_2 on roll-textured nickel after annealing at 550°C and 750°C, showing evidence of thin NiO layers under the CeO_2 film 47

47 Raman spectra of CeO_2 films on roll-textured nickel, together with spectrum of sintered polycrystalline CeO_2 48

48 Attenuated total reflection FTIR spectra of single-crystal $LaAlO_3$, single-crystal $SrTiO_3$, and a thin film of STO on LAO 49

49 FTIR spectra of five identical TFA-type YBCO precursor films on CeO_2-buffered YSZ single crystals after various stages of a single thermal treatment 51

50 X-ray reflectivity scans for bare deformation-textured nickel foil specimen, Gd_2O_3-on-DT-nickel specimen, and Y_2O_3-on-DT-nickel specimen, powder scans of the [004] reflections for Gd_2O_3 and Y_2O_3 films on DT nickel substrates 52

51 Azimuthal scans of [222] reflection of Gd_2O_3 and Y_2O_3 buffer layers on DT nickel substrates; and rocking curves for bare DT nickel, Gd_2O_3, and Y_2O_3 reflections 53

52 Representative data for weight gain vs. time for oxidation of Hastelloy C276 in 0.01% O_2 at 600-800°C 57

53 Summary of parabolic rate constant vs. temperature for oxidation of Hastelloy C276 in various atmospheres 57

54 Scale thickness vs. time for oxidation of Hastelloy C276 at 700°C in 0.01% O_2, 0.1% O_2, 1% O_2, 10% O_2, and 100% O_2 58

55 Average surface roughness of scale on polished Hastelloy C276 vs. temperature for scales grown for 10 h in 100% O_2 58

58 Summary of tensile strengths 61

59 Schematic diagram of apparatus used to measure the transient response of a melt-cast BSCCO tube to a pulsed magnetic field 62

60 Transient response of melt-cast BSCCO superconductor tube to pulsed magnetic field 63

61 Superconductor slab of thickness 2a subjected to sinusoidal applied field in z direction..... 64

62 Wave forms of magnetic flux density at various values of x/a in superconductor slab when $a/\delta = 2$ 65

63 Variation of amplitude A with x/a for various values of a/δ 66

64 AC steady-state wave form of magnetic flux density at various values of x/a when $a/\delta = 0.5$ 67

65 AC steady-state wave form of magnetic flux density at various values of x/a when $a/\delta = 2.0$ 68

66 AC steady-state wave form of magnetic flux density at various values of x/a when $a/\delta = 10$. 68

67 Variation of time delay Δt with x/a for various values of a/δ 69

Tables

1 Tilt angle and FWHMs of ϕ- and ω-scans for ISD MgO films deposited at various angles……. 6

2 FWHM values of ϕ- and ω-scans for ISD MgO films before and after deposition of 1 μm MgO 6

3 Properties of thin YBCO films on single-crystal LAO 16

4 Properties of Ag-coated thick-YBCO films on single crystals 17

5 Conditions used for PLD of YBCO on IBAD-YSZ 26

PRACTICAL SUPERCONDUCTOR DEVELOPMENT FOR ELECTRICAL POWER APPLICATIONS

ANNUAL REPORT FOR FY 2001

Abstract

Most large-scale applications of high-critical-temperature superconductors will require wires or tapes that can carry large current in applied magnetic fields. This report describes research and development efforts at Argonne National Laboratory (ANL) aimed at producing practical superconducting components and devices using the Y-Ba-Cu-O and Bi-(Pb)-Sr-Ca-Cu-O systems. Topics discussed include various methods of forming second- and first-generation composite conductors, characterization of their structures and superconducting and mechanical properties, modeling of grain-boundary current transport, and the testing and modeling of a superconducting fault current limiter.

1 Introduction

The superconductor program at Argonne National Laboratory (ANL) is a multifaceted effort to establish the technology base that will enable broad-scale commercialization of high-T_c superconductors (HTSs) in the area of electric power applications. This effort includes investigating materials processing methods to improve the properties of HTSs, developing those methods for producing commercial conductors, fabricating and testing prototype conductors, and studying basic phenomena. Emphasis is placed on the technology and science of fabricating long-length conductors. Cooperative relationships with industrial and academic partners are integral to this program. The principal objective of the ANL program is to develop methods to fabricate and use structurally reliable HTSs for generation, transmission, and storage of electrical energy. These efforts presently focus on the yttrium-barium-copper oxide and bismuth-lead-strontium-calcium-copper oxide superconductor systems.

There are several requirements for composite and monolithic conductors, which can come in the form of wires, tapes, films, or other shapes. For most applications, the conductors must be capable of carrying large currents in the presence of large magnetic fields and must be strong, flexible, and chemically and cryogenically stable. Potential applications for such conductors include transmission lines, motors, generators, transformers, magnetic energy storage devices, and electronics. The principal impediments to the use of bulk HTSs are low critical current and critical current density (J_c) in large applied magnetic fields, relatively poor mechanical properties, and difficulty in fabricating very

long lengths with uniform properties. Processing methods for improvements in these areas have been and continue to be developed, with the majority of the effort centered on $YBa_2Cu_3O_x$ (YBCO) in the form of coated conductors.

This report reviews the technical progress and status of (1) YBCO tapes and their substrate materials; (2) $(Bi,Pb)_2Sr_2Ca_2Cu_3O_x$ (Bi-2223) and $Bi_2Sr_2CaCu_2O_x$ (Bi-2212) wires and tapes; (3) study of microstructures and fundamental grain-boundary properties; and (4) modeling and testing of key properties of prototype superconducting devices.

2 Technical Progress in 1999–2000

2.1 Y-Ba-Cu-O Coated Conductors

2.1.1 Substrate Development for Coated Conductors

Inclined Substrate Deposition (ISD) of MgO

Mechanically polished pieces of Hastelloy C (HC), ≈0.1-mm thick, 10-mm long, and 5-mm wide, were used as substrates for ISD of MgO. MgO films were grown at high (120–300 nm/min) deposition rates from a solid source by electron beam (e-beam) evaporation. The substrate inclination α (shown in Fig. 1 as the angle between the substrate normal and the evaporation direction) ranged from 10 to 70°. The substrate temperature was kept between room temperature and 50°C during film deposition, and oxygen was introduced to maintain an operating pressure of 2×10^{-5} torr. To decrease the surface roughness of as-deposited ISD MgO films, a homoepitaxial layer of MgO was deposited at 700-800°C with $\alpha = 0°$.

To improve the lattice match with YBCO, thin layers of ytrria-stabilized zirconia (YSZ) and ceria were deposited on top of the MgO-buffered substrates. YBCO films were subsequently deposited by pulsed laser deposition (PLD) using an excimer laser system (Lambda Physik COMPex 201). Substrates were attached to the sample stage with silver paste, and the substrate temperature was controlled at 700-800°C during the deposition of YBCO.

Surface morphology and crystalline orientation of the films were investigated by scanning electron microscopy (SEM) and transmission electron microscopy (TEM). Surfaces were examined by atomic force microscopy (AFM) using a Digital Instrument NanoScope. Textures were studied by X-ray diffraction (XRD) pole figure analysis with Cu-K_α radiation. In-plane texture was characterized by the full width at half maximum (FWHM) of ϕ-scans for the MgO (002) reflection, and out-of-plane texture was characterized by the FWHM

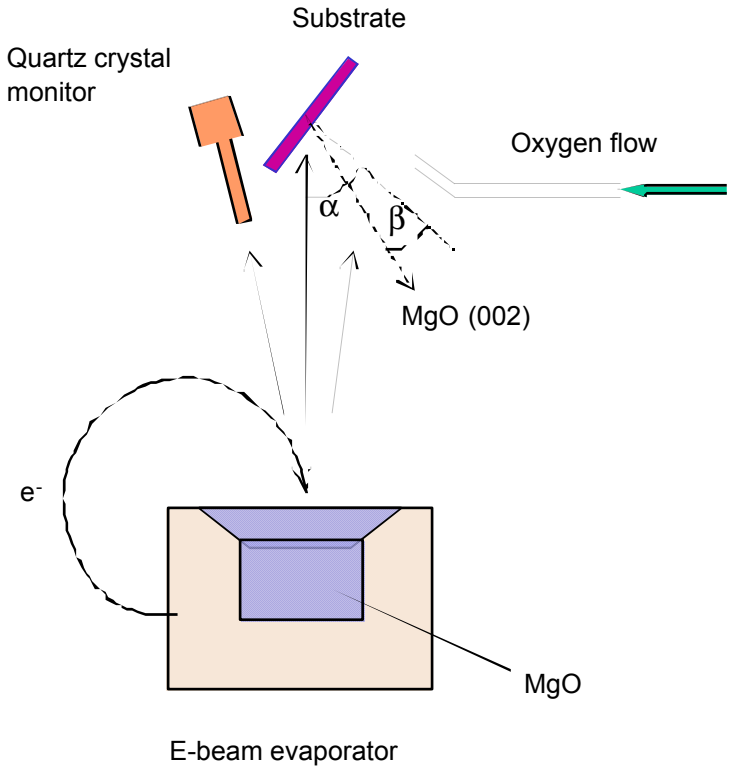

Fig. 1. Experimental arrangement for inclined substrate deposition (ISD) of MgO on HC substrate.

of ω-scans at the MgO [001] pole. The superconducting critical transition temperature (T_c) and critical current density (J_c) were determined by inductive and transport methods. Before the transport measurements, samples were first coated with 2-μm-thick silver by e-beam evaporation and then annealed for 2 h in flowing high-purity oxygen at 400°C. The superconducting properties are described later in Section 2.1.2.

Figure 2 shows the MgO (002) and (220) X-ray pole figures for an ISD MgO film (thickness ≈1.5 μm) that was deposited at room temperature with α = 55°. The sharp, well-defined poles (Fig. 2a) for the [001] axis as well as the [010] and [100] axes show that the film exhibits good biaxial texture. The asymmetric distribution of the pole peaks reveals that the MgO (00*l*) planes are tilted with respect to the substrate normal, unlike the YSZ films prepared by ISD, for which the (001) planes are parallel to the substrate surface. The tilt angle, β, is determined from the χ-angle value of the [001] reflection in the MgO (002) pole figure; β = 32° for the ISD MgO film deposited at room temperature with an inclination of 55°.

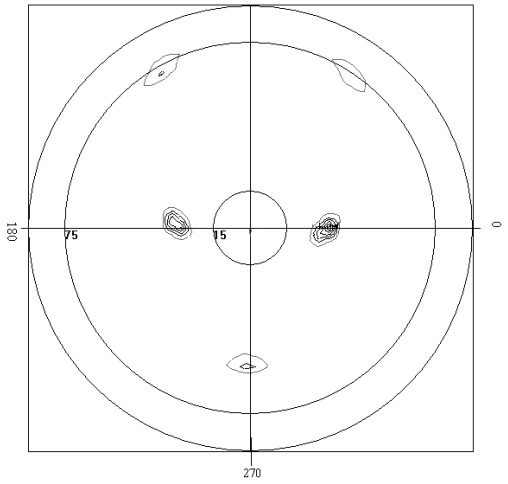

(a) (b)

Fig. 2. (a) MgO (002) and (b) MgO (220) pole figures.

Figure 3 shows typical ϕ- and ω-scan patterns of an ISD MgO film deposited at α = 55°. The FWHMs of ϕ- and ω-scans for MgO (002) are plotted in Fig. 4 as a function of α. The smallest FWHM (12.2°) for a ϕ-scan was observed for films deposited at α = 55°, and the smallest FWHM (5.6°) for an ω-scan was observed for samples deposited at α = 30°. Clear minima are observed at ≈30° and 55°, with the tilt angle β = 22° and 32°, respectively, for these angles. Data regarding the texture of ISD MGO films are summarized in Table 1.

The film tilt angle increases with increasing substrate inclination, which implies that β cannot be independently adjusted without affecting the texture of the films. In this report, MgO films deposited with α = 55° were subsequently used as buffer layers for deposition of YBCO films by PLD. To improve the surface roughness, a thin homoepitaxial layer of MgO was deposited on the ISD MgO films by e-beam evaporation with α = 0°. Table 2 shows the FWHM values for several ISD MgO films before and after deposition of a 1-μm homoepitaxial MgO layer. We observed ≈2 and ≈1° improvements in FWHM values from the MgO (002) ϕ-scan and ω-scans, respectively. AFM analysis showed that the homoepitaxial MgO layer also decreased the root-mean-square (RMS) surface roughness from ≈28 nm to ≈10 nm.

Plan-view SEM revealed (Fig. 5a) a "roof-tile" structure for an ISD MgO film that was deposited at room temperature with α = 55°. A cross-sectional fracture surface showed columnar grains that are nearly perpendicular to the substrate surface (Fig. 5b). The MgO grain size increased with film thickness for thickness <0.25 μm, but stabilized at ≈0.1 μm for film thickness >0.25 μm.

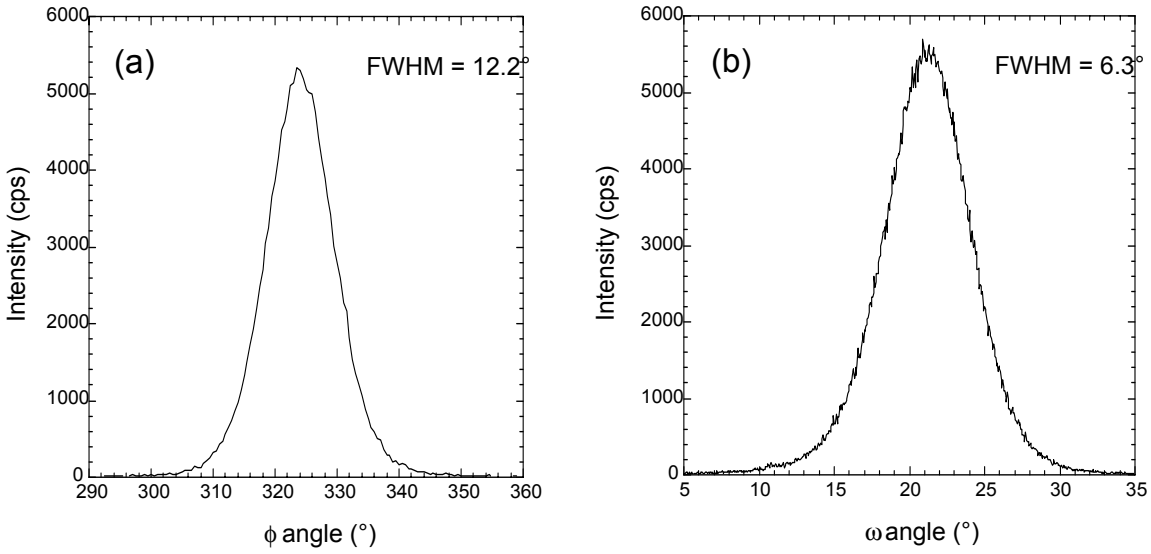

Fig. 3. X-ray diffraction data for ISD MgO deposited at α = 55°: (a) ϕ-scan and (b) ω-scan.

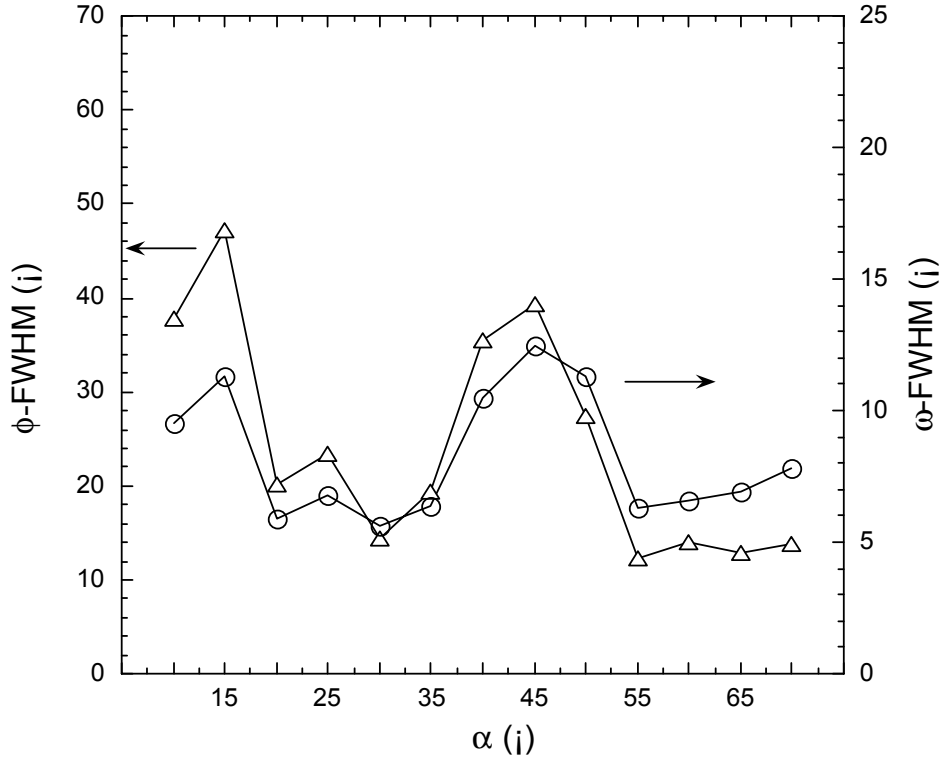

Fig. 4. Effect of inclination, α, on FWHM values of ϕ- and ω-scans.

Table 1. Tilt angle and FWHMs of ϕ- and ω-scans for ISD MgO films deposited at various angles

α (°)	β (°)	ϕ FWHM (°)	ω FWHM (°)
10	16	37.8	9.5
15	16	47.2	11.3
20	17	20.2	5.9
25	17	23.4	6.8
30	22	14.4	5.6
35	18	19.4	6.4
40	16	35.5	10.5
45	20	39.3	12.5
50	24	27.4	11.3
55	32	12.2	6.3
60	28	14.1	6.6
65	32	12.8	6.9
70	37	13.8	7.8

Table 2. FWHM values of ϕ- and ω-scans for ISD MgO films before and after deposition of 1 μm MgO

Sample	ϕ-scan MgO (002) FWHM (°)			ω-scan MgO (002) FWHM (°)		
	Before	After	Change	Before	After	Change
1	11.8	9.7	2.1	6.6	5.6	1.0
2	11.6	9.8	1.8	7.0	5.8	1.2
3	12.7	10.9	1.8	6.5	5.6	0.9
4	13.2	9.2	4.0	6.8	5.2	1.6

Figure 6 shows SEM images of a sample made of a 1.5-µm-thick ISD MgO layer deposited at room temperature, with α = 55°, followed by a 0.5-µm-thick additional MgO layer deposited at 700°C, with α = 0°. Surface smoothness and texture were improved significantly.

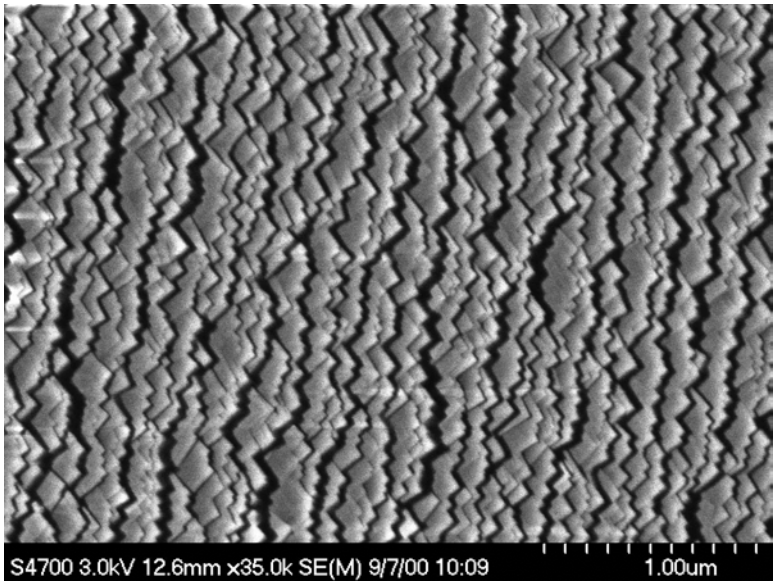

(a)

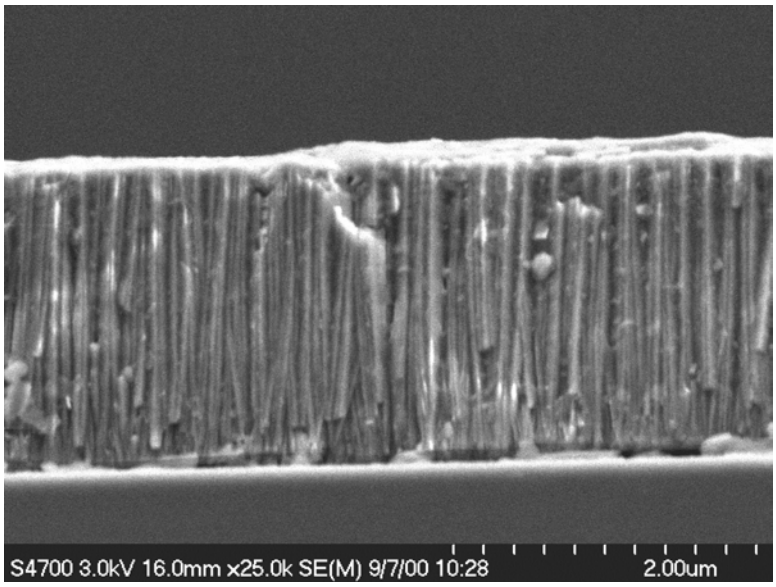

(b)

Fig. 5. SEM photomicrographs of ISD MgO film: (a) top surface and (b) cross section.

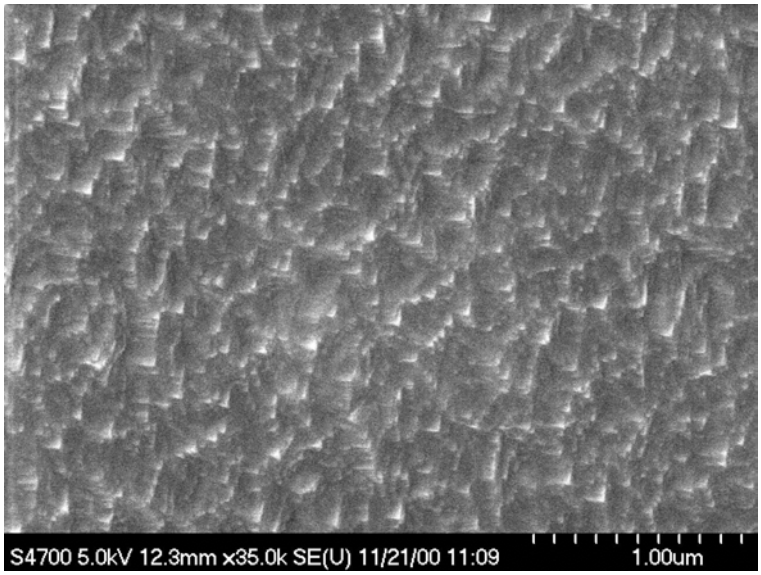

(a)

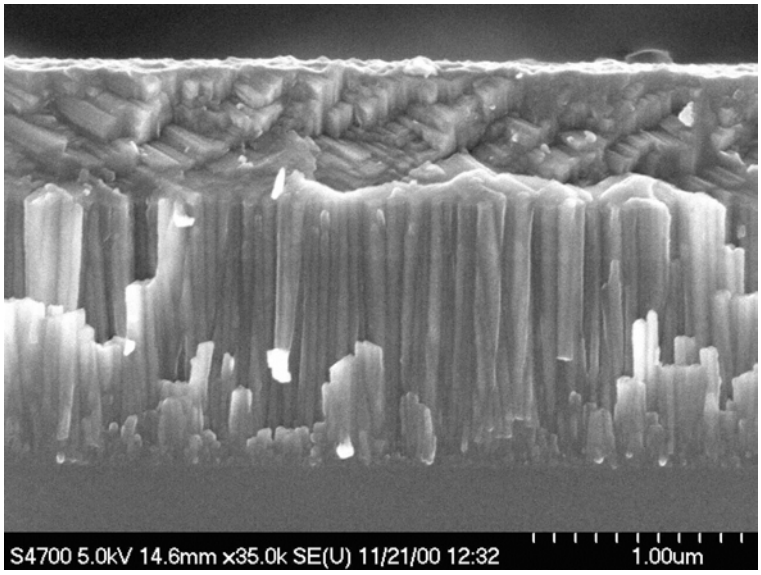

(b)

Fig. 6. SEM photomicrographs of ISD MgO + e-beam MgO film: (a) top surface and (b) cross section.

Figure 7 shows a TEM image and selected area diffraction (SAD) pattern of MgO columnar grains in a film that was deposited with $\alpha = 55°$. The top facet of MgO grains is a (002) plane. Film morphology and texture evolution in the ISD MgO films can be understood from the self-shadowing effect. It has been demonstrated [1] that in-plane texture develops during the growth of polycrystalline films through a combination of fast growth along a certain

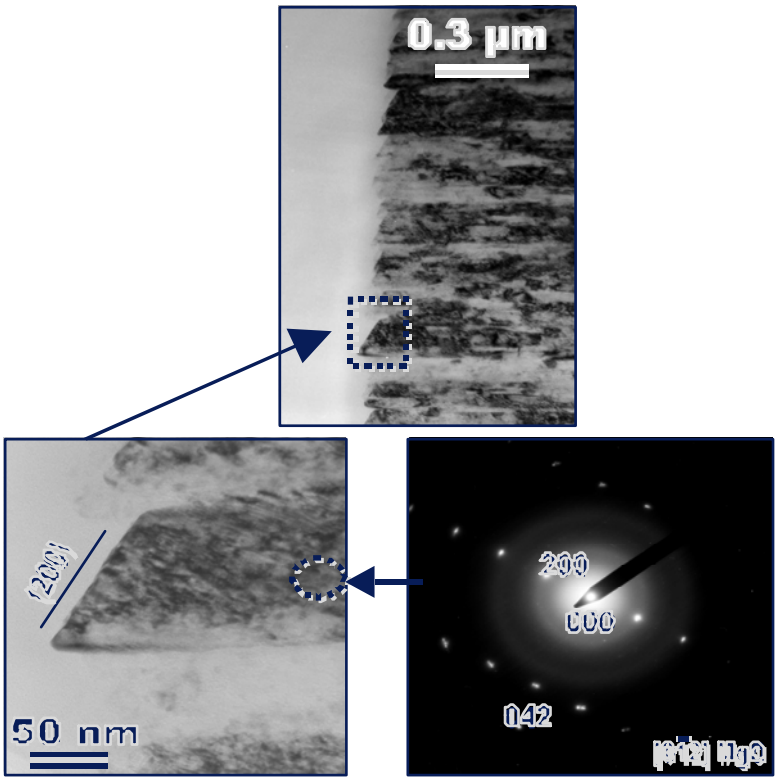

Fig. 7. Facet of (200) plane on top of MgO columnar grain and corresponding SAD pattern.

crystallographic direction and self-shadowing that results from deposition at an inclined angle. In the case of MgO, the fast growth plane is {200} [2]. Because maximizing the (002) faces can decrease the surface free energy, the {200} plane is also the equilibrium crystal habit, as confirmed by the cubic morphology exhibited in the MgO film [3]. With deposition at an inclined angle, the {200} plane rotates toward the vapor source, so that the (002) surface grows faster than other crystalline faces. A schematic representation of this grain growth mechanism is illustrated in Fig. 8.

Direct Deposition of YBCO on Silver

Direct deposition of YBCO on silver (Ag) substrates offers the potential to simplify the fabrication of coated conductors by eliminating the need for buffer layers. Other fabrication methods require multiple buffer layers to prevent cation diffusion that degrades the properties of YBCO. Direct deposition of YBCO on Ag removes the need for buffer layers, because Ag is chemically inert toward YBCO under fabrication conditions.

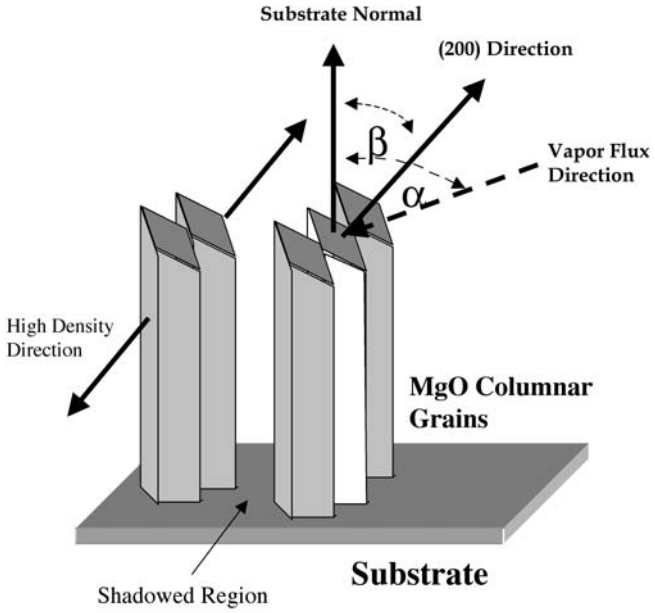

Fig. 8. Illustration of ISD MgO growth mechanism due to shadowing effect.

Mechanically polished Ag pieces (1 μm finish) measuring ≈0.2-mm thick, ≈5-mm wide, and 10-mm long were used as substrates for ISD of YBCO films. The experimental arrangement for ISD is shown in Fig. 9, where the inclination α is the angle between the substrate normal and the axial direction of the plume. YBCO films were deposited at various inclinations by means of commercial YBCO targets (2.5-cm dia. x 0.64-cm thick) and a Lambda Physik LPX 200 excimer laser with KrF as the lasing medium. The Ag-substrate was attached to a temperature-controlled stage by using silver paste, and was kept at 700-800°C during deposition. The laser spot size on the rotating target was ≈3 mm^2, giving an energy density of 2.5-3 J/cm^2. The distance between the target and the substrate was ≈5.5 cm. The base pressure of the chamber was 2×10^{-6} torr. High-purity oxygen flowed (≈10 sccm) during deposition to maintain an operating pressure of 0.1 to 0.3 torr.

X-ray diffraction pole figures were collected with a Scintag XRD 2000 diffractometer using Cu-K_α radiation. TEM was performed in a Philips CM30 microscope. Surfaces of the films were analyzed by AFM using a Digital Instrument NanoScope. The superconducting transition temperature (T_c) was measured inductively, and the transport critical current density (J_c) was measured by the four-probe method. To measure the transport J_c, samples were first coated with 2-μm-thick silver by e-beam evaporation, then annealed for 2 h in flowing high-purity oxygen at 400°C. The superconducting properties are described later in Section 2.1.2.

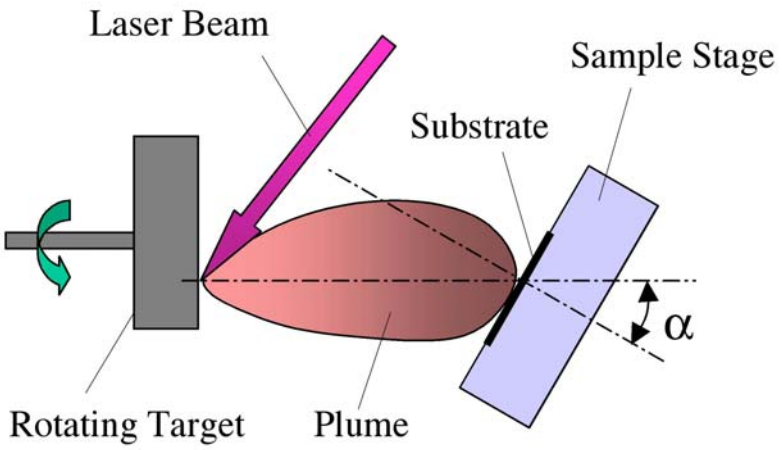

Fig. 9. Experimental setup for the inclined substrate deposition (ISD) of YBCO films directly on Ag substrates.

Ion Beam Assisted Deposition (IBAD) of Yttria-Stabilized Zirconia (YSZ)

Mechanically polished HC pieces measuring ≈0.1-mm thick, 1-cm long, and ≈5-mm wide were used as substrates for IBAD of YSZ and subsequent YBCO deposition. Thin YSZ buffer films were grown from sintered YSZ pieces using an e-beam evaporator. Polished HC substrates were attached to a water-cooled sample stage with vacuum silver paste. The Ar^+ ion beam, at an incident angle of 55° with respect to the substrate normal, was generated by an 8-cm Kaufman source operating at 300 eV. A Faraday cup (Kimball Physics FC-70A) was used to measure the beam intensity before each deposition. Base pressure of the deposition chamber was 2×10^{-7} torr, and an operating pressure of $\approx 1 \times 10^{-4}$ torr was maintained with a flowing 10:1 argon-oxygen mixture and a cryogenic pump. A quartz crystal monitor was mounted beside the sample stage to monitor the deposition rate. Circulating water flowed through the sample stage to dissipate heat generated by the ion source and maintain the substrate temperature below 100°C during the deposition. Without cooling water, the substrate temperature would rise to ≥250°C.

YBCO films of 300- to 1000-nm thickness were deposited by PLD with a Lambda Physik COMPex 201 excimer laser with a Kr-F_2 gas premixture as the lasing medium. Commercial YBCO targets (Superconductive Components, Inc., Columbus, OH) of 25.4 mm in diameter and 6.4-mm thick were used. Substrates were attached to a heatable sample stage with silver paste and heated to ≈800°C during deposition. The laser spot focused at the rotating target was 2-3 mm in diameter, which resulted in an energy density of ≈2 J/cm^2. Distance between the target and the substrates was 7 cm. The desired oxygen partial pressure (in the

range of 100-300 mtorr) was obtained by flowing ultra-high-purity oxygen through the chamber. A pulse repetition rate of 8 Hz produced a growth rate of ≈15 nm/min. A CeO_2 buffer layer (thickness ≈10 nm) was deposited at 800°C by PLD before depositing YBCO to improve the lattice match with YBCO.

The superconducting T_c and J_c were determined by the inductive method and confirmed by the four-probe transport method at 77 K in liquid nitrogen. The inductive test was used as a standard characterization tool to measure the superconducting properties of our YBCO films. Thin-film superconductor samples were placed between a primary and secondary coil pair with inner diameter of 1 mm and outer diameter of 5 mm. Alternating current was introduced to the primary coil and detected from the secondary coil by a lock-in amplifier (Stanford Research Systems SR830 DSP). Samples used for transport measurements were first coated with silver (thickness ≈2 μm) by e-beam evaporation, then annealed for 2 h at 400°C in flowing high-purity oxygen. Typical samples used for the four-probe transport measurement were 3-5 mm wide and 1 cm long.

Texture was examined by X-ray diffraction pole figure analysis with Cu-K_α radiation. In-plane texture was characterized by the FWHM of ϕ-scans for the YSZ (111) reflection (2θ = 30.1°), while out-of-plane texture was characterized by the FWHM of ω-scans for the YSZ (002) reflection (2θ = 34.9°). AFM observations were conducted with a Digital Instruments D3100 SPM. TEM was done with a Philips CM30 microscope operated at 300 keV.

The crystalline texture of the IBAD YSZ films was characterized by X-ray diffraction pole figure analysis. A typical YSZ (111) X-ray pole figure is shown in Fig. 10. Four well-defined (111) poles are evenly distributed with respect to the azimuth angle and have a tilt (χ-angle) of ≈55°. This confirmed that the (00*l*) planes of the IBAD YSZ film are parallel to the substrate surface. Figures 11 and 12 show YSZ (111) ϕ- and ω-scans for ≈1-μm YSZ films deposited on the HC substrate, respectively. The FWHM of the YSZ (111) ϕ-scan is usually used to quantitatively characterize in-plane textures of IBAD YSZ films. Out-of-plane texture was characterized from the YSZ (002) ω-scan, shown in Fig. 12. The IBAD YSZ films that were deposited with 300 eV beam energy at a substrate temperature of 90°C gave an FWHM of 13.2° for the YSZ (111) ϕ-scan and an FWHM of 7.7° for the YSZ (200) ω-scan .

Figure 13 plots the FWHM of a YSZ (111) ϕ-scan vs. the substrate temperature during deposition of ≈1-μm-thick IBAD YSZ films. In-plane texture of the IBAD YSZ films improved with a decrease in substrate temperature. These results suggest that a FWHM of ≈12° could be obtained with a substrate temperature of ≈50°C.

Fig. 10. YSZ (111) pole figure of IBAD YSZ film deposited on HC substrate with 300 eV ion beam energy at substrate temperature of 90°C.

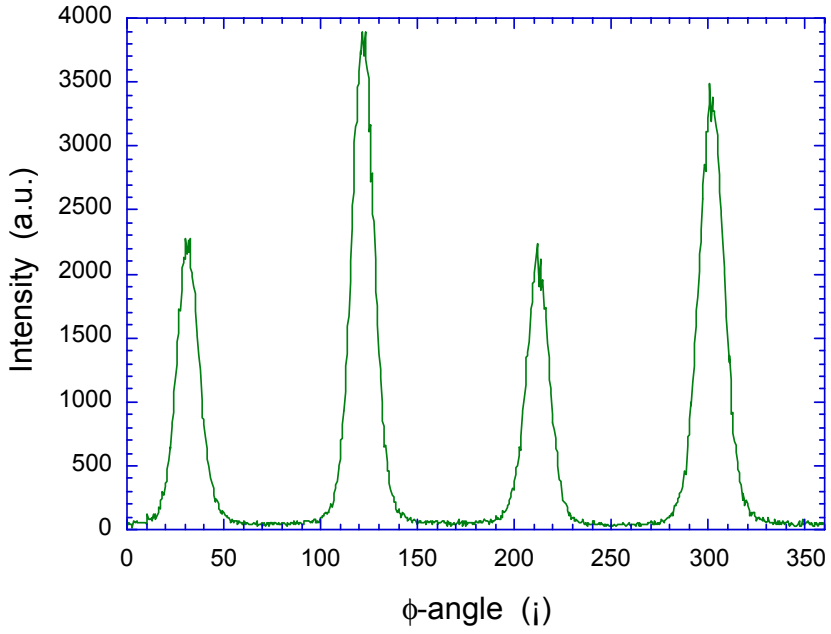

Fig. 11. In-plane texture of IBAD YSZ film deposited on HC substrate with 55° bombardment angle, 300 eV beam energy, and substrate temperature of 90°C.

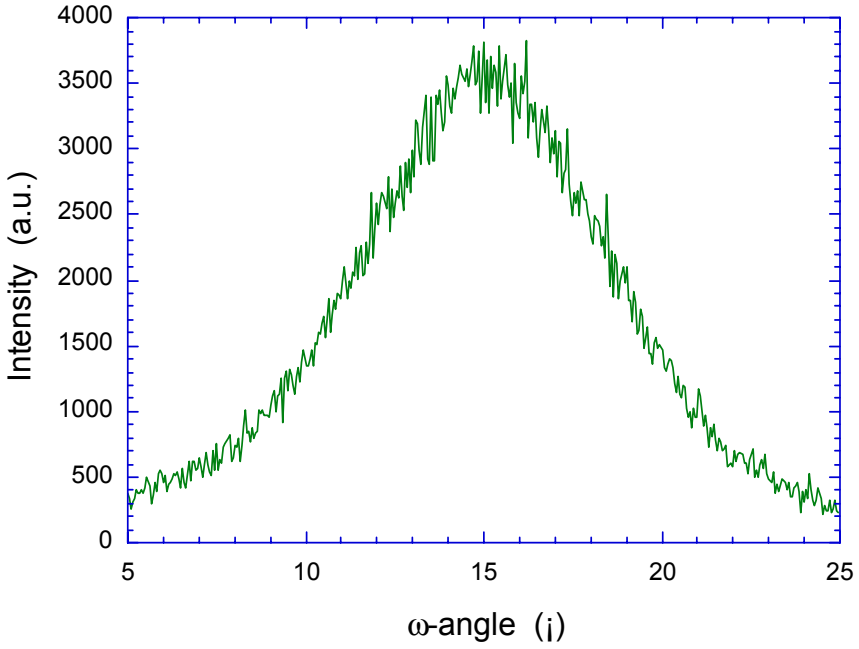

Fig. 12. Out-of-plane texture of IBAD YSZ film deposited on HC substrate with 55° bombardment angle, 300 eV beam energy, and substrate temperature of 90°C.

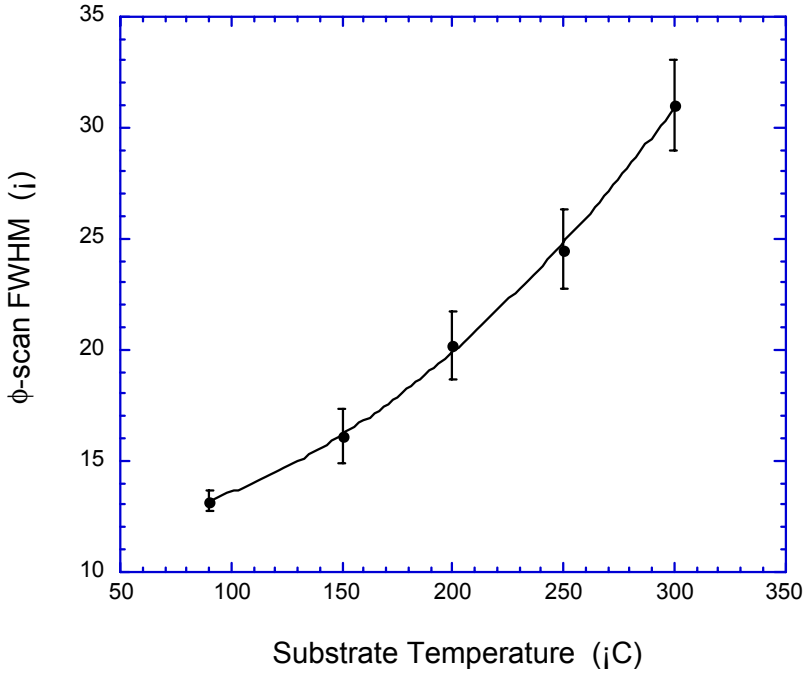

Fig. 13. FWHM of YSZ (111) ϕ-scan for IBAD YSZ films deposited at various substrate temperatures.

Figure 14 shows a top surface AFM image of an IBAD YSZ film. A dense, smooth surface with RMS roughness of ≈3.3 nm was observed. Figure 15 shows a cross-sectional TEM image and SAD patterns of IBAD YSZ at various distances from the substrate. The SAD patterns indicate that biaxial alignment in the YSZ film improves with increasing film thickness; a thickness of 500 to 800 μm is necessary for good in-plane texture in the YSZ films.

2.1.2 Pulsed Laser Deposition (PLD) of YBCO

YBCO on Single-Crystal Substrates

Because the properties of a coated conductor are only as good as the YBCO that it contains, we have continued to optimize the PLD and postannealing conditions for producing high-quality YBCO films. At an optimum deposition temperature of ≈790°C, high-quality YBCO films are now consistently obtained on $LaAlO_3$ (LAO) and $SrTiO_3$ (STO) single-crystal substrates. YBCO films exhibit $T_c \geq 90$ K and $J_c > 3$ MA/cm^2 for films ≤0.3 μm thick and 1 MA/cm^2 for films with thickness ≥1 μm. The J_c of YBCO films on LAO single-crystal substrates is sensitive to film thickness, decreasing with increasing film thickness even for films <0.3 μm thick. Representative data are shown in Table 3.

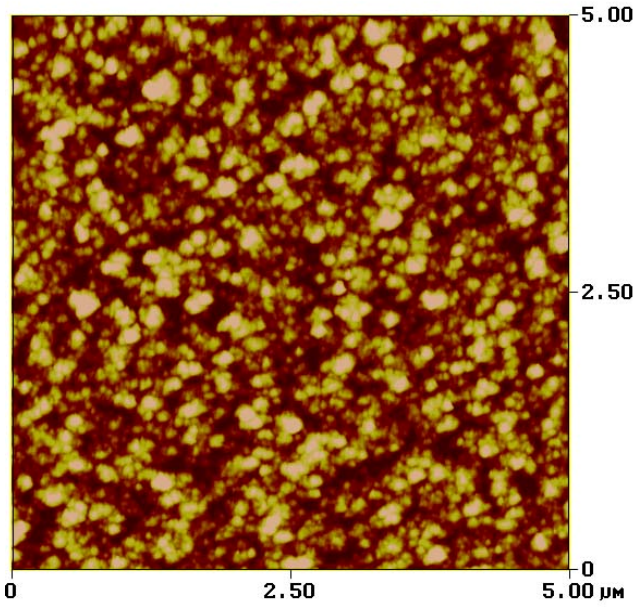

Fig. 14. AFM image of top surface of IBAD YSZ film deposited with 300 eV beam energy at 90°C substrate temperature.

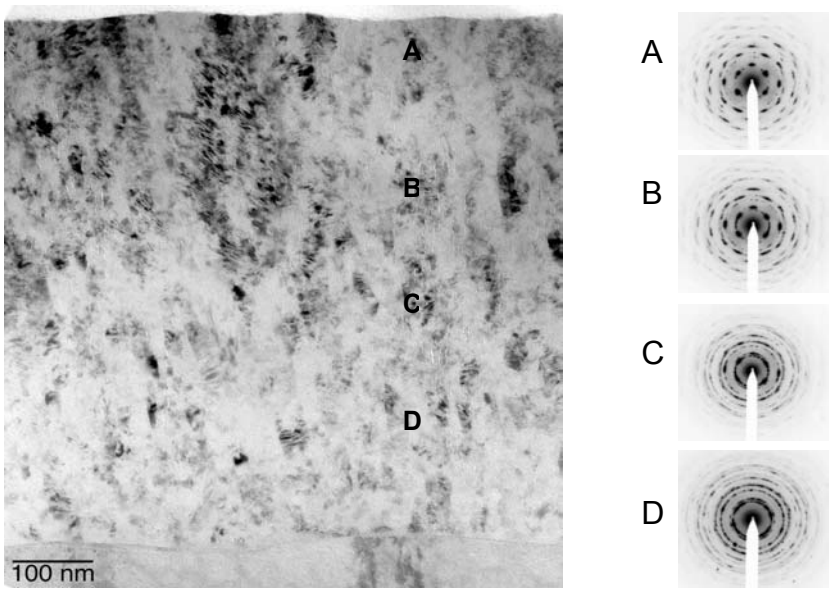

Fig. 15. Cross-sectional TEM and SAD patterns of IBAD YSZ at four distances (A, B, C, D) from the substrate.

Table 3. Properties of thin YBCO films on single-crystal LAO

Sample	Type	T_c (K)	$J_{c,m}$ (MA/cm^2)	Thickness (μm)
1020A1	YBCO/LAO	90.0	8.3	0.10
1011A2	YBCO/LAO	90.0	6.6	0.15
0802B2	YBCO/LAO	87.0	5.0	0.20
0912A2	YBCO/LAO	90.5	3.3	0.30

Ex-situ postannealing conditions have been optimized, resulting in significant improvements in T_c and J_c (usually measured by inductive methods) for the YBCO/LAO samples (Fig. 16).

Transport J_c measurements require current probes with a low contact resistance. To ensure low contact resistance, samples are first coated with Ag, then they are annealed to re-oxygenate the samples. The annealing conditionsafter Ag coating were studied for YBCO films on LAO and STO crystals. Representative data from these studies are shown in Table 4 and Fig. 17.

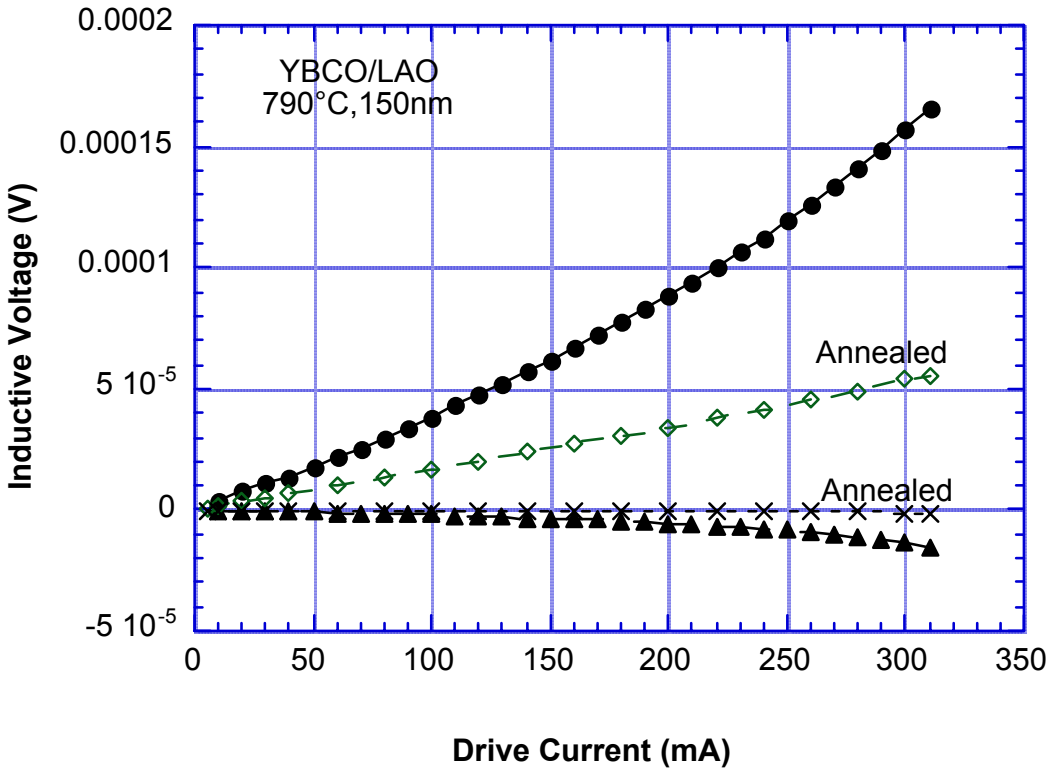

Fig. 16. Inductive voltage vs. drive current for YBCO film on LAO. Annealing increased the inductive J_c from 4.0 to 6.6 MA/cm^2 at 77 K.

Table 4. Properties of Ag-coated thick-YBCO films on single crystals

Sample	T_c (K)	$J_{c,m}$ [a] (MA/cm^2)	$J_{c,t}$ [a] (MA/cm^2)	Thickness (μm)	Width (mm)
YBCO/LAO	90.5	3.3	3.17	0.3	5.2
YBCO/LAO	91.0	>1.0	1.35	1.0	5
YBCO/STO	90.8	>1.0	1.57	1.0	5

[a] $J_{c,m}$ and $J_{c,t}$ are J_c measured by inductive and transport methods, respectively.

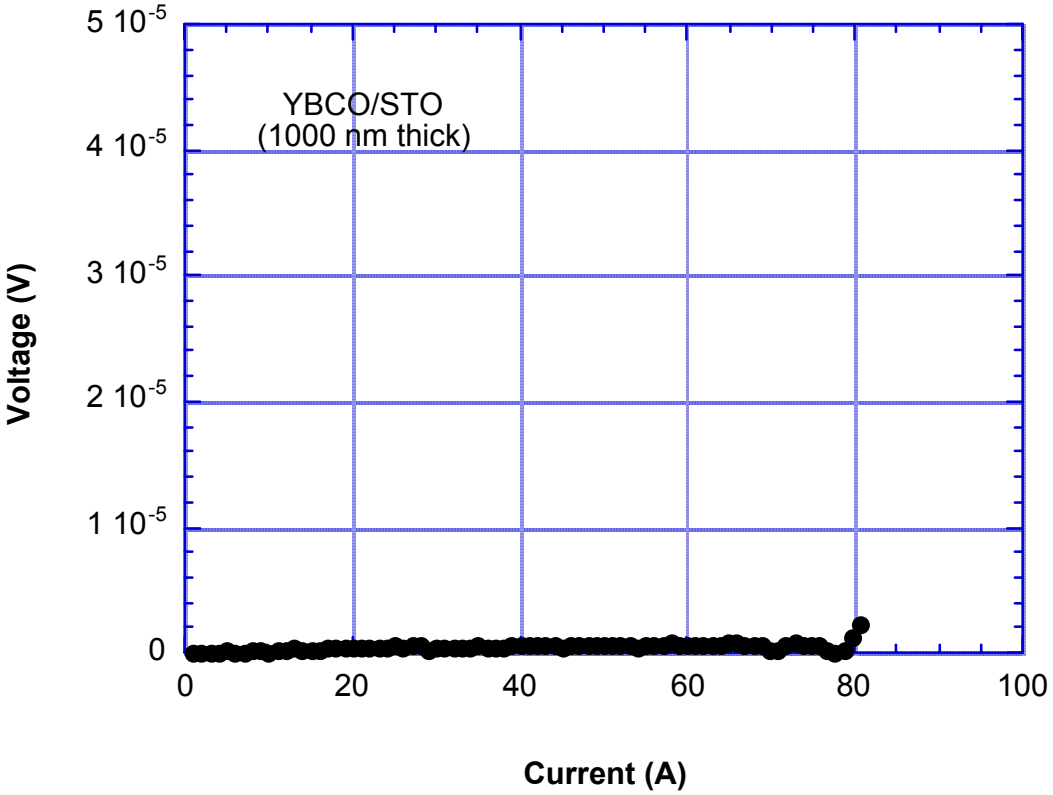

Fig. 17. Plot of current vs. voltage at 77 K for YBCO film on STO crystal transport I_c = 79 A and $J_{c,t}$ = 1.57 MA/cm^2.

YBCO on ISD-MgO Substrates

Biaxially aligned YBCO films were deposited by PLD on ISD-MgO-buffered HC substrates. The FWHM values of the YBCO films were generally 1–2° smaller than those of the underlying MgO films. Figure 18 shows ϕ-scans for the MgO (220) and YBCO (103) grown on a MgO-buffered HC substrate; it reveals epitaxial growth with cube-to-cube biaxial alignment: YBCO [001] // MgO [001] and YBCO [100] // MgO [100] (or MgO [010]). To decrease the lattice mismatch between the substrate and YBCO, various buffer layers were deposited between the MgO and YBCO layers by either e-beam evaporation or PLD. Inductive measurements for 0.5-μm-thick YBCO on MgO-buffered HC (Fig. 19) show that T_c = 90 K, and the superconducting transition is complete at 88 K. The inductive measurements also showed a critical current density of ≈2 x 10^5 A/cm^2 at 77 K in the self-field on a sample that is 0.5-μm thick, 0.5-cm wide, and 1-cm long.

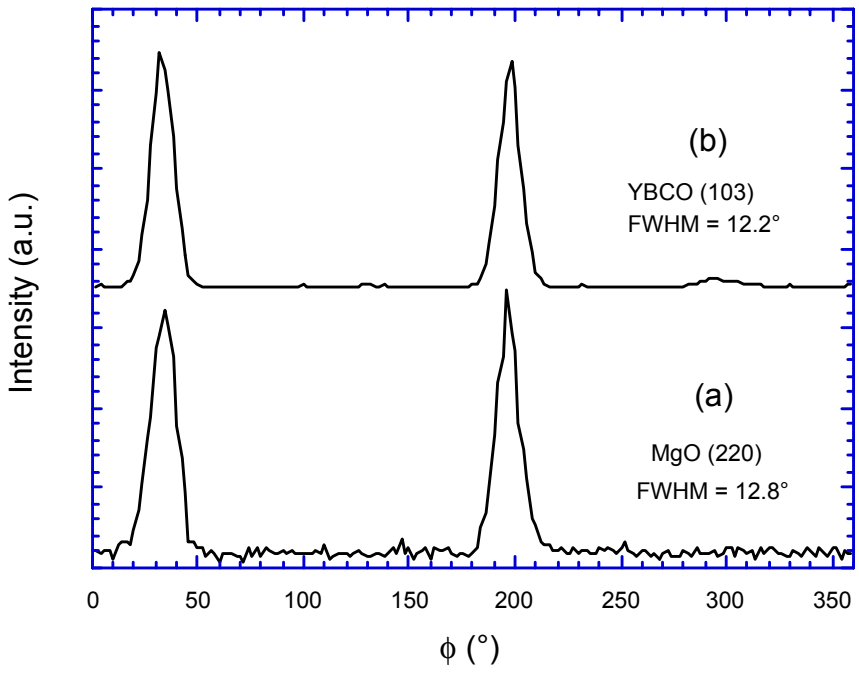

Fig. 18. ϕ-scans of MgO (220) and YBCO (103) showing epitaxial growth.

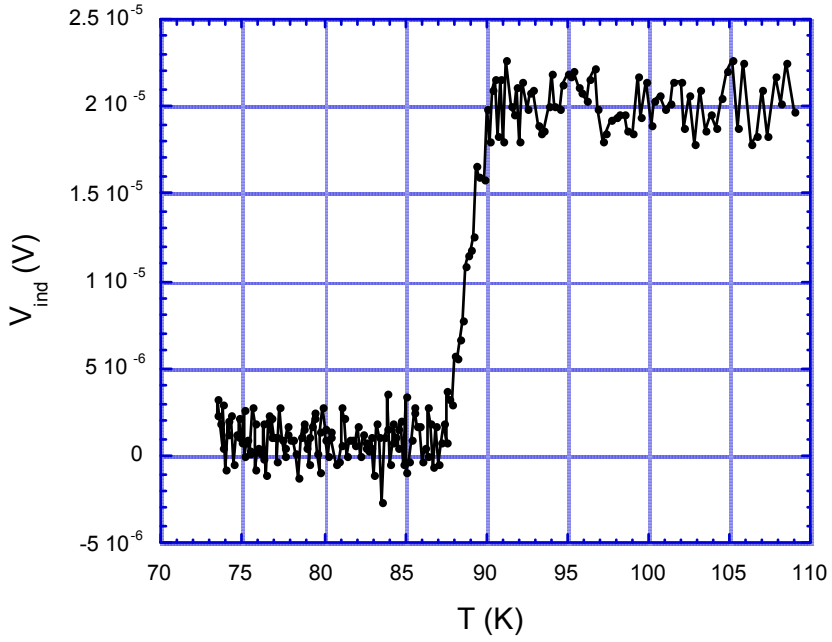

Fig. 19. Critical-temperature transition curve for YBCO film deposited on ISD-MgO-buffered HC substrate.

YBCO on Silver Substrates

The surface morphology of YBCO films deposited on polished Ag substrates was examined by AFM. Unlike YBCO on single-crystal substrates, grain boundaries are clearly seen in the plan view of YBCO on Ag (Fig. 20). The film contains c-axis oriented grains with an average size of ≈0.5 μm as well as a few uniformly dispersed a-axis oriented grains (Fig. 20). Also, a-axis oriented grains were seen by SEM (Fig. 21). Only (*00l*) peaks were observed in the X-ray diffraction pattern (Fig. 22), however, indicating that c-axis orientation was dominant in the YBCO film. The strong c-axis alignment was confirmed by an intense peak at 340 cm^{-1} in the Raman spectrum (Fig. 23). The YBCO (103) pole figure (Fig. 24) revealed, however, that the YBCO on Ag had only fiber texture with its c-axes aligned parallel to the substrate normal. No biaxial alignment was evident, i.e., the a- and b-axes of YBCO were not preferentially aligned within the plane of the film.

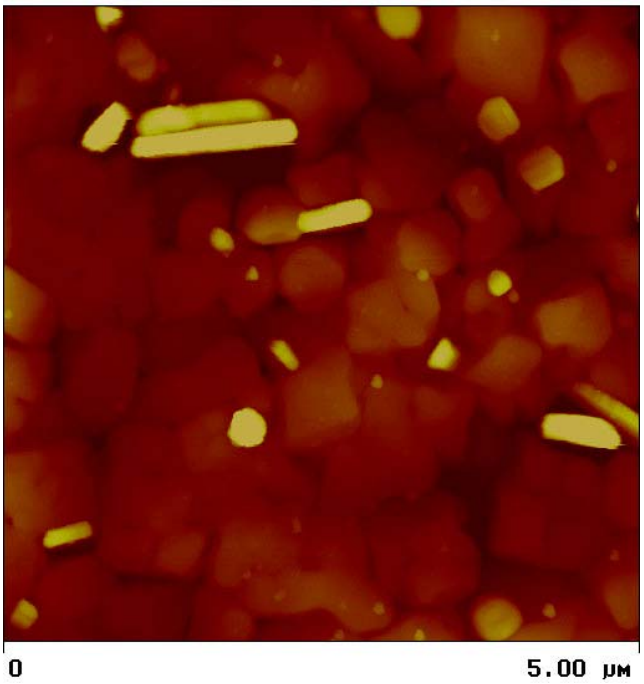

Fig. 20. Plan view by AFM of a YBCO film deposited directly on Ag substrate at 755°C with inclination of 55°.

Cross-sectional TEM (Fig. 25) revealed an amorphous layer at the interface between YBCO and the Ag substrate. The origin of this layer and its role in the growth of YBCO are not yet fully understood and are being studied further. For the sample deposited at 755°C with an inclination of 55°, the thickness of the amorphous layer was ≈70 nm. Figure 26 shows the TEM EDS spectra of the

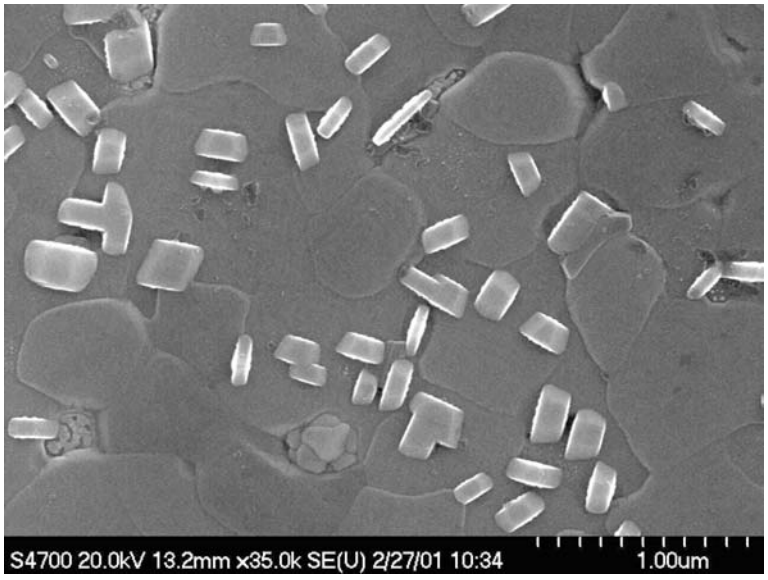

Fig. 21. Secondary electron image (plan view) of a YBCO film deposited directly on Ag substrate at 755°C with inclination of 55°.

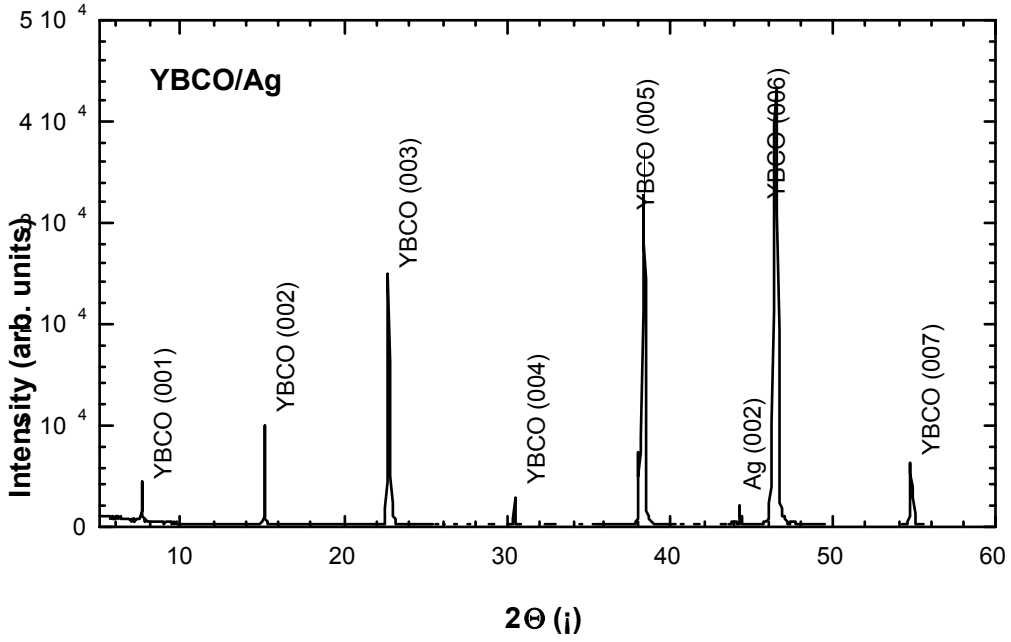

Fig. 22. A 2-Θ X-ray diffraction pattern for the YBCO film deposited directly on polished Ag substrate.

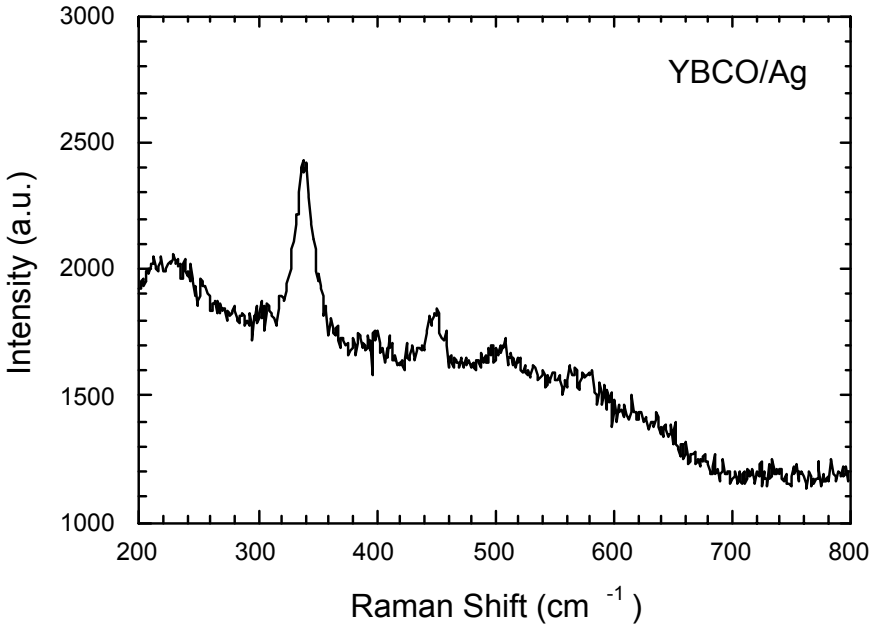

Fig. 23. Raman spectrum of a YBCO thin film deposited directly on Ag substrate.

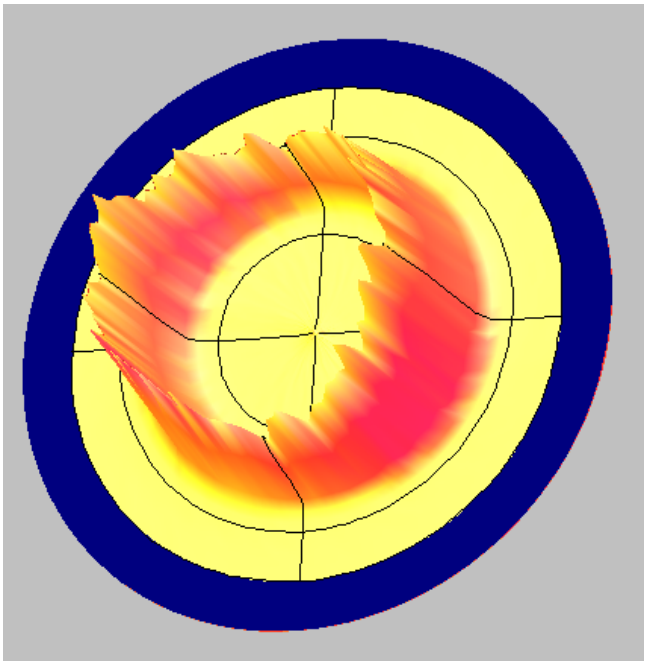

Fig. 24. YBCO (103) pole figure of a YBCO thin film deposited directly on Ag substrate.

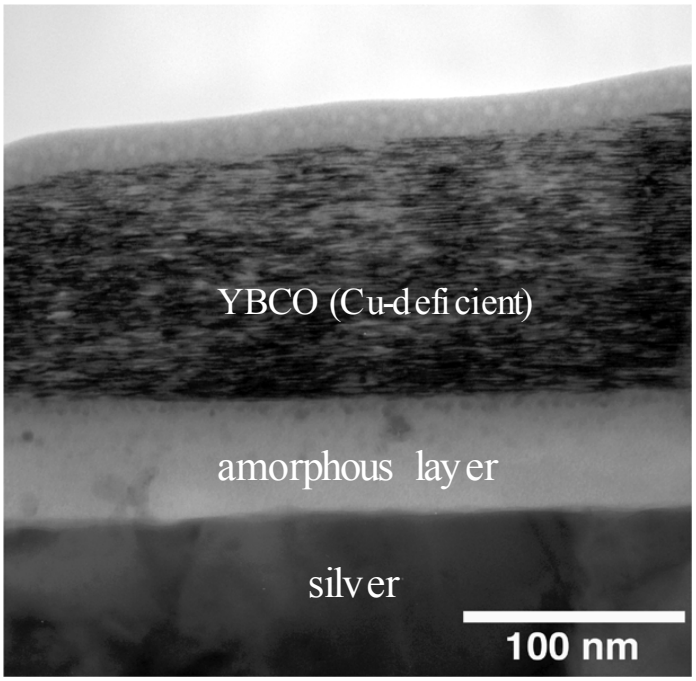

Fig. 25. Cross-sectional view (by TEM) of YBCO deposited directly on Ag substrate at 755°C with an inclination of 55°.

YBCO film and the amorphous layer. The YBCO layer contained minimal Ag, while the amorphous layer contained significant concentrations of Ag, Y, Ba, and Cu. The relative concentrations varied through the thickness of the amorphous layer, with the Ag concentration decreasing and the Y, Ba, and Cu concentrations increasing closer to the YBCO film. In addition, TEM EDS indicated that the YBCO was slightly Cu-deficient, suggesting that Cu diffused into the amorphous layer or the Ag substrate. To reduce the driving force for Cu diffusion, several Ag substrates were prepared with 0.5 mol.% Cu. YBCO will be deposited on these substrates by PLD, and the effect of Cu on YBCO growth and properties will be studied.

Figure 27 shows the superconducting transition that was measured inductively for a YBCO film deposited on Ag at 755°C with an inclination of 55°. The transition was sharp with T_c(onset) ≈90 K and was complete at ≈88 K. To measure the transport J_c by the four-probe method, YBCO/Ag samples were coated with Ag (≈2-μm thick) by e-beam evaporation, then were annealed in flowing high-purity oxygen at 400°C for 2 h. For YBCO deposited at 755°C with an inclination of 55°, measurements shown in Fig. 28 indicate that J_c(transport) = 275,000 A/cm^2 at 77 K in the self-field using the 1 μV/cm criteria. Figure 29 shows T_c(onset) for samples deposited at inclinations of 35, 55, and 72°. The data are quite scattered; but the highest T_c was obtained on a sample deposited with an inclination of 55°.

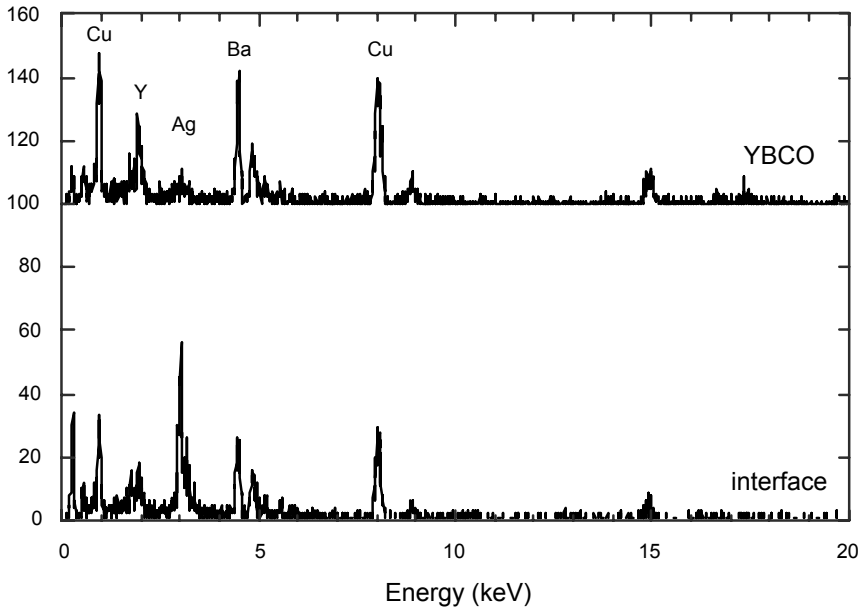

Fig. 26. TEM EDS spectra of YBCO film deposited directly on Ag and an amorphous layer between Ag and YBCO.

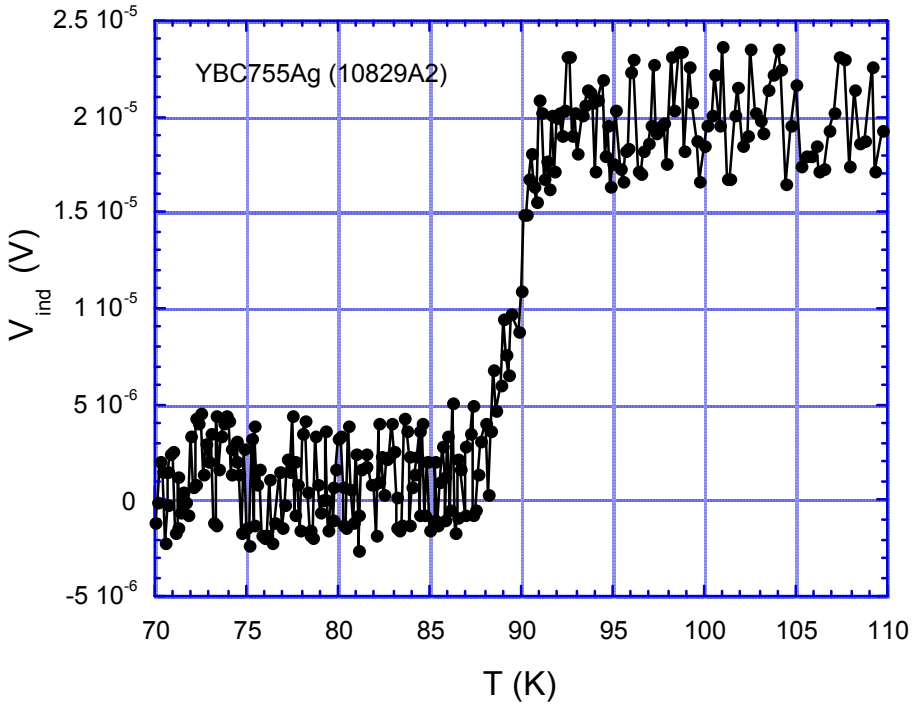

Fig. 27. Superconducting transition for YBCO deposited directly on Ag at 755°C, as determined by inductive method.

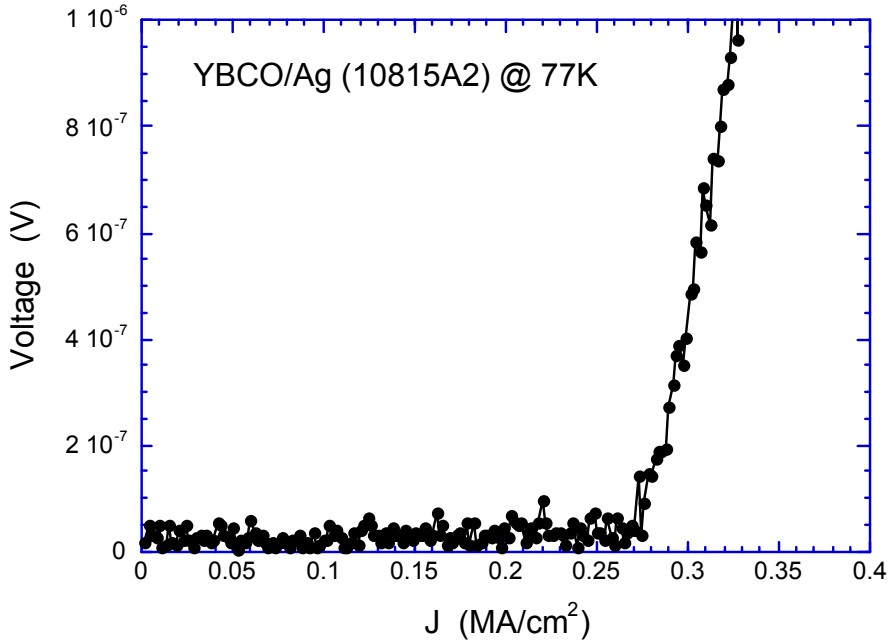

Fig. 28. J_c transition curve in self-field for a YBCO film deposited directly on Ag at 755°C .

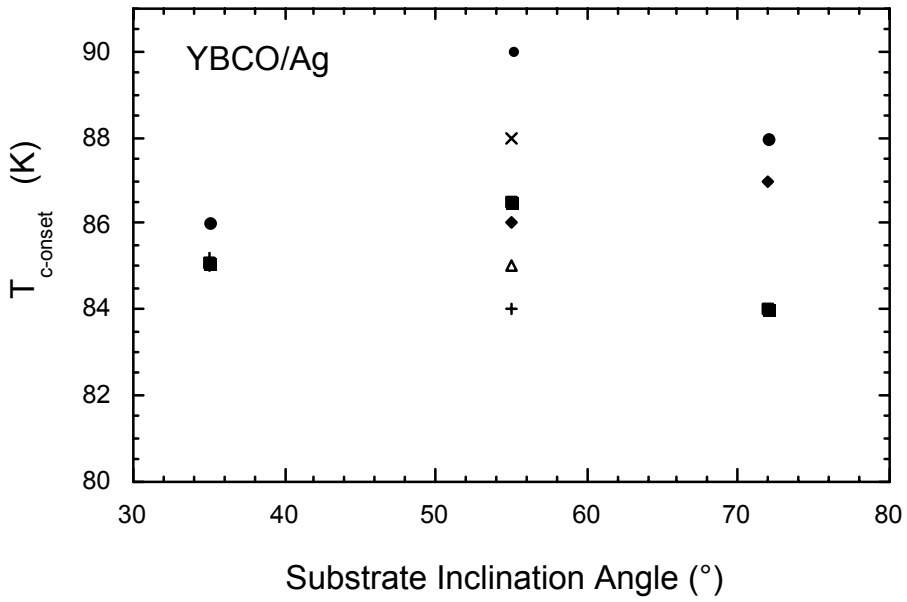

Fig. 29. Critical transition temperature, T_c, of YBCO films on silver as a function of substrate inclination.

YBCO on IBAD-YSZ Substrates

Biaxially aligned YBCO films were deposited on IBAD-YSZ-buffered HC substrates by PLD under the conditions listed in Table 5. An XRD 2θ-scan of YBCO directly deposited on HC substrate reveals tiny YBCO (*l*00) peaks, as shown in Fig. 30a. Before PLD of YBCO, a CeO_2 buffer layer (thickness ≈10 nm) was deposited on the YSZ by e-beam evaporation to reduce the lattice mismatch between YBCO and YSZ. Deposition of the ceria buffer layer on the YSZ film helped to reduce a-axis misalignment and improve c-axis alignment, as shown in Fig. 30b. The YBCO (*l*00) peaks disappeared in the XRD pattern of the sample with the ceria buffer layer. Layer-by-layer XRD ϕ-scans of the sample indicated epitaxial growth of the CeO_2 and YBCO films, as shown in Fig. 31. In-plane-texture FWHMs of 12° and 9° were observed for CeO_2 (111) and YBCO (103), respectively.

Table 5. Conditions used for PLD of YBCO on IBAD-YSZ

Laser wavelength	248 nm (Kr-F)
Repetition rate	8 Hz
Pulse width	25 ns
Energy density	1-3 J/cm^2
Substrate temperature	700-800°C
Operating pressure	100-300 mtorr
Oxygen flow rate	10 sccm
Target-to-substrate distance	4-8 cm

A YBCO film (0.5-μm thick) was deposited by PLD on ceria-buffered IBAD-YSZ that was fabricated on HC substrate. Inductive measurements (Fig. 32) showed that T_c (onset) = 90 K and the superconducting transition was completed at 88.5 K. J_c(transport) for this sample was 2.2 x 10^6 A/cm^2 at 77 K with zero external field.

2.1.3 YBCO Films from a Solution Process

Various processing methods are being investigated for the fabrication of YBCO-coated conductors on metallic substrates. Promising options include nonvacuum ex-situ processes such as metal organic deposition (MOD) and sol-gel processing. Solution techniques are now being studied by several groups, and some of their results are comparable to superconducting performance levels obtained by vacuum processes such as PLD. Of the solution techniques, the

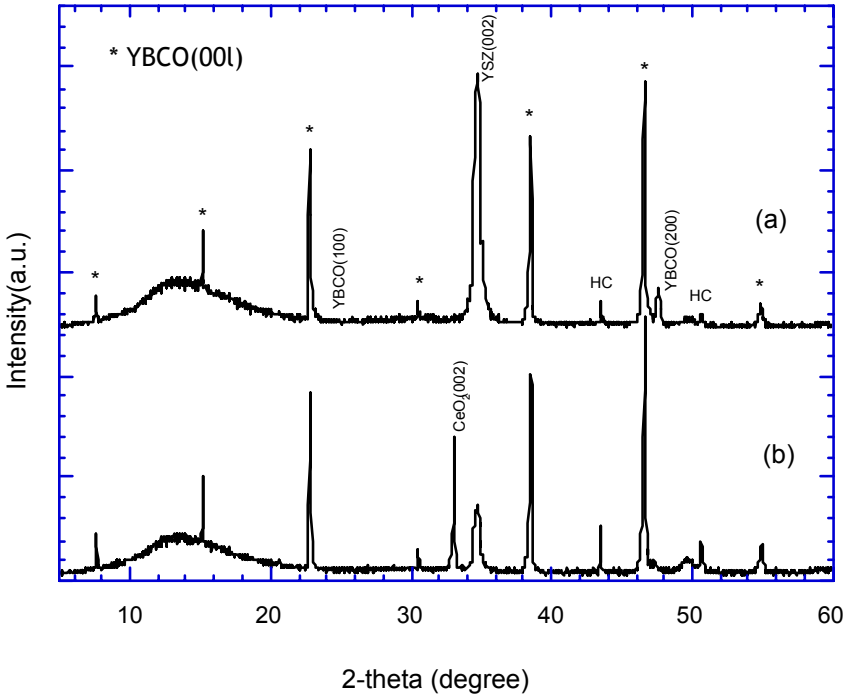

Fig. 30. XRD patterns of YBCO deposited by PLD on IBAD-YSZ-buffered HC substrates.

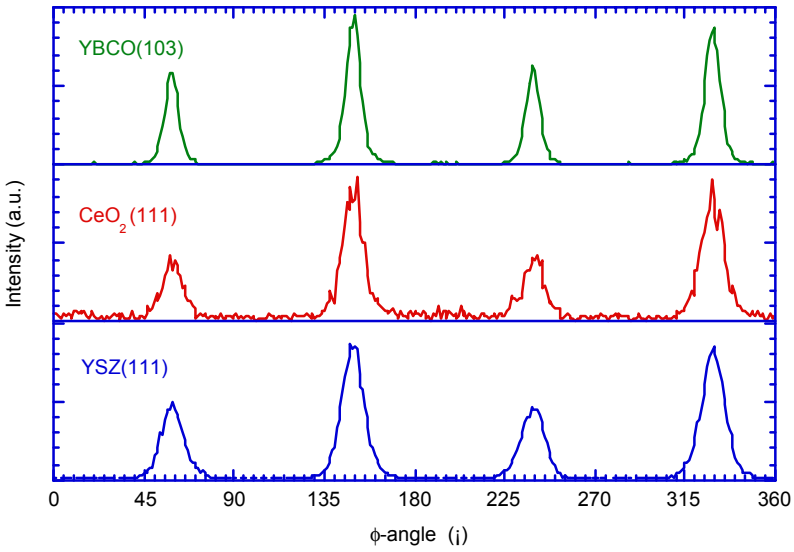

Fig. 31. X-ray ϕ-scan patterns of YBCO (103), CeO_2 (111), and YSZ (111), showing epitaxial growth.

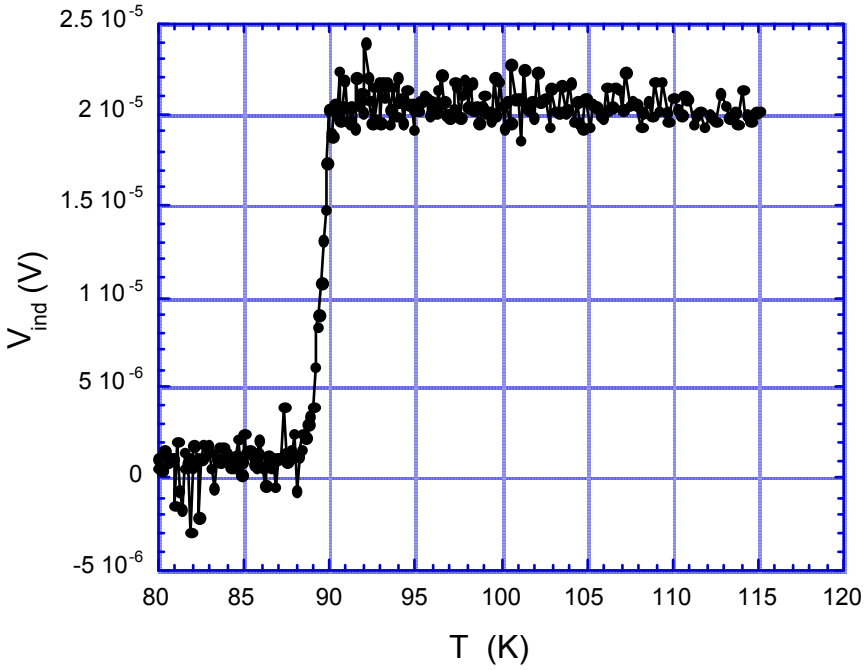

Fig. 32. Critical-temperature transition curve for YBCO film deposited on CeO_2-buffered IBAD-YSZ on HC substrate.

MOD process based on trifluoroacetate (TFA) has produced some of the highest J_c values. For that reason, we have worked to optimize the heat treatment of TFA-based YBCO precursors. The work initially made use of $LaAlO_3$ (LAO) single-crystal substrates, then progressed to using CeO_2-buffered YSZ single-crystal substrates. Because the ultimate goal is to use the TFA solution process with metallic substrates, in which case reactions between YBCO and the substrate may be difficult to control, we concentrated particularly on lowering the heat-treatment temperatures.

Acetates of Y, Ba, and Cu were weighed to a 1:2:3 molar ratio and dissolved in trifluoroacetic acid, and the mixture was refluxed for 4 h. The resulting solution was dried in air, and a methanol-based solution with a 1.5 M cation concentration was prepared. The solution was applied to LAO single crystals. The precursor film that formed was converted to an epitaxial YBCO film through two separate heat-treatment steps. During the first step, a uniform fluoride-containing solid film formed. During the second step, which was carried out in an Ar atmosphere with low-O_2 pressure, the fluorides were driven off, and a uniform, textured YBCO film formed. Various maximum temperatures were

investigated for the second step. The estimated O_2 content of the Ar was ≈10 ppm. After the second step, the composition of the YBCO film was determined by inductively coupled plasma/atomic emission spectroscopy.

The superconducting properties (T_c and J_c) of the films were measured by an inductive method. Microstructures were studied by SEM and energy-dispersive spectroscopy, and in-plane texture development was evaluated by XRD. The in-plane texture was quantified by measuring the FWHMs of YBCO (113) ϕ–scans. For analysis of c-axis alignment, FWHMs of the (005) and (007) peaks of YBCO were measured from Ω-scans for each sample. Information about second-phase formation, oxygen stoichiometry, c-axis alignment, and defect structures was obtained by Raman microspectroscopy.

Figure 33 shows plan-view SEM images of representative samples that were prepared at five temperatures for the second heat treatment. Pores and crystalline particles are observed to varying degrees on the surface of each sample; this is typical for YBCO films prepared by a postannealing process. Needle-shaped grains (which appear to be a-axis oriented) are frequently observed in the films prepared at 720 and 740°C (Figs. 33a and 33b). This indicates some grain misalignment, although the dominant texture of the films is c-axis vertical to the substrate. Far fewer a-axis grains can be seen in samples made at 750 and 760°C (Figs. 33c and 33d), suggesting that the c-axis verticality improves as the processing temperature increases. In the sample prepared at 780°C (Fig. 33e), the needle-shaped grains are absent; however, other large particles are observed. These large particles were mainly $BaCuO_2$, which suggests that the YBCO begins to decompose at temperatures between 760 and 780°C.

In-plane texture and c-axis alignment of the YBCO films were determined from the FWHMs of the ϕ– and Ω-scans. Figure 34 shows a (113) ϕ–scan for a film heated at 750°C; the average FWHM was ≈0.6° Figure 35 presents a plot of the variation of the FWHMs of the ϕ–scan with heat-treatment temperature. The FWHM values ranged from 0.55 to 0.8°.

FWHMs of Ω-scans for the YBCO (005) and (007) reflections are shown in Fig. 36 as a function of heat-treatment temperature. The FWHMs were 0.38° at minimum and 0.68° at maximum, and were not obviously correlated with temperature. The FWHMs from ϕ- and Ω-scans obtained by other groups are commonly ≈1.5 and 0.5°, respectively. In general, our TFA-based YBCO films exhibited quite good in-plane and c-axis alignment.

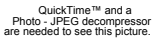

(a)

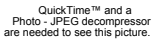

(b)

Fig. 33. SEM photomicrographs of YBCO films made by the TFA process at (a) 720, (b) 740, (c) 750, (d) 760, and (e) 780°C during the second heat treatment.

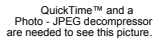

(c)

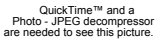

(d)

Fig. 33. (Contd.)

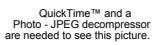

(e)

Fig. 33. (Contd.)

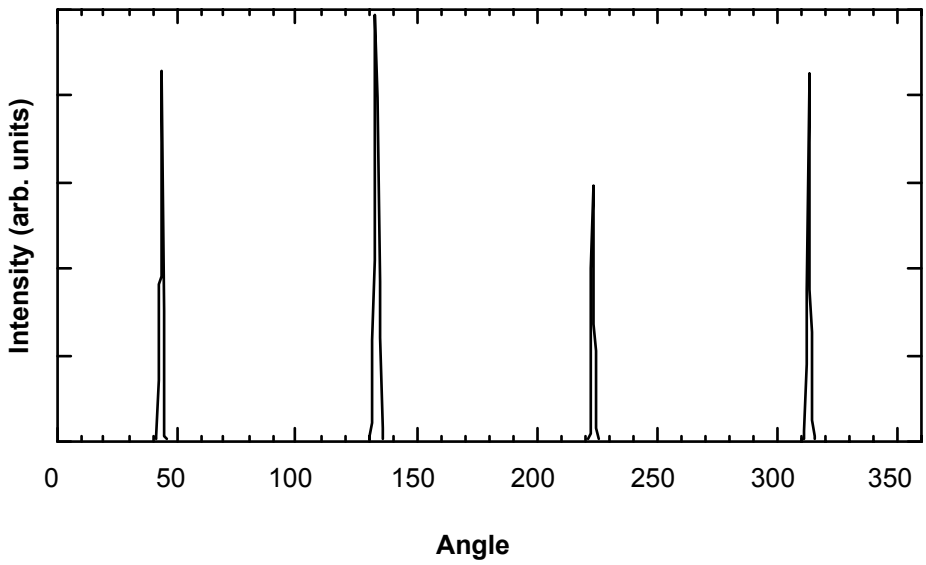

Fig. 34. ϕ–scan of YBCO film heat treated at 750°C.

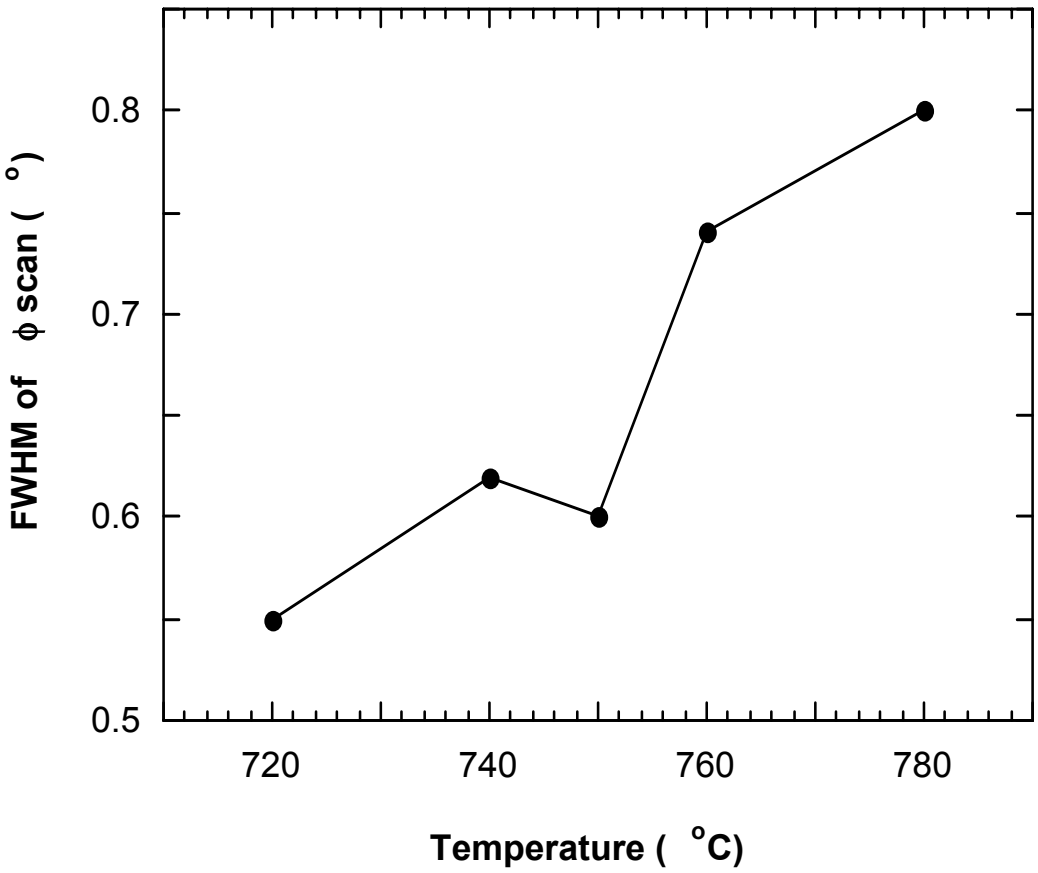

Fig. 35. FWHMs of ϕ–scan vs. temperature during second heat treatment of samples made by the TFA process.

Raman microspectroscopy was used to investigate the effect of heat treatment temperature on c-axis alignment, defect structures, oxygen stoichiometry, and second-phase formation. Figure 37 shows representative Raman spectra for samples processed at each of the five heat-treatment temperatures. The spectra were recorded in the xx/yy mode, i.e., with the laser excitation and observation directions perpendicular to the substrate and hence (presumably) also perpendicular to the a-b planes of all epitaxial YBCO grains. In this configuration, a perfectly epitaxial, defect- and impurity-free YBCO film should exhibit only one band (marked with an inverted triangle in Fig. 37) between 200 and 800 cm^{-1}. This band, nominally at ≈340 cm^{-1}, is the out-of-phase O2/O3 mode of YBCO.

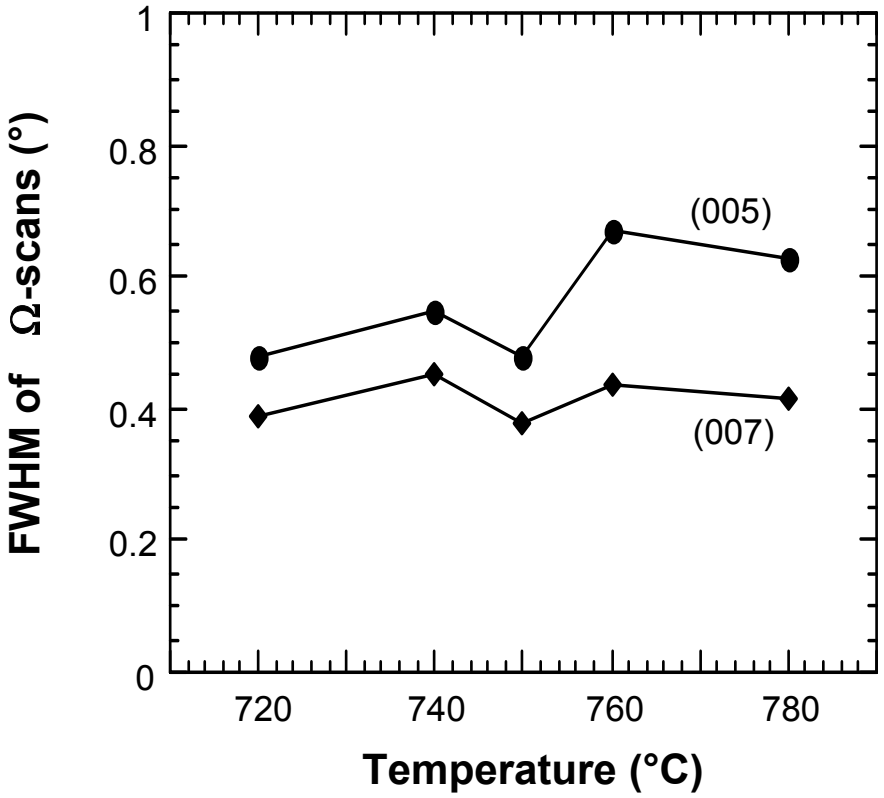

Fig. 36. FWHMs [Ω-scans of (005) and (007) XRD peaks] of samples made by the TFA process vs. temperature during second heat treatment.

The presence of other bands is generally an indication of defect structures, poor c-axis alignment, and/or impurity phases. For example, the band near 225 cm^{-1} has been attributed to the presence of broken M-O chain structures, which can exist on a nanoscopic, microscopic, or macroscopic scale. This band was rarely observed for films heat treated at 740–760°C. Occasionally, a small band was observed in this region for samples heat treated at 720°C, which may suggest imperfect connectivity between the YBCO grains. Some samples heat treated at 760°C also showed evidence of the band at 225 cm^{-1}, but it became much stronger when the heat-treatment temperature was increased to 780°C. The band at 225 cm^{-1} also tended to appear when the $BaCuO_2$ band at ≈630 cm^{-1} (marked as BC in Fig. 37) was intense. This findng indicates that the presence of $BaCuO_2$ may be related to the imperfect grain connectivity.

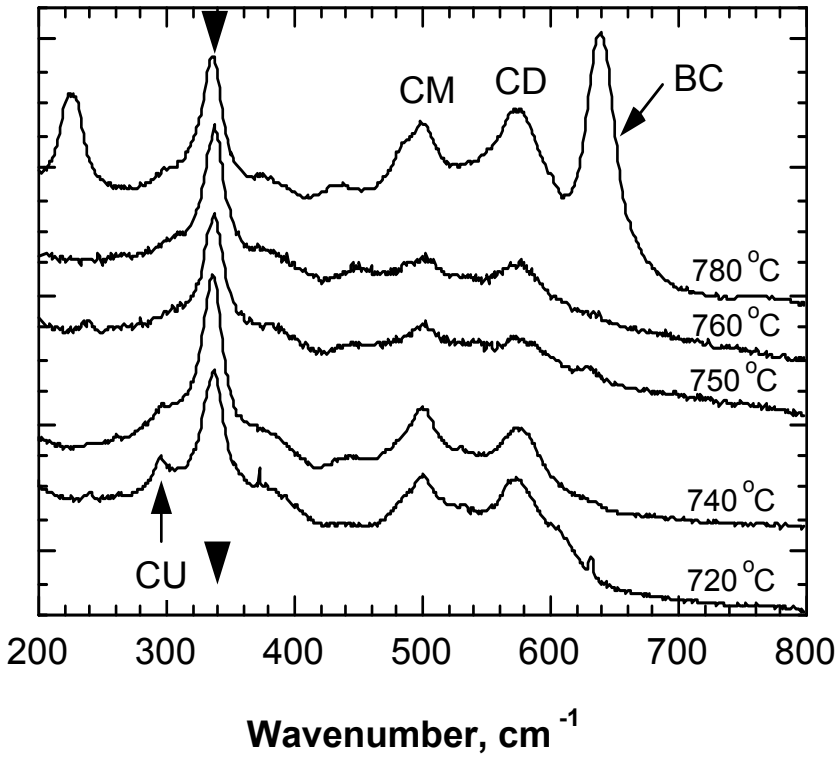

Fig. 37. Raman spectra for YBCO films made by the TFA process at the second heat-treatment temperatures shown.

For films heat treated at 780°C, two types of spectra were often observed: one that showed a strong CuO band and the other that showed a strong BC band. The spectrum for a sample made at 780°C (Fig. 37) shows a strong BC band but a very weak CuO band. The position of the CuO band is marked by CU in the spectrum for a sample made at 720°C. The appearance of CuO and $BaCuO_2$ bands suggest that YBCO starts to decompose near 780°C.

The band marked CM in Fig. 37 is the O4 phonon of YBCO. In the xx/yy configuration, the intensity of this mode should be minimal if the YBCO film is perfectly epitaxial. The intensity of this mode relative to the 340 cm^{-1} phonon is, in essence, a measure of the degree of c-axis misalignment. Using this relationship, Fig. 37 shows that the samples heat treated at 720, 740, and 780°C exhibited the largest degree of c-axis misalignment; samples heat treated at 750 and 760°C showed considerably less misalignment.

The peak frequency of the CM band provides an approximate measure of the oxygen stoichiometry, x, of $YBa_2Cu_3O_x$ (YBCO). For tetragonal YBCO, the value of x is expected to be near 6 and the CM peak frequency near 480 cm^{-1}, whereas the value of x is expected to be near 7.0 and the CM mode peak frequency near 500 cm^{-1} for othorhombic YBCO. The CM mode peak frequency was near 500 cm^{-1} for all of the samples, indicating that the YBCO phase is orthorhombic in all cases.

The band near 590 cm^{-1} (marked as CD in Fig. 37) has been attributed to cation disorder in the YBCO lattice. Like the CM mode, the CD band is much less prevalent for samples processed at 750 and 760°C.

The sharpest superconducting transitions were observed with samples that were prepared between 740 and 760°C, the temperature range that also yielded the best YBCO phase purity. Figure 38 shows the results of inductive J_c measurements on samples prepared at the five heat-treatment temperatures. Not surprisingly, the highest J_c value (1.3 MA/cm^2) was obtained for the sample heat treated at 750°C, where the Raman results suggest there is the least cation disorder and c-axis misalignment. Using these conditions, additional YBCO thin films with high T_c and J_c were prepared on LAO single crystals.

The heat-treatment conditions for the TFA process with LAO single-crystal substrates were not applicable to CeO_2-buffered YSZ single crystals. When YBCO was prepared on CeO_2/YSZ by the same procedure as YBCO on LAO single crystals, YBCO on CeO_2/YSZ did not exhibit a superconductor transition. The loss in superconductivity apparently resulted from reactions between YBCO, or its precursor, and the substrate. To improve the heat treatment procedure and minimize these reactions, we considered that fluorine removal is governed by the following equation:

$$H_2O + 2F^- \Leftrightarrow 2HF + O^{2-}. \quad (1)$$

Inside a TFA sample, water vapor reacts with BaF_2 to remove fluorine in the form of HF gas. The corresponding reaction constant is

$$K = [HF]^2[O^{2-}]/[H_2O][F^-], \quad (2)$$

where K is a function of temperature, and the concentration of fluorine is expressed as

$$[F^-] = K\,[HF]^{\,2}\,[O^{2-}]/[H_2O]. \quad (3)$$

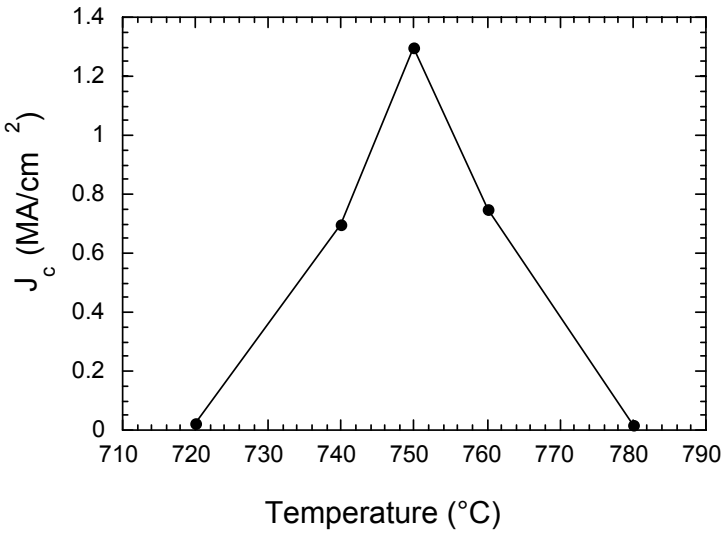

Fig. 38. Inductive J_c of YBCO made by TFA process vs. processing temperature.

The desired direction for this reaction is toward a decrease in the concentration of fluorine ions ($[F^-]$). Equation 3 shows that the removal of fluorine should be enhanced by reducing the HF concentration. This could be accomplished by increasing the flow rate of gas during heat treatment or by performing the heat treatment under a partial vacuum. Fluorine removal could also be enhanced by increasing the partial pressure of water during heat treatment. In addition, these various methods to facilitate fluorine removal might allow the heat treatment to be done at a reduced temperature, which would minimize diffusion between the layers and perhaps eliminate reactions between the layers.

Based on these considerations, YBCO precursor samples on CeO_2/YSZ substrates were processed by two types of heat treatments. In one type, the HF concentration was minimized by significantly increasing the flow rate of gas during heat treatment; all other conditions were kept the same. In this case, samples coated with YBCO precursor were heat treated at 750°C in argon saturated with water at room temperature (partial pressure of water ≈23 torr). In the other type of heat treatment, the removal of HF was facilitated by using a partial vacuum (total pressure ≈1/3 atm). In this case, argon was saturated with water at 60°C (partial pressure of water ≈150 torr), and the heat treatment temperature was decreased to 730°C.

Figure 39a shows the T_c curve from a sample that was prepared with a high gas flow rate. The transition width was 5 K, and the onset temperature was >90 K. From an engineering point of view, however, this is not ideal, because it involves flowing large amounts of high-purity gas. Figure 39b shows a sharper superconducting transition for a sample that was fabricated in a partial vacuum. These results indicate that a partial vacuum may provide important benefits during the heat treatment of TFA-based coated conductors.

2.1.4 Current Transport across YBCO Grain Boundaries

There is evidence that the J_c of grain boundaries (GBs) in high-T_c superconductors does not drop as quickly with magnetic field (H) as might be expected from a simple Josephson junction model, in which the envelope of the Fraunhofer pattern goes as 1/H. In very low fields, pinning of Josephson vortices by the meandering of thin-film, [001] tilt, bicrystal GBs in YBCO has been shown [4] to enhance J_c. However, as the spacing between Josephson vortices decreases in higher fields, this long-wavelength pinning potential due to meandering becomes less effective. Gurevich and Cooley [5] proposed a new mechanism for an enhanced GB critical current arising from pinned Abrikosov vortices in the banks of a GB, which present a static, quasi-periodic pinning potential to pin GB vortices. Their calculations, which predict a peak in $J_c(H)$, are in the low-field limit, but the central concept can be extrapolated to higher fields.

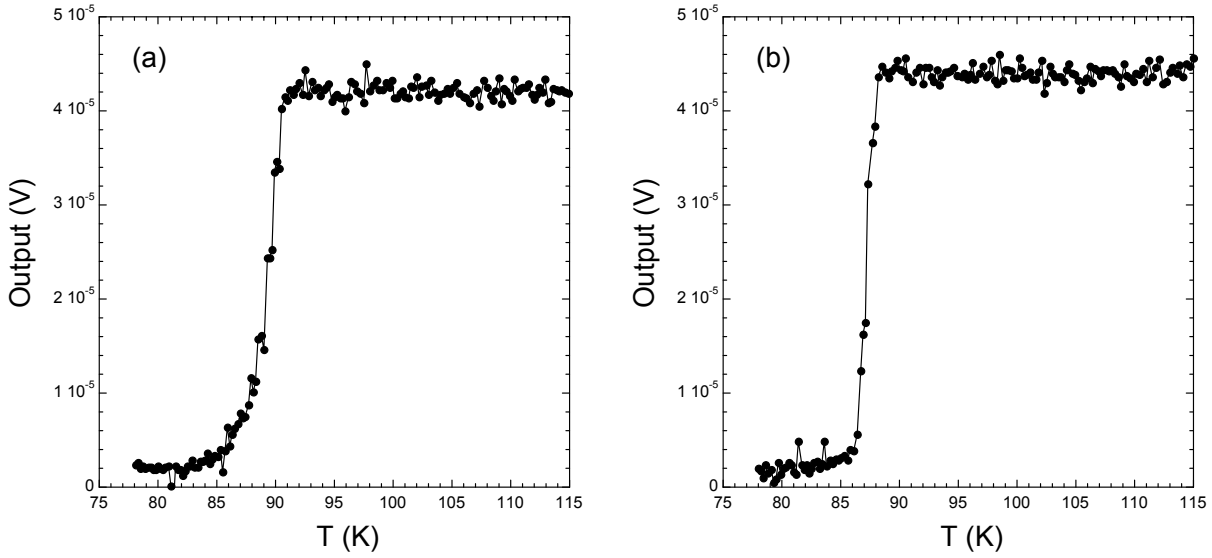

Fig. 39. Inductive T_c plots for TFA YBCO films on CeO_2/YSZ: (a) film processed with high gas flow rate and (b) film processed in partial vacuum.

This pinning mechanism exhibits optimal effectiveness if the Abrikosov and Josephson vortices have the same spacing, i.e., when the magnetic flux density in the GB and the banks are equal. In that case, there is one potential well for pinning per Josephson vortex.

We have obtained data as a function of magnetic field on three types of bicrystal GBs of high-T_c superconductors that show a peak in the critical current and an unusual inverse hysteresis upon field cooling. These results support a new mechanism for an enhanced GB critical current that arises from interactions of GB vortices with pinned Abrikosov vortices in the banks of a GB, as suggested by Gurevich and Cooley. A substantial fraction of this enhancement also occurs upon exceeding the critical current of the grains after zero-field cooling. A bulk GB and an isolated GB from a coated conductor showed qualitatively identical results, whereas a 24° artificial GB made on a bicrystal substrate showed enhancements of at least a factor of 10 (Figs. 40 and 41).

We have discovered another method, besides field cooling, to introduce Abrikosov vortices into the grains and enhance the critical current. After cooling in zero field, if the current exceeds the threshold for flux creep, Abrikosov vortices are injected into the banks of the GB. These can play the same pinning role as the Abrikosov vortices introduced by field cooling, and thus increase the critical current of the GB. The increase can be a significant fraction (≈1/2) of the increase obtained by field cooling. However, by analyzing the temporal voltages during current pulses, evidence was found for heating effects. Thus, the injection of vortices into the grains could be akin to field cooling. Shorter pulses (≈2 μs) eliminated heating, so the much smaller, but definitive, enhancements of critical current must be due to Lorentz-force-driven vortex injection. The enhancements depended mostly on the magnitude of the pulse current and only weakly on the number of pulses.

In summary, we found strong support for the conceptual model of Gurevich and Cooley, in which GB vortices are pinned by Abrikosov vortices in the banks of the GB. This conclusion has some interesting and possibly important consequences. It provides a mechanistic basis to understand the high-field behavior of granular high-T_c superconductors. It also points to the potential for improved performance (i.e., higher critical currents), in applications where the critical current is affected by GBs, by decorating the GB banks with pinned Abrikosov vortices.

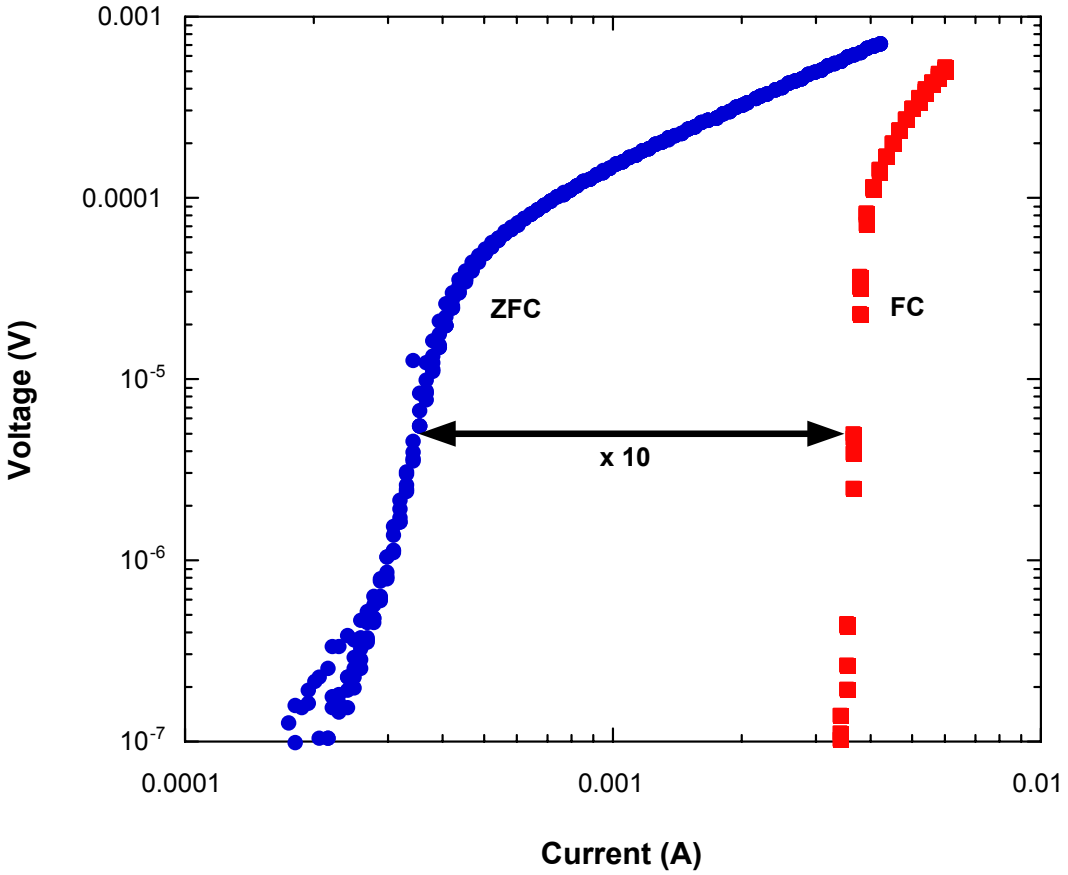

Fig. 40. Voltage vs. current across bicrystal grain boundary at 35 K. Field-cooled specimen exhibits much larger J_c. ZFC = zero-field-cooled; FC = field-cooled.

2.1.5 Characterization of Coated-Conductor Composition and Microstructure

Over the past year we have been conducting studies aimed at developing and applying molecular spectroscopy and synchrotron X-ray characterization methods to coated-conductor substrates, buffer layers, precursors, and fully processed samples. The molecular spectroscopy measurements involve use of Raman microspectroscopy and Fourier transform infrared (FTIR) spectroscopy. The X-ray measurements are being performed at ANL's Advanced Photon Source (APS) facilities available at the insertion device beamline of the Materials Research Collaborative Access Team (MRCAT) and at the beamlines of the Basic Energy Sciences Synchrotron Research Center. Examples are given below of the

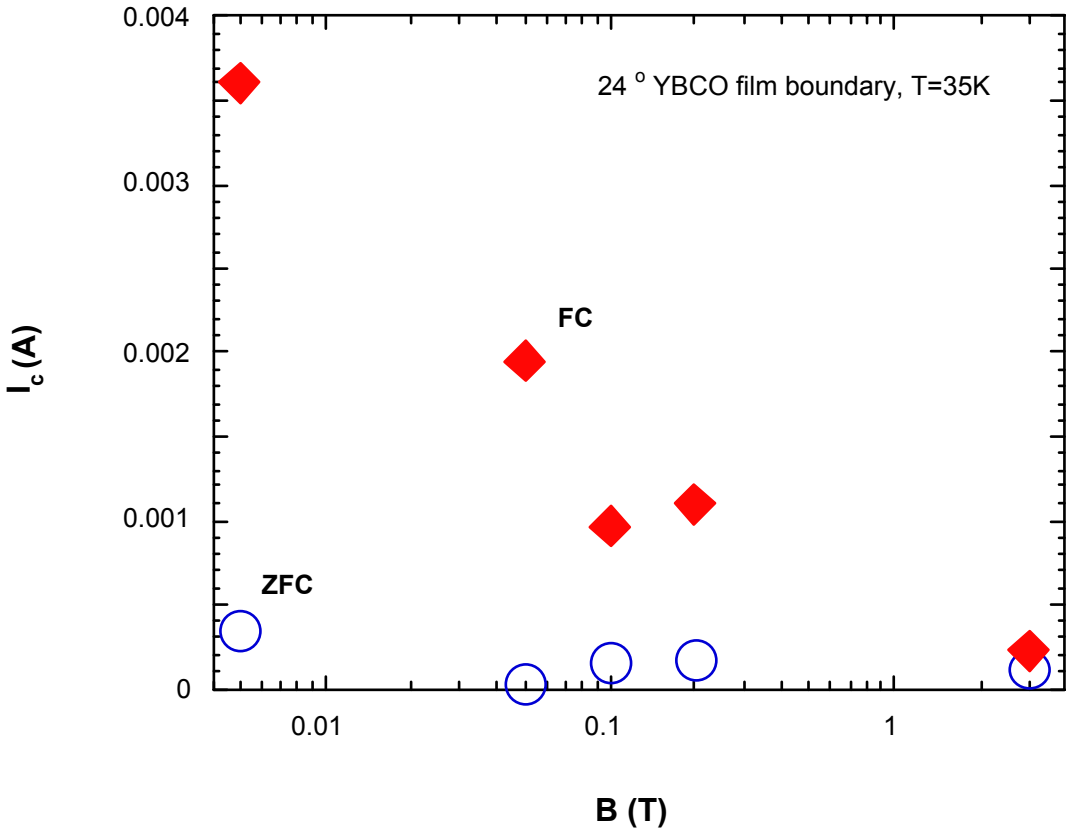

Fig. 41. Critical current values for bicrystal grain boundaries at 35 K. Field-cooled specimens exhibit much larger J_c.

types of information that we are obtaining from these measurements. An important motivation for this work is to investigate characterization techniques that have potential as on-line process-monitoring tools at coated-conductor manufacturing facilities.

Raman Microscopy of Coated-Conductors

We have previously described how Raman microscopy (RM) has been used to analyze fully processed coated-conductor specimens produced either by PLD or spin-coating of TFA precursors. In particular, we pointed out how Raman spectroscopy data obtained in the microscope mode provide information about YBCO c-axis alignment, oxygen stoichiometry of the superconducting phase, cation disorder, microstructural continuity, phase purity, and spatial uniformity of composition. We illustrated that (1) the c-axis quality of a YBCO thin film could be determined by comparing the relative intensities of the out-of-phase O(2,3) phonon (≈335 cm^{-1}) and the (O4) phonon (≈500 cm^{-1}); (2) YBCO oxygen

stoichiometry could be estimated from the measured frequency of the O(4) phonon; (3) a normally inactive phonon in the 580–600 cm^{-1} region has been construed by some to be an indicator of cation disorder in the YBCO phase; (4) another normally inactive phonon in the vicinity of 225 cm^{-1} may be attributable to badly disrupted metal-oxygen bonding networks; and (5) small concentrations of $BaCuO_2$ and CuO produce characteristic phonons at ≈640 cm^{-1} and ≈290 cm^{-1}, respectively.

More recently, dozens of PLD- and TFA-type YBCO-coated-conductor films produced at ANL have been examined by RM, and the RM results were correlated with performance characteristics of the samples. As a result, the performance (in terms of both T_c and J_c) can now be qualitatively predicted in virtually all cases, and the causes of relatively poor performance can be identified rapidly and inexpensively. Typically, the root causes have been poor c-axis alignment of the YBCO (specifically when the seed surface is noninclined), appreciable cation disorder, and (to a lesser extent) the presence of $BaCuO_2$. Progress is being made on understanding issues related to c-axis alignment, and these will be discussed in a subsequent report. In this report, we present results that are pertinent to the issues of cation disorder and $BaCuO_2$.

The notion that the appearance of the 580–600 cm^{-1} "inactive" phonon is due to cation disorder (e.g., cation vacancies and/or cations on the wrong site) is not uniformly accepted and requires further corroboration. In an effort to provide corroboration, we investigated the Raman spectra of YBCO single-crystal specimens that were doped to varying degrees on the copper site with aluminum, cobalt, nickel, or zinc. The studies were conducted in the RM configuration, with the excitation laser and observation directions parallel to the YBCO crystallographic c-axis (as is typically done for coated-conductor samples). The finding was ostensibly the same in all cases: as the concentration of the dopant increased, the intensity of the 580–600 cm^{-1} phonon tended to increase.

A typical RM result is shown in Fig. 42 for the case of aluminum substitution on the copper site of YBCO. Aluminum produced the largest effect, cobalt the next largest, and nickel and zinc comparably the least. This result is expected because aluminum offers the largest mass difference relative to copper, whereas nickel and zinc, which straddle copper in the periodic table, offer the least mass difference. Ignoring differences in lattice force constants that accompany the metal atom substitutions, we found that the kinematics of the YBCO phonons are least likely to be affected by nickel and zinc substitution for copper and most likely to be affected by aluminum substitution. In any case, the 580–600 cm^{-1} phonon is clearly influenced by cation substitution, which in essence constitutes a simulated form of cation disorder. The cation disorder

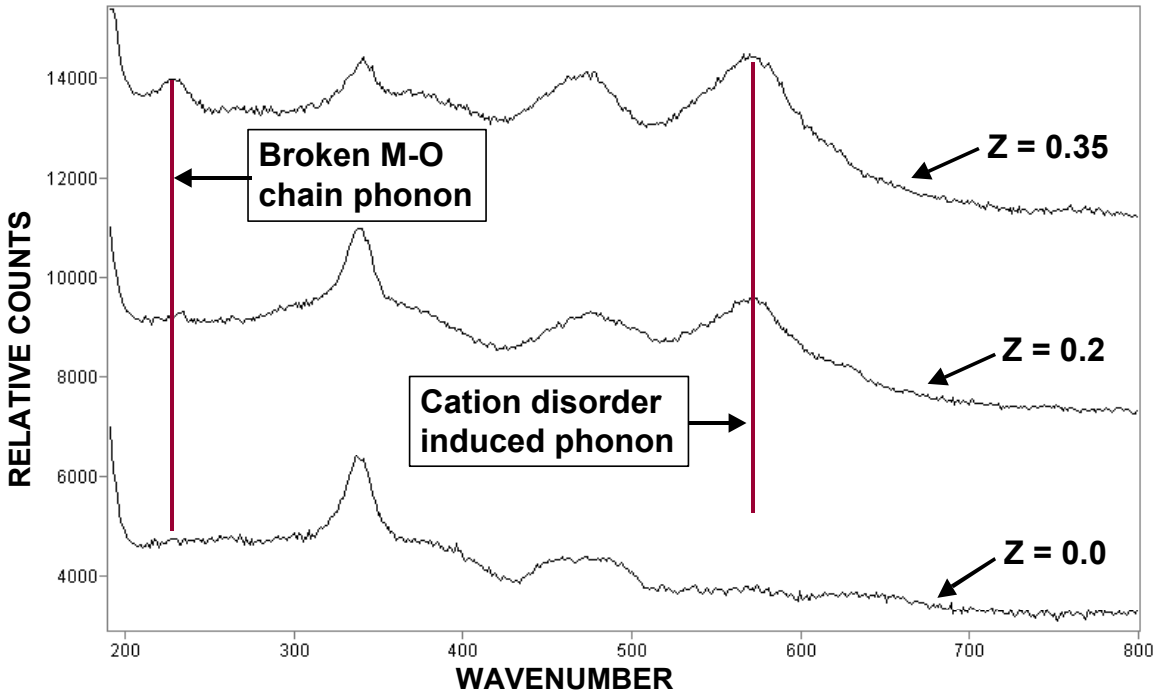

Fig. 42. Raman microprobe spectra of $YBa_2Cu_{3-z}Al_zO_x$ single crystals with z = 0.0, 0.2, and 0.35. Taken with the excitation laser and observation directions parallel to the crystallographic c-axis.

associated with substitution on the copper site of YBCO is known to degrade T_c and J_c. A more detailed study of the causes and consequences of cation disorder in YBCO-coated conductors seems warranted by the results that have been obtained thus far.

In Raman microscopy, one combines white-light microscopy with the recording of Raman spectra of phases in the field of view of the white light. In viewing coated-conductor samples that show detectable quantities of $BaCuO_2$, the surfaces of the YBCO films often appear to be decorated with crystalline nodules. Investigation of these samples by imaging Raman microscopy (IRM) has revealed evidence for several types of $BaCuO_2$ dispersions. Large isolated crystallites of $BaCuO_2$ tend to form if the processing temperature is too high or the local cation stoichiometry varies too far from the prescribed value; however, these kinds of processing issues were resolved at an early stage and are no longer relevant to our TFA- or PLD-based samples.

The IRM results in Fig. 43 are typical of YBCO-coated conductor samples with moderate performance that nonetheless contain small but detectable quantities of $BaCuO_2$. The sample in this case was a TFA-based YBCO film on a

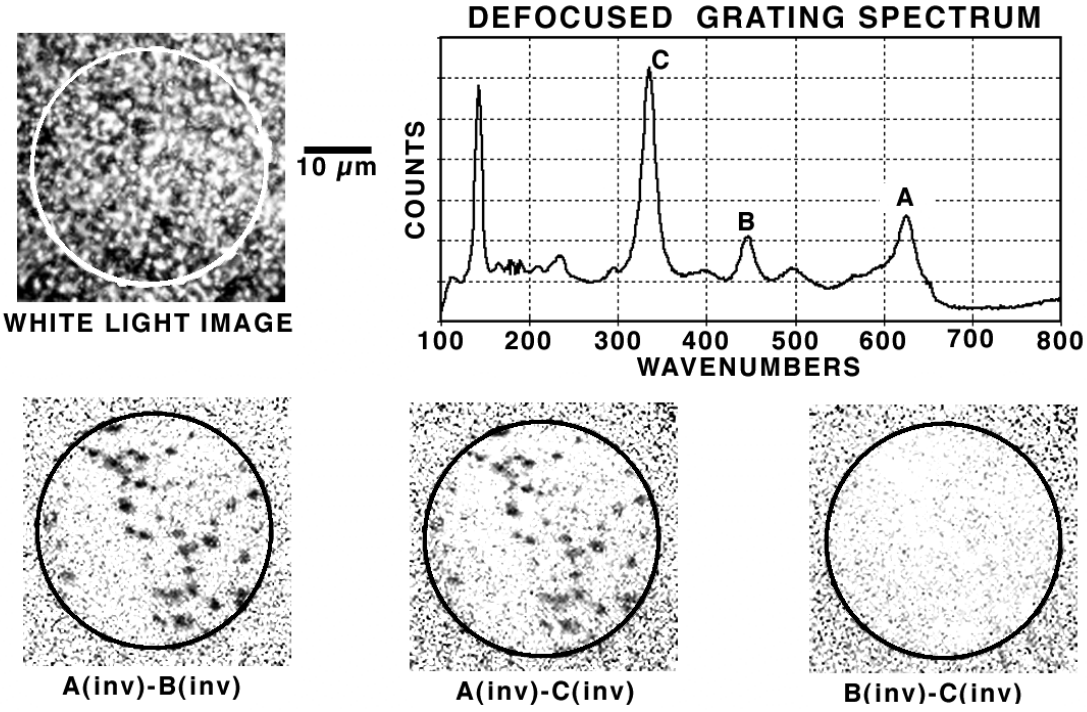

Fig. 43. Imaging Raman microprobe results for TFA-type YBCO film on CeO_2-buffered YSZ single crystal. Black spots in images A(inv)-B(inv) and/or A(inv)-C(inv) indicate size and location of $BaCuO_2$ crystallites on YBCO film surface.

CeO_2-buffered YSZ single crystal. The defocused Raman spectrum in Fig. 43 was obtained from the circled region (≈40 μm in diameter) in the white-light image. Band A (upper right, Fig. 43) is the most prominent $BaCuO_2$ phonon, and bands B and C are phonons of YBCO. The Raman images of bands A, B, and C, which essentially show where $BaCuO_2$ and YBCO are in the imaged region, were recorded, and their gray scales were inverted. In the inverted gray scales, the "presence" of a phase is indicated by black, and the "absence," by white. In the image A(inv)-B(inv), the black spots indicate where $BaCuO_2$ is relative to YBCO, and (as a consequence of the gray-scale arithmetic) the whitest regions indicate where YBCO is relative to $BaCuO_2$. As expected, image A(inv)-C(inv) produces much the same result as A(inv)-B(inv) because C is also a phonon of YBCO. The white-out in image B(inv)-C(inv) occurs because bands B and C are from the same phase; in this case, white signals the equivalence of B and C. The results (Fig. 43) indicate that the $BaCuO_2$ exists as small (micrometer-size) nodules spread over the surface of the YBCO film.

The IRM results in Fig. 44 are for TFA-based YBCO on an unbuffered LAO single crystal. Comparison of the intensities for bands A and C in the defocused Raman spectrum indicates a greater relative presence of $BaCuO_2$ (versus YBCO)

than was seen for the sample in Fig. 43 and substantially more cation disorder (evidenced by band B). The blackest and whitest regions in image A(inv)-C(inv) of Fig. 44 show where the $BaCuO_2$ and YBCO are, respectively. (Note the larger size of the $BaCuO_2$ patches in Fig. 44 when compared with those in Fig. 43.) The observations that $BaCuO_2$ crystallites are less dominant in image A(inv)-B(inv) than in image A(inv)-C(inv), and that there are obvious dark-gray to black regions in B(inv)-C(inv) suggest that the YBCO cation disorder (which stimulates band B) is more prevalent near the $BaCuO_2$ crystallites. This observation suggests that the persistence of second phases is connected with cation disorder, and that their dissipation might eliminate the disorder.

While removing the Ag cap layer from a PLD-YBCO film on single-crystal YSZ, we found that surface-bound $BaCuO_2$ can be removed from YBCO by a brief soak in ammoniacal peroxide solution. The Raman results in Fig. 45 show that the phonons attributable to $BaCuO_2$ disappear after the soak. This confirms our conclusion from IRM studies that $BaCuO_2$ tends to form on the surface of YBCO films. Also, the disappearance of the band at ≈225 cm^{-1} after the soak is consistent with prior Raman studies [6] indicating the presence of a true phonon

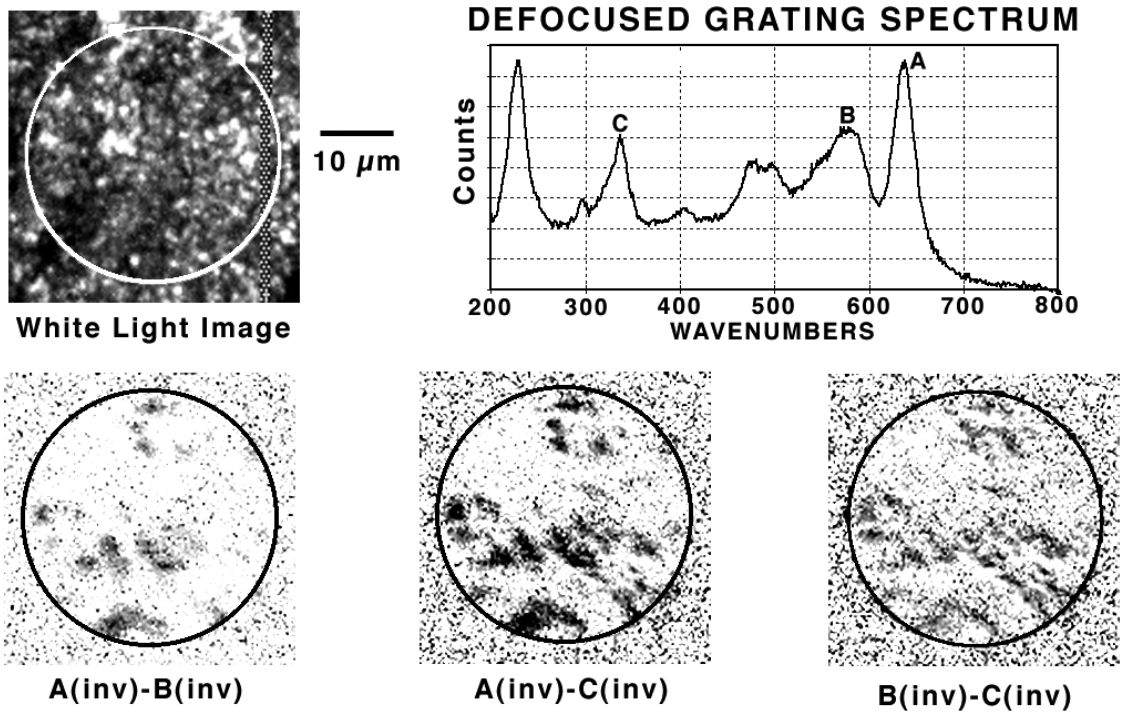

Fig. 44. Imaging Raman microprobe results for TFA-type YBCO film on an unbuffered $LaAlO_3$ single crystal. Black spots in image A(inv)-C(inv) indicate the size and location of $BaCuO_2$ crystallites on YBCO film surface.

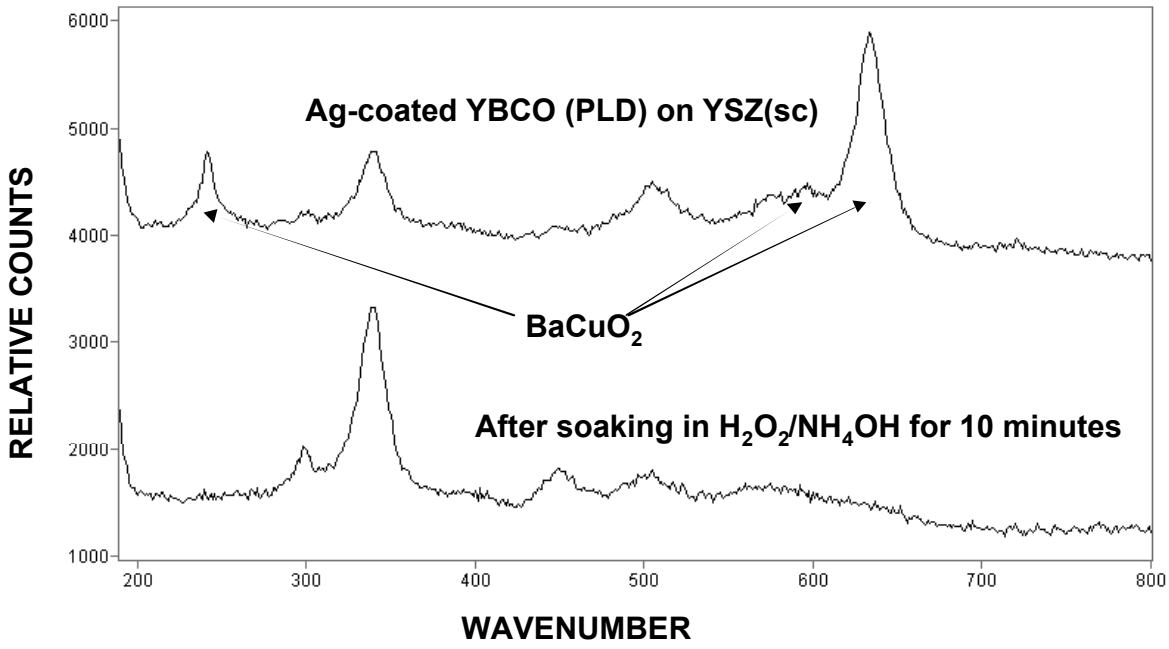

Fig. 45. Raman microprobe spectra of PLD-YBCO film on single-crystal (SC) YSZ before and after removing sputter-deposited silver contact layer by soaking in ammoniacal peroxide solution.

of $BaCuO_2$ near this frequency, a frequency that has also been associated with disrupted metal-oxygen bonding networks. This finding shows that the Raman bands near 225 cm^{-1} must be interpreted with care when other evidence clearly indicates the presence of $BaCuO_2$ (i.e., at ≈640 cm^{-1}).

Characterization of Seed and Buffer Layers for Coated Conductors

Raman microscopy, FTIR spectroscopy, X-ray diffraction, and X-ray reflectivity methods are also being used to examine the composition and structure of substrate surfaces, seed layers, and buffer layers, as well as the interfaces between them. Figure 46 shows the Raman spectra from a set of CeO_2 thin films produced by e-beam evaporation on deformation-textured (DT) nickel.

The Raman spectra in Figs. 46a and b are typical of the spectra obtained for CeO_2-buffered nickel specimens. The spectra in Figs. 46a and 46b were obtained after annealing at 550°C and 750°C, respectively. The intense, sharp, symmetrical band at ≈467 cm^{-1} is the lone Raman-active phonon of cubic CeO_2 in these two spectra. The two weaker/broader bands at ≈1100–1300 cm^{-1} and ≈1500–1600 cm^{-1} are commonly observed in Raman spectra of oxidized nickel surfaces and pure NiO, and have been attributed to the second-order longitudinal optical (2LO) mode (≈1100–1300 cm^{-1}) and the two-magnon (2M)

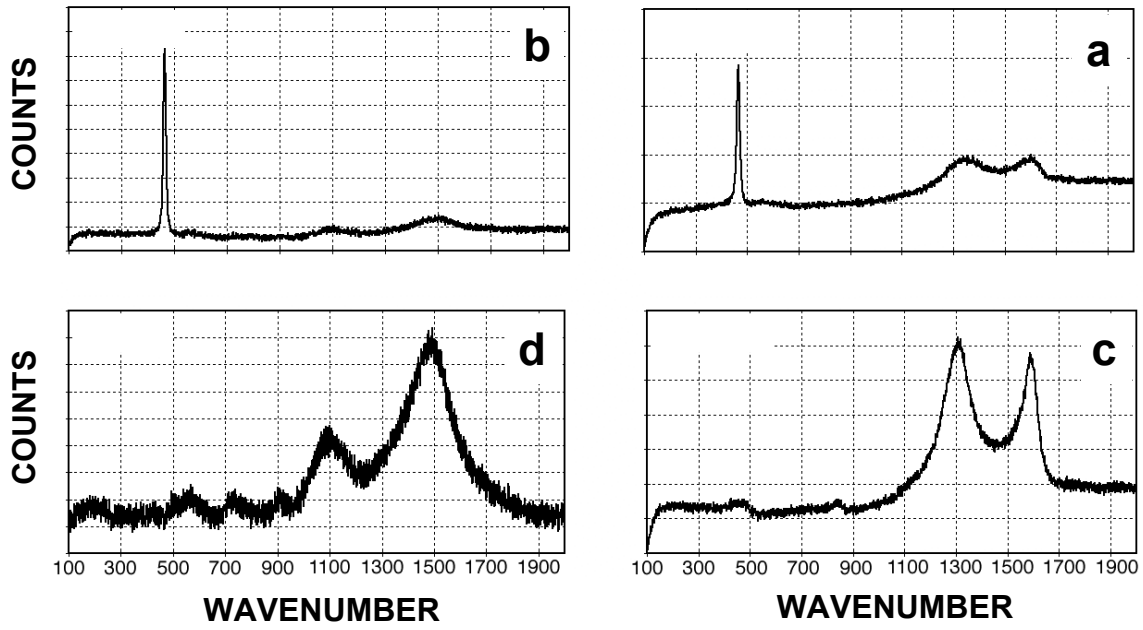

Fig. 46. Raman spectra of ≈200-nm-thick, e-beam-deposited CeO_2 on roll-textured nickel after annealing at (a) 550°C and (b) 750°C, showing evidence of thin NiO layers under the CeO_2 film. Raman spectra in (c) and (d) are for as-rolled nickel after annealing at 550°C and 750°C, respectively.

mode (≈1500≈1600 cm^{-1}) of cubic NiO. (Cubic NiO does not produce a first-order Raman spectrum.) Figures 46c and d are Raman spectra of as-rolled nickel foil annealed at 550°C and 750°C, respectively. Correlation/comparison of the spectra in Figs. 46a-d indicates that a residual NiO layer is present under the CeO_2 film after deposition and annealing. The shift in the frequency of the 2LO and 2M modes with annealing temperature appears to be associated with changes in the oxygen stoichiometry of the NiO layer and may, therefore, be a useful indicator of oxygen activity at the CeO_2/Ni interface. We intend to look for a correlation between this "indicated" oxygen activity and the performance (T_c and J_c) of YBCO deposited on CeO_2-buffered nickel substrates.

In addition to investigating the CeO_2/Ni interface in this series of samples, we studied the grain size of the CeO_2 films as a function of film thickness. Figure 47 shows the Raman spectra for CeO_2 films of three thicknesses, together with the spectrum of sintered polycrystalline CeO_2. Using an empirical relationship developed by Wang et al. [6], $\Gamma = 10 + (104/d)$, where Γ is the FWHM of the CeO_2 Raman band in cm^{-1}, and d is the average grain size in nm, we determined grain-size values. The average grain size increased with increasing film thickness and assumed a value that was approximately one-tenth of the film thickness. In the light of this finding, it seems worthwhile to search for a correlation between

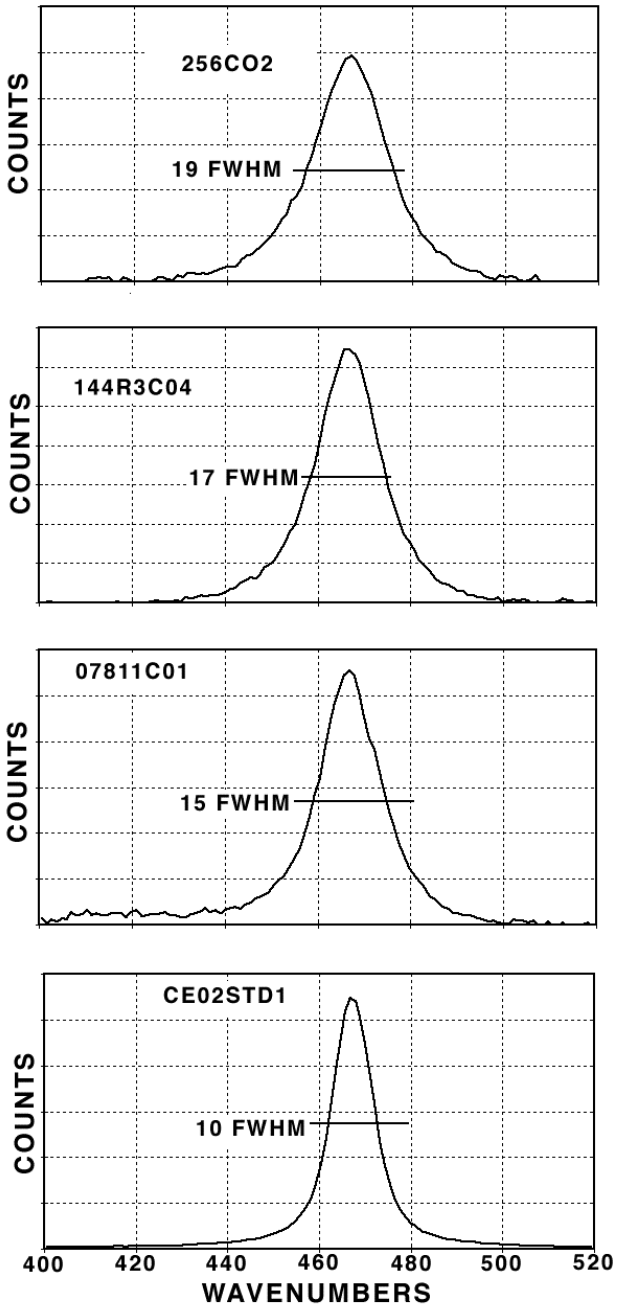

Fig. 47.
Raman spectra of CeO_2 films on roll-textured nickel, together with spectrum of sintered polycrystalline CeO_2.

YBCO-coated-conductor performance and the grain size of the underlying buffer layer. If such a correlation exists, then the grain size/thickness relationship should allow selection of the optimum buffer layer thickness.

We also began to study strains in seed and buffer layers, using a combination of molecular spectroscopy and X-ray diffraction. The strain that develops in thin crystalline films applied to templating substrates can be either tensile or compressive, depending on whether the film must "stretch" or

"compress" to match the lattice spacing and thermal expansion of the substrate. This stretching or compressing correspondingly stretches or compresses the lattice spacings and the chemical bonds in the film; these changes are manifested by small but measurable shifts in diffraction lines and phonon frequencies. An example of this response is shown in Fig. 48, the FTIR spectra for single-crystal LAO, single-crystal STO, and a thin film of STO on single-crystal LAO. These spectra were obtained by an attenuated total reflection (ATR) FTIR technique in which the sample is pressed against a silicon ATR element. The spectra contain optical modes of the respective single crystals, as indicated, plus a small uncompensated residual absorption due to the silicon ATR element. The LAO and STO single-crystal infrared spectra are in excellent agreement with prior work. The shift to higher wavenumber of the phonon STO1 in the topmost spectrum (where STO is a thin film on LAO) relative to its single-crystal value indicates the stress associated with compressing the cubic STO lattice (a = 2.7584 Å) onto the rhombohedral LAO lattice (a = 2.6825 Å).

We also measured the X-ray diffraction patterns of the STO single-crystal and the STO film on an LAO substrate that produced the FTIR spectra in Fig. 48. The frequency shift of the STO1 phonon from the single-crystal value (521 cm^{-1})

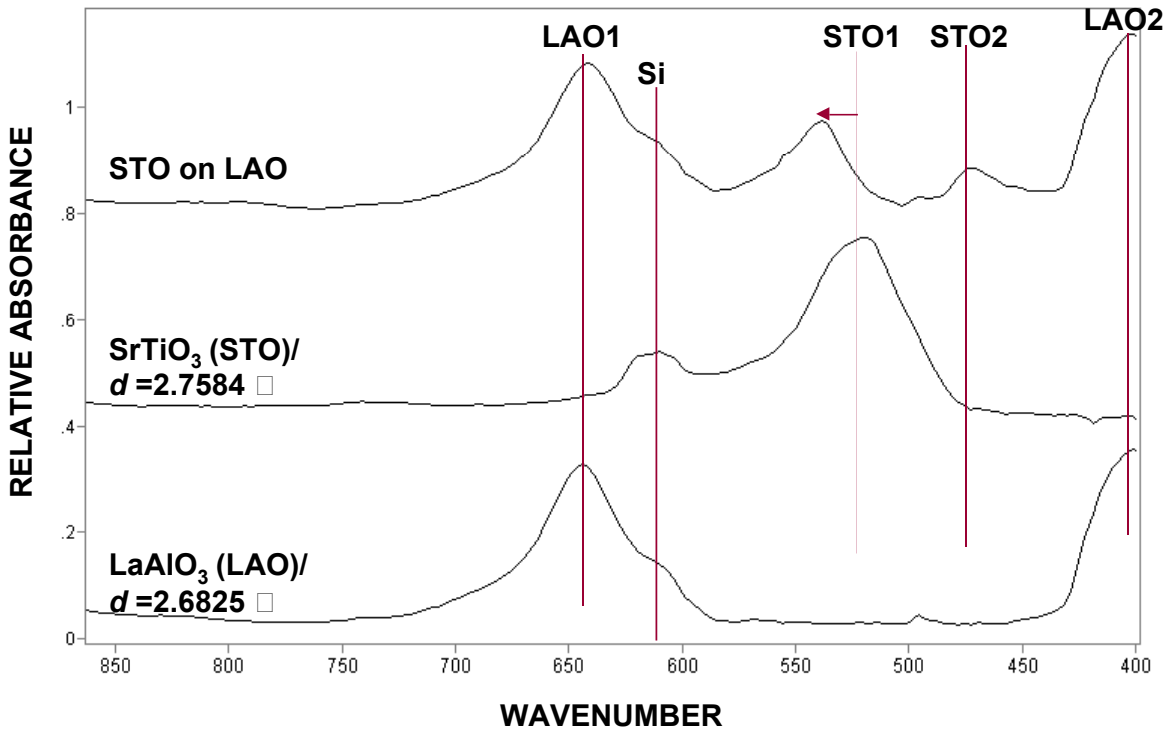

Fig. 48. Attenuated total reflection FTIR spectra of (from bottom to top) single-crystal $LaAlO_3$ (LAO), single-crystal $SrTiO_3$ (STO), and a thin film of STO on LAO.

to the strained-film value (538 cm^{-1}) is related to the change in lattice spacing of the strained STO film (relative to the single-crystal value) by the expression

$$(\nu_S - \nu_O)/\nu_O = -n\gamma(a_S - a_O)/a_O\,, \qquad (4)$$

where ν_S and ν_O are the strained-film and single-crystal values for the STO1 phonon, respectively; a_S and a_O are the strained-film and single-crystal values for the STO lattice spacing, respectively; n is a dimensionless parameter (equal to 2.0 for thin films); and γ is the Gruneisen parameter [7]. From the data in Fig. 48, we obtained a value of 0.033 for $(\nu_S - \nu_O)/\nu_O$, and from the X-ray data we obtained a value of -0.007 ± 0.001 for $(a_S - a_O)/a_O$. From these two values we determined that $\gamma = 2.4 \pm 0.4$. Because $(a_S - a_O)/a_O$ is directly related to strain in the crystalline film, having a value for the Gruneisen parameter of a seed or buffer layer material allows one to determine strain at the film/substrate interface from a vibrational spectrum, which during a continuous manufacturing process is generally easier to record than an X-ray diffraction pattern.

Monitoring Pyrolysis of TFA-Type YBCO Precursors

The TFA-based sol-gel process for producing YBCO films has considerable potential to lead to rapid low-cost fabrication of coated conductors. A key step in the TFA route is pyrolysis of the precursor. Decomposition of the anions in the deposited precursor can be significantly exothermic at temperatures >250°C. We have begun to explore the TFA decomposition process with two objectives in mind. One is to search for an optimum set of temperature/ramp-rate/oxygen-partial-pressure conditions; the second is to develop an in-situ reaction-monitoring methodology that will allow the progress of the decomposition reaction to be examined and, in the longer range, might also be applicable to on-line process monitoring.

In one set of recently completed measurements, FTIR spectroscopy was used to examine TFA precursor deposits on CeO_2-buffered YSZ single crystals that were quench-cooled at selected time/temperature points during a thermal decomposition study. The series of FTIR spectra shown in Fig. 49 was obtained by the method mentioned above in connection with the results in Fig. 48, wherein the precursor coating is pressed against a silicon ATR element. Spectrum a in Fig. 49 is from an as-deposited precursor before any heating. Four other, identically prepared, samples were placed in a furnace as a group and ramped to 210°C at ≈10°C/min. One sample was withdrawn upon reaching 210°C (b); another sample was withdrawn after a slow, 75-min ramp to 215°C (c); a third sample was withdrawn after an additional 75-min ramp to 220°C (d); the fourth sample was withdrawn after a rapid (20°C/min) ramp to 400°C (e). The six star-marked FTIR absorption bands in Fig. 49 are characteristic

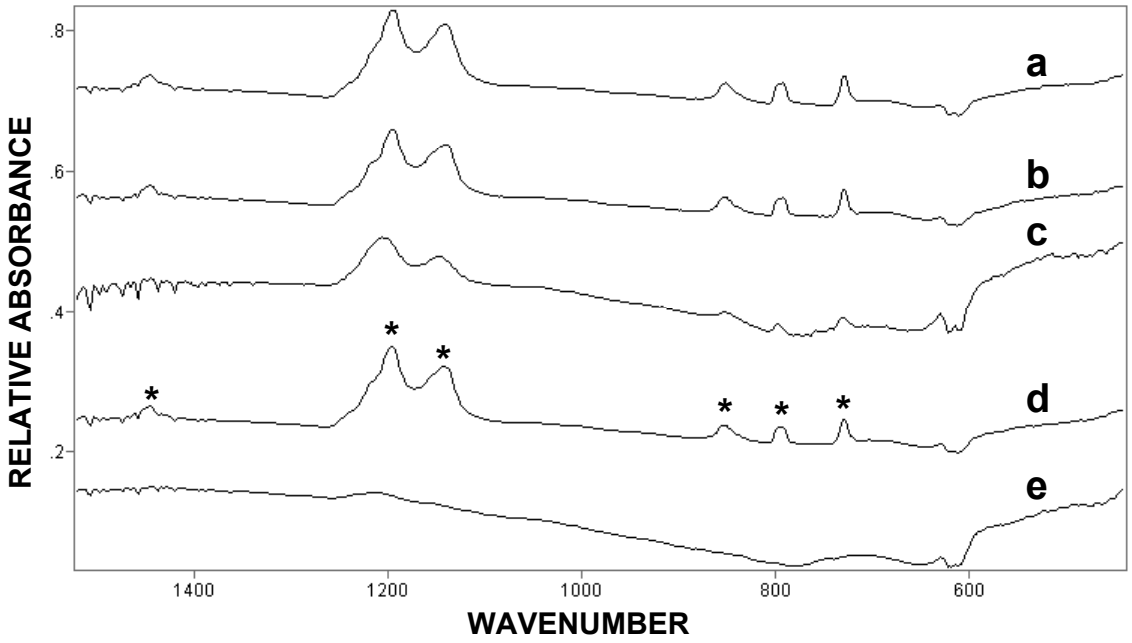

Fig. 49. FTIR spectra of five identical TFA-type YBCO precursor films on CeO_2-buffered YSZ single crystals after various stages of a single thermal treatment: (a) as-deposited, (b) after 10°C/min ramp to 210°C, (c) after additional 75-min slow ramp to 215°C, (d) after an additional 75-min slow ramp to 220°C, and (e) after additional 20°C/min ramp to 400°C.

vibrational modes of the TFA anion. Note that little change occurs in the number of bands, their intensities, and their profiles until the final ramp to 400°C, at which point there is no remaining spectroscopic evidence of the TFA anion.

This finding is consistent with recently published differential thermal analysis results, which show that decomposition of the TFA precursor starts to occur in the 210–270°C range. Based on the results in Fig. 49, the decomposition starts at a temperature above 220°C and is complete by the time the temperature reaches 400°C, as indicated by spectra d and e in Fig. 49. Temperatures in the 220–400°C range could be explored in greater detail by using an FTIR technique that allows spectra to be recorded at high temperatures.

X-ray Reflectivity Analysis of Deformation-Textured (DT) Nickel Substrates

We have begun to explore the utility of synchrotron-based X-ray reflectivity (XRR) analysis for characterizing the surface morphology and roughness of DT nickel substrates before and after application of buffer layers. Background-corrected XRR results are shown in Fig. 50a for bare DT nickel foil, Gd_2O_3 on DT nickel, and Y_2O_3 on DT-nickel (all supplied by American Superconductor Corp.). These data were obtained on a focused bending-magnet beamline at the

APS/Basic Energy Sciences Synchrotron Research Center by using 12 keV (1 Å) X-rays. The results in Fig. 50a can be interpreted as follows. The oscillation in the reflectivity curve for the bare DT nickel surface reveals that it is covered with an ≈5-nm-thick film (presumably NiO). The sharp drop-off in reflectivity for the Gd_2O_3- and Y_2O_3-buffered samples indicates a significant increase in the surface roughness when compared with that of the bare DT nickel, more so for the Gd_2O_3 than for the Y_2O_3.

The thickness values for the Gd_2O_3 and Y_2O_3 layers are too large (>100 nm) to determine from the data in Fig. 50a. The powder scans of the [004] reflections for Gd_2O_3 and Y_2O_3 in Fig. 50b provide evidence that the buffer layers are well ordered, with domain sizes in the c-direction of 22 and 25 nm, respectively. The results in Fig. 50 highlight the utility of a powerful X-ray source for this kind of measurement. Such results could not be obtained with a conventional laboratory X-ray source.

The [222] reflection azimuthal scans in Fig. 51a show the existence of 45° in-plane-turned domains for the Gd_2O_3/Ni specimen (representing <10% of the Gd_2O_3 grains present) but no evidence of such domains for the Y_2O_3/Ni

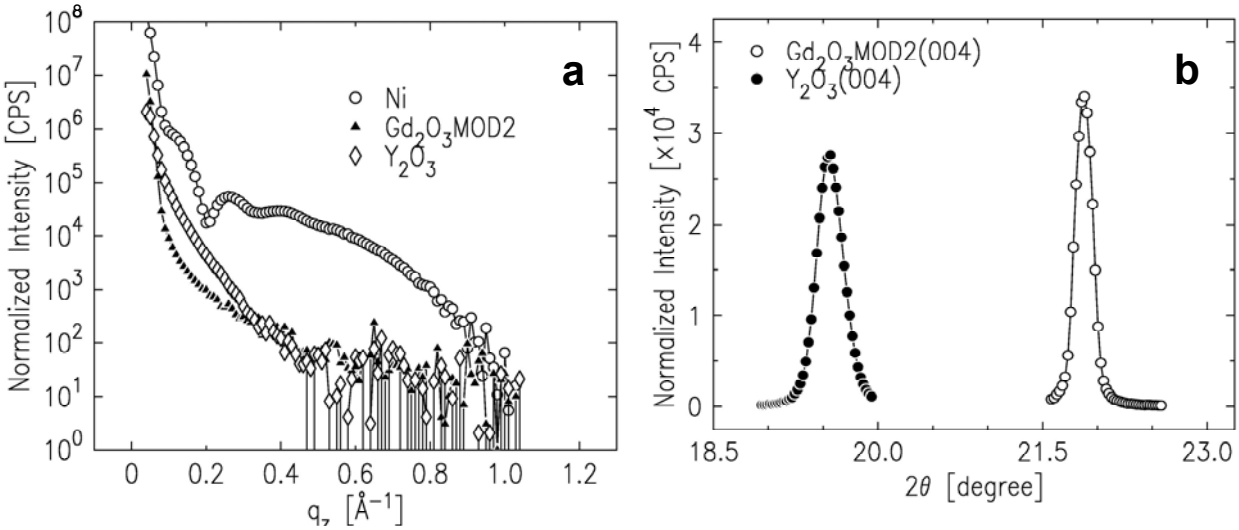

Fig. 50. (a) X-ray reflectivity scans for bare deformation-textured nickel foil specimen, Gd_2O_3-on-DT-nickel specimen, and Y_2O_3-on-DT-nickel specimen; (b) powder scans of the [004] reflections for Gd_2O_3 and Y_2O_3 films on DT nickel substrates.

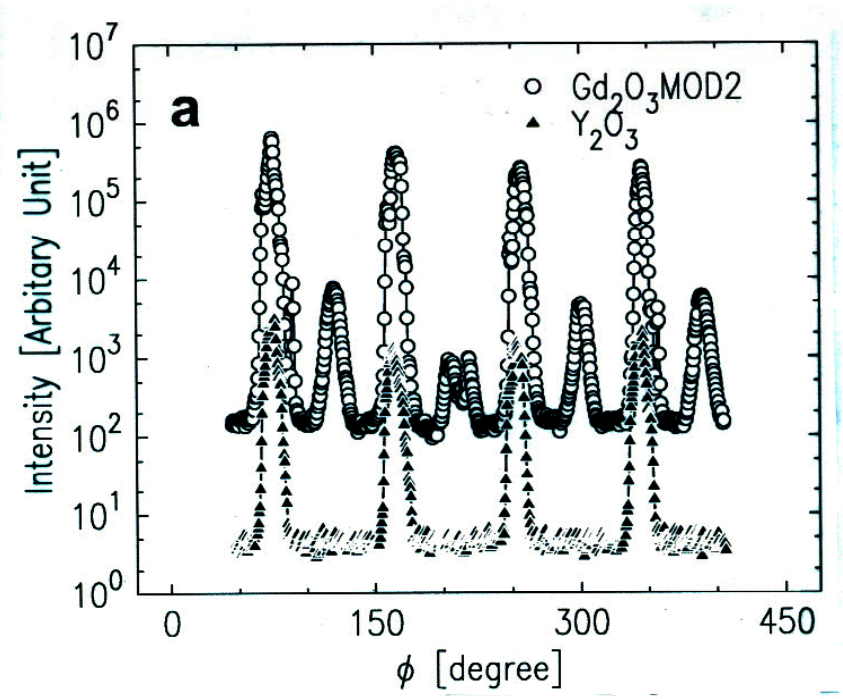

Fig. 51. (a) Azimuthal scans of [222] reflection of Gd_2O_3 and Y_2O_3 buffer layers on DT nickel substrates; and (b) rocking curves for bare DT nickel [002], Gd_2O_3 [004], and Y_2O_3 [004] reflections.

specimen. The rocking curves in Fig. 51b provide information about the quality of the mosaic distributions. In particular, the spikes in the curve for the bare DT nickel specimen indicate that the Ni [001] domains consist mostly of large grains, whereas the curves for the Gd_2O_3/Ni/Ni and Y_2O_3/Ni specimens give evidence of a smoother but not necessarily narrower mosaic distribution. Seemingly, the buffer layers exist as ordered arrays of small grains on large nickel [001] grains that act like pallets.

2.1.6 Residual Stress Analysis

Residual strains, and hence residual stresses, develop during the processing of coated conductors as a result of differences in thermal expansion for the various layers. These stresses may cause microcracking in the superconductor layer, which may degrade its superconducting properties and reduce its service life. Therefore, it is critical to evaluate residual stresses in coated conductors and improve our understanding of the relationship between residual stresses and various processing parameters. To better understand the development of residual stresses in coated conductors, X-ray diffraction techniques are being used to measure residual stresses in the ceramic buffer and superconductor layers of simple coated conductor systems. To this point, we have examined both ceramic (LAO) and metal (HC) substrates that were coated with YBCO superconductor or a YSZ buffer layer.

Using X-ray diffraction data, we calculated residual strain from the measured lattice spacing d for a particular (hkl) refection for the coating. The lattice strain (ε) associated with the (hkl) plane is given by $\varepsilon = (d - d_o)/d_o$, where d_o is the unstrained (hkl) spacing obtained from the strain-free powder. Subsequently, stress analysis was performed, and the measured strains in different directions were used to evaluate the residual stresses associated with specific planes. The measured stresses were compared with calculated values of thermal mismatch stresses, and the comparison shed light on the nature of stress evolution in these coatings.

We initially evaluated the effects of processing technique on the development of residual stresses in YSZ films that were deposited on HC by IBAD. Textured YSZ was grown at an ion-beam bombardment angle of ≈55°, while untextured YSZ of the same thickness was grown at an angle of ≈67°. Using the (200) reflection for the films, we measured compressive residual stresses of ≈375 MPa and ≈600 MPa for the textured and untextured films, respectively. Both measured stresses are much larger than the calculated thermal mismatch stress (≈125 MPa). This large difference between the measured stresses for the films and the calculated thermal mismatch stress is believed to result from

Ar-ion-peening effects during IBAD processing. Impingement of the Ar ions produced compressive stresses in both films, but channeling effects reduced ion-peening in the textured film made at ≈55°. By comparison, the ion-peening effect was larger during formation of the untextured film because there was no channeling. This effect leads to a larger induced internal stress and thus a higher measured residual stress in the untextured film.

In contrast to the YSZ films on HC, a YBCO film deposited on LAO by the TFA process showed good agreement between the measured residual tensile stress (450 ± 80 MPa) and the calculated value (525 MPa) of thermal mismatch stress. In this case, because there were no ion-peening effects, no internal stresses were induced, and hence, good agreement between the measured and calculated values of the residual stress was observed.

To confirm the validity of the X-ray diffraction technique [8], we used curvature measurements to estimate the residual stress in a YBCO film on an LAO substrate. To make the curvature measurement, flat LAO substrates (150 μm thick) were first polished on both sides. The initial curvature of the polished substrates was measured by optical interferometry; several measurements were made to improve the statistical reliability. The polished substrates were then coated with YBCO (0.3 μm thick) by PLD, and the curvature of the coated surfaces was measured by optical interferometry. The difference in curvature before and after coating with YBCO gives the curvature of the coating due to residual stress. Using this curvature of the coating, we calculated the residual stress (σ) by modification of Stoney's equation [9].

The average value of residual stress measured on five specimens was 210 ± 72 MPa. This compares very well with the stress value of 178 ± 53 MPa that was measured by X-ray diffraction and reported previously [10]. The good agreement between the results confirms the validity of these two independent measurement techniques. Further studies using optical interferometry are in progress to evaluate the residual stresses in coated conductors with different architectures.

2.1.7 Oxidation of Hastelloy C276 (HC)

Depending on which thin-film technique is used to deposit the requisite buffer and superconductor layers, the alloy can be exposed in a variety of atmospheres to temperatures as high as nearly 800°C. We have studied the oxidation kinetics of HC and the nature of the resulting oxide layer.

HC foil (≈0.4 mm thick) was obtained from Goodfellow (Berwyn, PA). Specimens (1–1.5 cm^2) were sheared from the strip and then oxidized at 300–800°C in a flowing atmosphere, in which the oxygen partial pressure (pO_2)

ranged from 0.01% to 100% O_2/balance Ar. Weight gain was monitored by thermogravimetric analysis (TGA). X-ray diffraction and SEM were conducted for each oxidized specimen. For most specimens, a diamond-stylus profilometer was used to measure surface roughness.

X-ray diffraction and SEM observations revealed only the presence of Cr_2O_3 in our scales. Most coupons were oxidized in the as-rolled condition, which was initially believed to most closely match the condition of the exposed surface of our coated conductors during one-sided deposition of buffers and superconductor. The average surface roughness of an as-rolled surface was ≈110 nm, and some surface scale was present initially. The polished surfaces, on which the buffer layers and YBCO are deposited, exhibited an average roughness of ≈2 nm, which appeared to represent the effective limit of the measurement sensitivity of the profilometer.

Typical TGA data of weight gain vs. time are shown in Fig. 52. The kinetics of most traces were approximately parabolic. We therefore plotted weight gain (ΔW) per area (A) vs. time (t). Linear fits yielded values of the parabolic rate constant (K_p) in units of $mg^2/cm^4 \cdot s$. The K_p values vs. temperature (T) were then plotted for measurements at various pO_2 values (Fig. 53). Two trends in the K_p data are clear. K_p is not a consistent function of pO_2; and no single rate constant could be ascribed to the data.

The TGA data can be converted to thickness of oxide layer if one assumes that the scale is Cr_2O_3 with a density of 5.225 g/cm^3. At all temperatures, the ΔW data exhibited scatter with respect to pO_2. For a deposition time of 2 h, scales ≈20–70 nm thick would be expected at 700°C (Fig. 54). This thickness is commensurate with that of most of the buffer layers in our coated conductors.

The question remains as to whether scales grown intentionally on HC can be sufficiently smooth and uniform to allow for subsequent buffer deposition, and whether these scales can provide any benefits in terms of, for example, impeding diffusion of cations from the substrate to the YBCO conductor. Work is in progress to address these questions. Anneals at 300–800°C have yielded important information on the surface finish of the resulting scales. Within the accuracy of the profilometry measurements, annealing at 500°C appears to produce a scale that is as smooth as the underlying metal (Fig. 55). The scales grown at temperatures ≥600°C clearly became rougher as temperature increased. The scales grown at temperatures ≤400°C appeared to become slightly rougher with decreasing temperature.

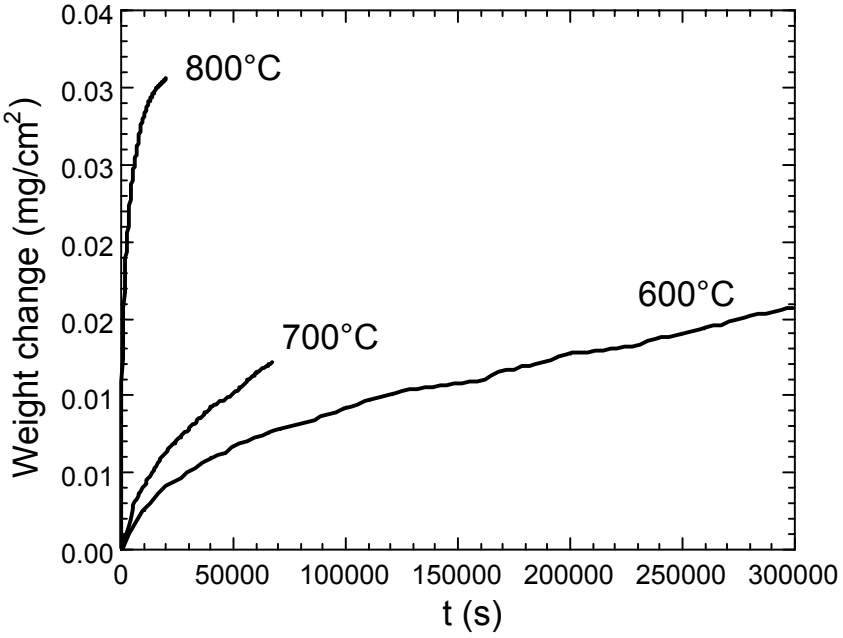

Fig. 52. Representative data for weight gain vs. time for oxidation of Hastelloy C276 in 0.01% O_2 at 600-800°C.

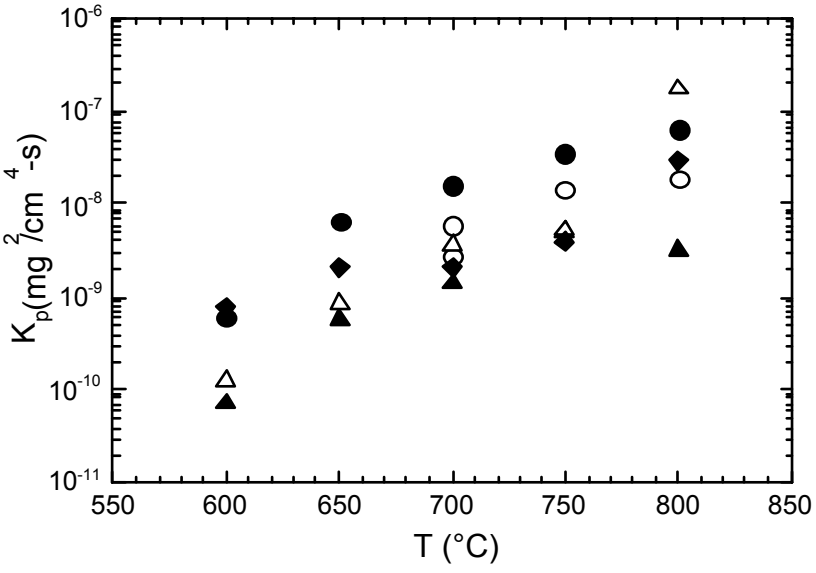

Fig. 53. Summary of parabolic rate constant vs. temperature for oxidation of Hastelloy C276 in various atmospheres: 0.01% O_2 (filled diamonds), 0.1% O_2 (open triangles), 1% O_2 (filled triangles), 10% O_2 (open circles), and 100% O_2 (filled circles).

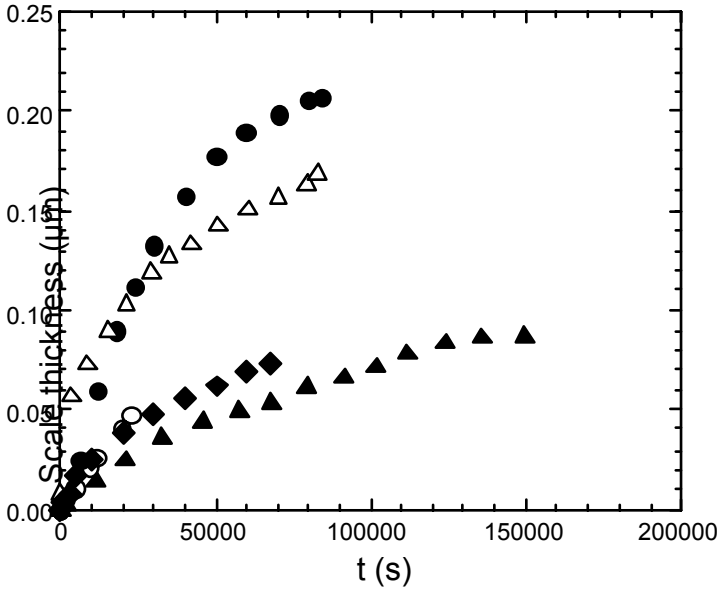

Fig. 54. Scale thickness vs. time for oxidation of Hastelloy C276 at 700°C in 0.01% O_2 (filled diamonds), 0.1% O_2 (open triangles), 1% O_2 (filled triangles), 10% O_2 (open circles), and 100% O_2 (filled circles).

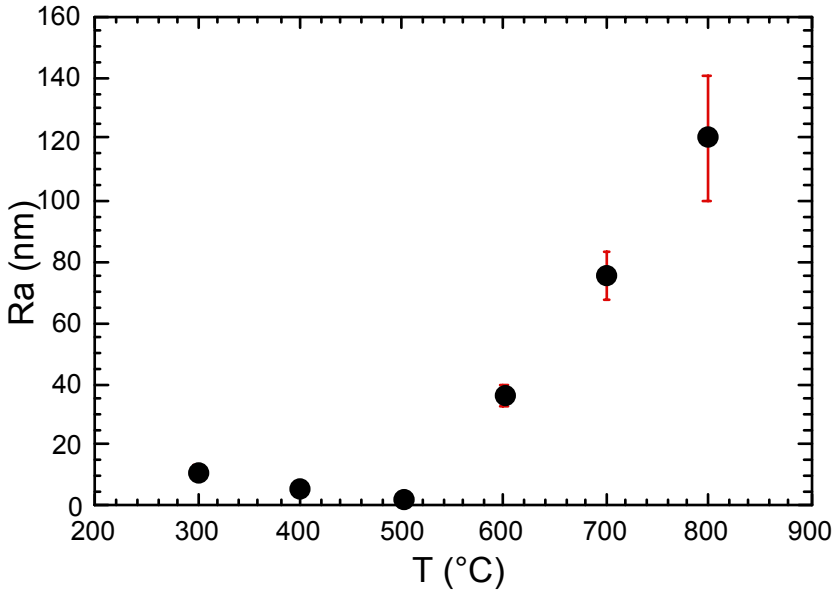

Fig. 55. Average surface roughness of scale on polished Hastelloy C276 vs. temperature for scales grown for 10 h in 100% O_2. Error bars are standard deviations.

Current work on oxidized HC is divided into kinetics studies of polished substrates, more-detailed characterization of the resulting films, and use of oxidized substrates in fabricating coated conductors.

2.2 Bi-Pb-Sr-Ca-Cu-O Conductors

We have reported previously [11,12] on dispersion hardening of Ag-Mg alloy sheaths through internal oxidation of reactive solute species. This treatment can substantially improve strength and strain tolerance of $Bi_2Sr_2CaCu_2O_X$ (Bi–2212) and $(Bi,Pb)_2Sr_2Ca_2Cu_3O_X$ (Bi–2223) conductors. This hardening may also allow for use of Ag-Mg alloys in coated-conductor applications. Hardening through formation of Mg-O clusters and MgO precipitates has been confirmed, and hardness increases have been documented. However, the tensile properties of hardened AgMg alloys are more relevant than hardness to wire applications. For this reason, studies were done in which the heat treatment has been correlated to the tensile strength, ductility, and microstructure.

TGA data from the Ag/1.12 at.% Mg alloy have been presented [13] previously and published. In brief, as expected, the times to reach oxygen saturation increased with decreasing temperature. Furthermore, the oxygen saturation levels were higher at lower temperature, and the saturation reached a maximum and then decreased with increasing time at a given temperature. The TGA data provided evidence of an internal oxidation process that involved clustering of O and Mg species.

The presence of the inferred clusters was confirmed by TEM (Fig. 56). Uniform distributions of clusters were observed. In the sample treated at 450°C, for example, the clusters were smaller (≈30 Å) and more densely distributed than in the sample treated at 825°C (cluster size ≈50 Å). The observed cluster size agreed well with those predicted from the Mg/O ratios.

The tensile data provided some surprises. A representative plot of load-displacement data is shown in Fig. 57. Note that the slope is not the elastic modulus because the load-train compliance was low. Exceptions to the typical brittle behavior occurred in the coupons that were saturated with O at 500°C and subsequently annealed at 825°C. Although these coupons exhibited brittle fracture after the first heat treatment, the second treatment resulted in extensive ductility (Fig. 57b). These specimens were the only ones to exhibit ductility. Average fracture stresses are shown in Fig. 58.

Fig. 56. Plan-view TEM images of coupons subjected to heat treatment at (a) 450 and (b) 825°C.

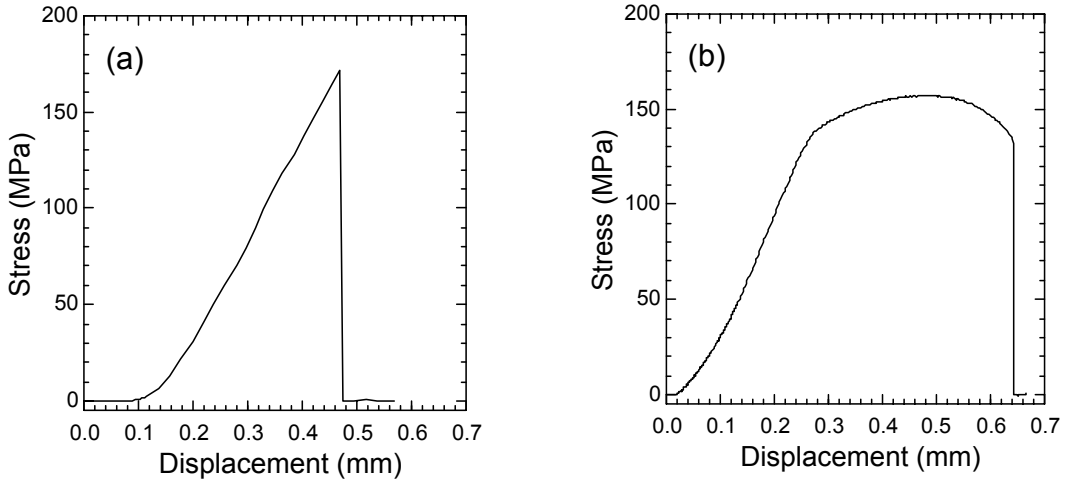

Fig. 57. Representative tensile-test data: (a) specimen saturated with O at 600°C and (b) specimen saturated with O at 500°C, then heated for 50 h at 825°C.

The cause for the anomalous behavior at 500°C is not yet clear. In a kinetic analysis presented previously [12], we discussed a discontinuity in the parabolic rate constant for internal oxidation at temperatures below 600°C and an oxygen pressure of ≈8% O_2. Both this discontinuity and the anomalous mechanical data could be due to a change in oxidation behavior, such as a superstoichiometric

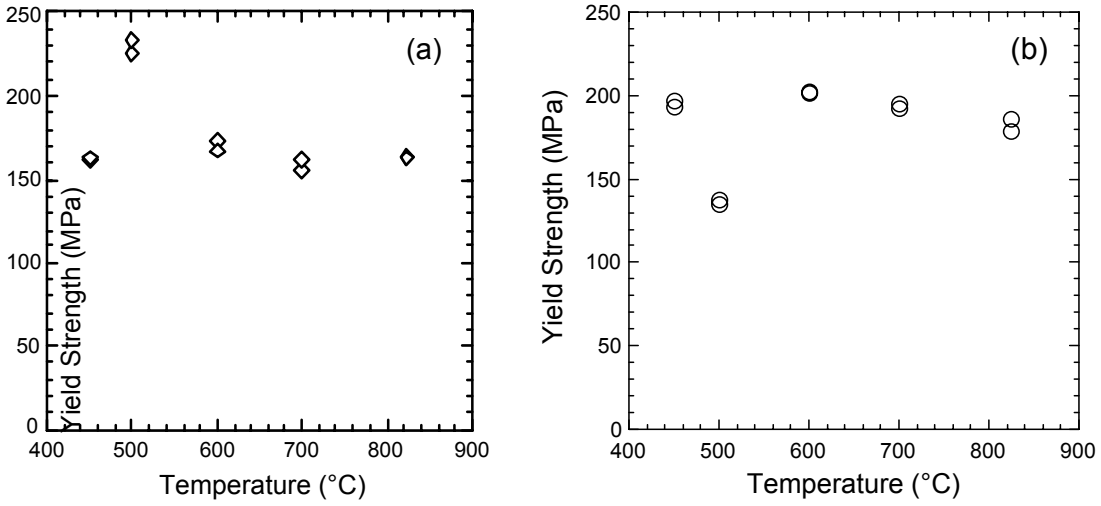

Fig. 58. Summary of tensile strengths: (a) specimens saturated with O and (b) specimens saturated with O at temperature shown, then heated for 50 h at 825°C.

oxidation reaction of Mg or oxidation of an Ag-Mg-O intermediate phase that is stable only at 8% O_2 and below 600°C. Alternatively, diffusion could possibly occur faster along dislocations in cold-worked Ag-Mg alloys internally oxidized at low temperatures.

2.3 Applications and Devices

A potential application of high-T_c superconductors for the electric power industry is the fault current limiter (FCL). A leading candidate for FCLs is the so-called superconductor-shielded core reactor (SSCR), a passive device that consists mainly of a closed iron core inside a superconductor tube and a copper coil wound on the outside of the superconductor tube [14-18]. The SSCR uses the shielding capability of a superconductor tube to keep the inductance low under normal operating conditions. Under fault conditions, the high current in the copper coil exceeds the shielding capability of the superconductor tube, and a jump in impedance occurs because the iron core is no longer shielded from the coil by the superconductor tube.

Originally, the SSCR was thought to be an inductive device because the coupling between the superconductor and the primary circuit is magnetic. For some time, however, it has been realized from test results that a closed-core SSCR is a resistive device [19]. The superconductor tube heats significantly during a fault, and its recovery is usually much longer than that of an inductive

device because heat must be removed from the superconductor after the fault is cleared. An equivalent circuit of an ideal transformer, based on the lumped parameter, can be used to explain the resistive behavior of the SSCR quite well [19]; however, the magnetic and thermal behavior of a superconductor tube during a fault is not well understood. To improve our understanding of this behavior, we experimentally studied the transient response of a superconductor tube to a pulsed magnetic field [20-21]. In this study, magnetic diffusion [20,22] is used to qualitatively explain the important experimental observations on the transient response of a superconductor tube to a pulsed magnetic field.

The experimental measurements were obtained with a test section made of a copper coil wound on a cylindrical superconductor tube, as shown in Fig. 59. The copper coil had 1200 turns and was made of 0.71-mm-diameter copper wire. The material of the superconductor tube was bulk $Bi_2Sr_2CaCu_2O_x$ (BSCCO) made by a melt-cast process. The BSCCO tube was 74.8 mm long, with a wall thickness of 5.5 mm and an outside diameter of 25.6 mm. A Hall probe was placed near the center of the tube to measure the magnetic field in the hole of the tube. A Rogowski coil was employed to measure the induced current in the superconductor tube. The copper coil was connected to a pulsed current source.

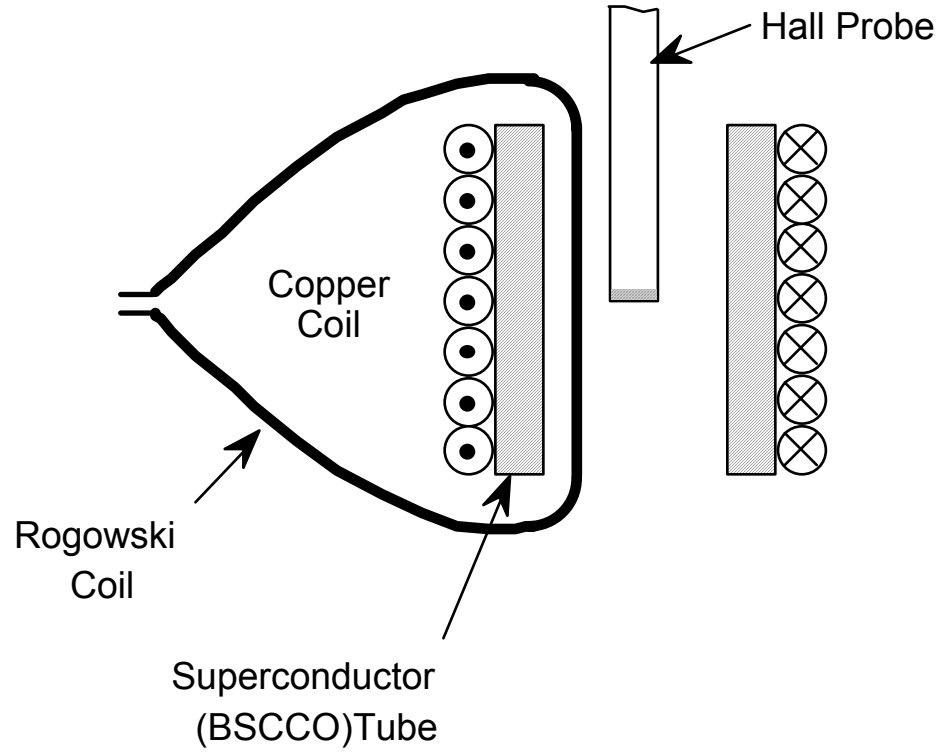

Fig. 59. Schematic diagram of apparatus used to measure the transient response of a melt-cast BSCCO tube to a pulsed magnetic field.

A more detailed description of the experimental apparatus and the experimental procedure can be found in Ref. 20. Figure 60 shows the typical response of the melt-cast-processed BSCCO superconductor tube subjected to a pulsed magnetic field.

The most important feature of Fig. 60 is the time delay between the peak excitation current NI and the peak penetrated field H at the center of the tube. As shown in Fig. 60, during the period from 22 to 32 ms, the magnetic field H is still increasing while the excitation current NI has already reached its peak and begun to decrease. A second important feature of the experiment is that, as the peak excitation current NI_{max} is increased, the time delay between peak NI and peak H decreases. Another important feature of the experiment is that the penetration field H* (Fig. 7 of Ref. 20) increases with peak NI. As we shall see, all three salient features of the experimental results can be explained qualitatively by the linear magnetic-diffusion model.

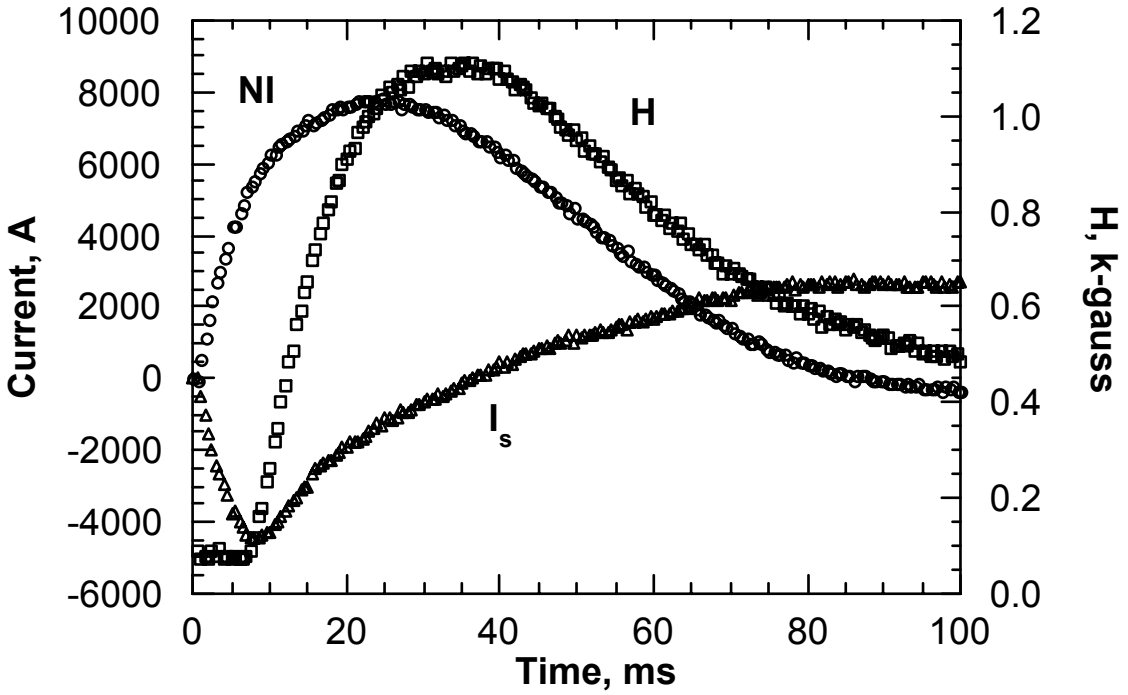

Fig. 60. Transient response of melt-cast BSCCO superconductor tube to pulsed magnetic field. N is the number of turns of the copper coil; NI, the excitation current in the copper coil; H, the magnetic field in the hole of the tube measured by a Hall probe; and I_S, the induced current in the superconductor tube, deduced from the signal of the Rogowski coil. (Adopted from Ref. 20.)

The geometry of the analytical model adopted here is a slab with thickness 2*a* in the x direction, subjected to a sinusoidal applied field in the z direction, as shown in Fig. 61. The governing equation is

$$D_m (\partial^2 B/\partial x^2) = \partial B/\partial t \,, \tag{5}$$

where B is the magnetic flux density in the z direction, and t is time. The magnetic diffusion coefficient D_m is given by

$$D_m = \rho/\mu_o \,, \tag{6}$$

where ρ is the resistivity, and μ_o is the permeability of free space.

Relevant parameters of the model include the characteristic length δ, also known as the skin depth, and the characteristic time τ. These are given by

$$\delta = (2D_m/\omega)^{1/2} \tag{7}$$

and

$$\tau = a^2/D_m \,, \tag{8}$$

where ω is the driving frequency for the applied field. A more detailed description of the model may be found in Ref. 23. The characteristic length δ is small only if the frequency ω is very large or if the resistivity is very small. In general, δ can be large or small compared with the characteristic dimension *a* of the superconductor.

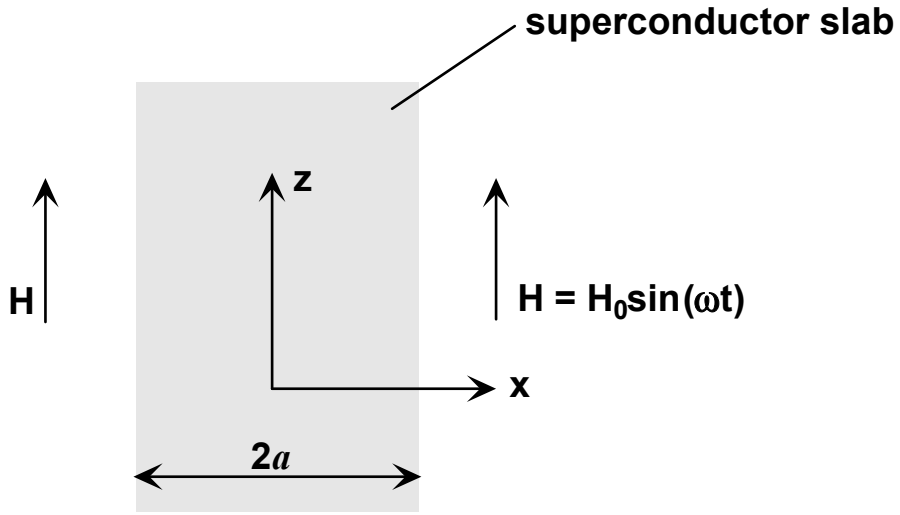

Fig. 61. Superconductor slab of thickness 2a subjected to sinusoidal applied field in z direction (slab extends to infinity in both the y and the z directions).

Based on the linear magnetic diffusion model, the time evolution of magnetic flux density was calculated at various locations in the superconductor along the x direction, as shown in Fig. 62 for $a/\delta = 2$. The horizontal axis is the time normalized by the period T_o. For a 60-Hz AC system, the period is $T_o = 16.67$ ms. Briefly, the solution contains a transient term, whose decay rate depends on τ, and a quasi-steady-state term. It was found that the transient dies out quickly and quasi-steady state is reached within three cycles, even for the innermost location of $x/a = 0$. Furthermore, the transient term modifies the quasi-steady-state solution only slightly; therefore, we shall use the quasi-steady state solution alone to explain the experimental results.

Figure 63 shows the amplitude A of the quasi-steady-state solution as a function of position for various values of a/δ. It can be seen that the magnetic flux density is fairly uniform in the slab when $a/\delta < 0.5$. Very little current is induced in the slab because Ampere's law states that

$$\partial B/\partial x = -\mu_o J \, . \tag{9}$$

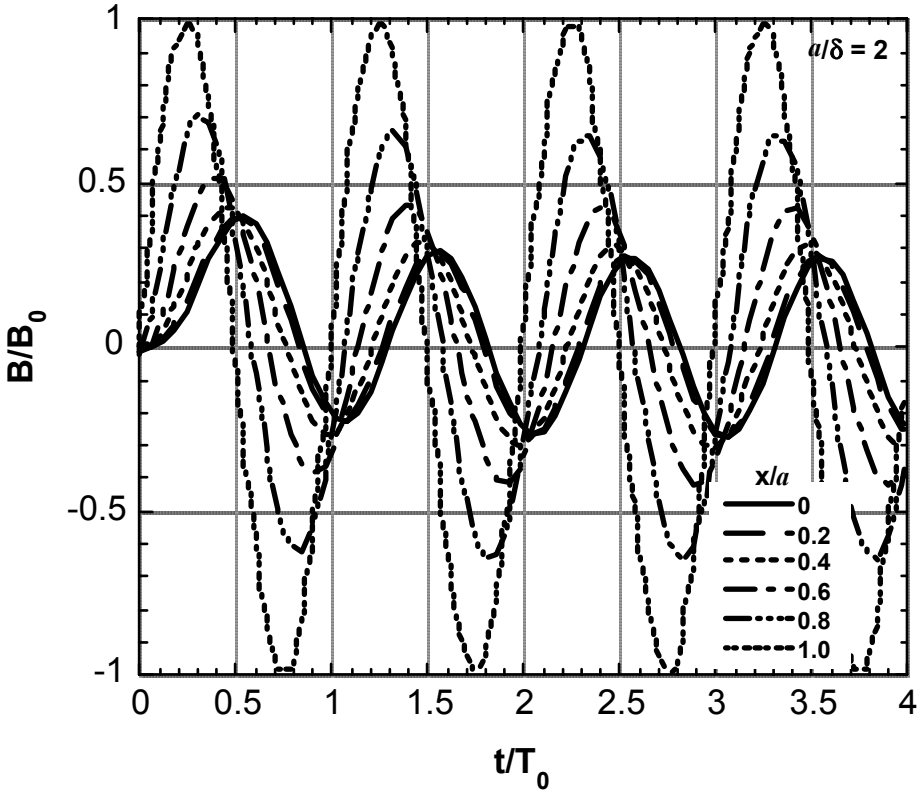

Fig. 62. Wave forms of magnetic flux density at various values of x/a in superconductor slab when $a/\delta = 2$.

This equation implies that resistance, rather than inductance, determines the field distribution [24]. At the other extreme, the magnetic flux density is limited to a relatively thin layer near the surface when a/δ>100. Very large current is induced near the surface to cancel the applied field inside the bulk of the slab. In this case, the macroscopic inductance, rather than the resistance, is the dominant factor. Figure 63 shows that under AC steady-state conditions, the center of the slab is just penetrated by the applied field when $a/\delta \cong 7.5$. For $a/\delta > 7.5$, the magnetic flux density at $x/a = 0$ is always zero.

In applying the linear magnetic diffusion model [23] to the transient response of the melt-cast BSCCO tube, one must remember that the explanation is qualitative because the current pulse is not exactly sinusoidal, the tube is cylindrical (not a slab), and the effects of nonlinear magnetic diffusion and heating are ignored. The half-thickness a of the slab can be considered equivalent to the wall thickness of the BSCCO tube. Therefore, $x/a = 1$ corresponds to the outside radius, and $x/a = 0$ corresponds to the inside radius of the BSCCO tube. The key parameter in the linear model is the dimensionless length a/δ, which depends on the magnetic diffusion coefficient D_m according to

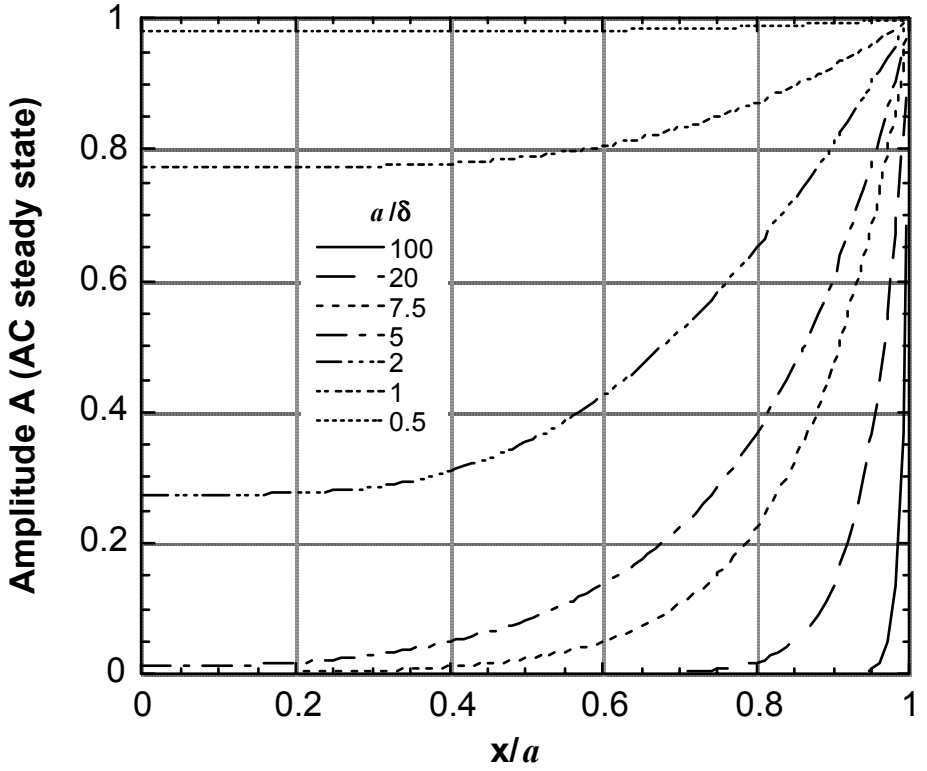

Fig. 63. Variation of amplitude A (of AC steady-state solution) with x/a for various values of a/δ.

Eqn. 7. When a/δ is much larger than 1, the superconductor behaves mostly like an inductor. This condition corresponds to a superconductor with a relatively low average resistivity, and only a relatively small amount of heat is generated near the outer radius of the superconductor tube. When a/δ <<1, the superconductor behaves like a resistor; the entire wall thickness of the superconductor tube becomes resistive, and the average resistivity of the superconductor is high.

Figures 64-66 show the calculated wave forms of the magnetic flux density B at various locations when a/δ equals 0.5, 2.0, and 10, respectively. For the resistance-dominated case (a/δ = 0.5), Fig. 64 shows that the magnitude of B/B_o is almost the same everywhere in the superconductor because the field is fairly uniform. However, there is clearly a phase lag between peak B inside the superconductor and that at the outer surface (x/a = 1). As a/δ is increased to 2, Fig. 65 shows that the peak field decreases with decreasing x/a, and the phase lag between peak B inside and that at the outer surface (x/a = 1) is greater than that shown in Fig. 64. As a/δ is increased to 10, the time delay between the applied field and the field inside becomes even larger (Fig. 66).

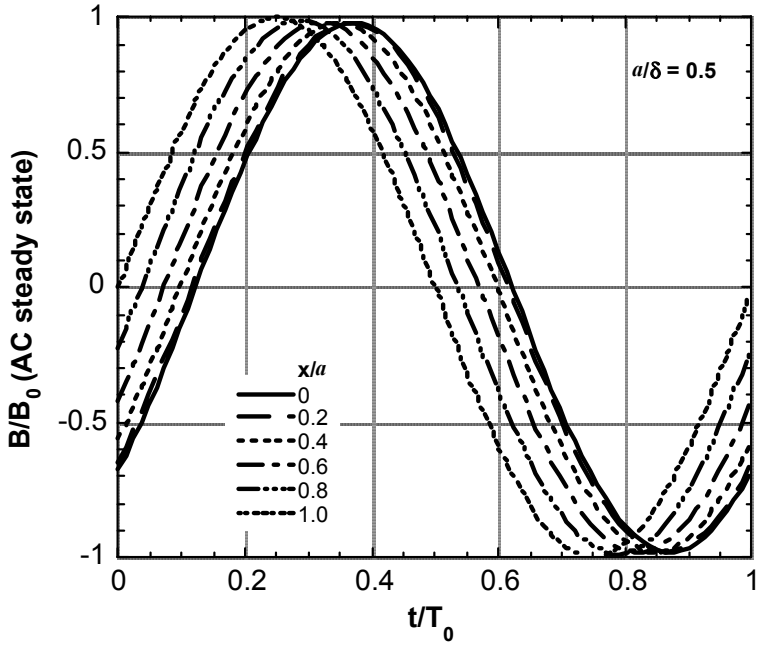

Fig. 64. AC steady-state wave form of magnetic flux density at various values of x/a when a/δ = 0.5.

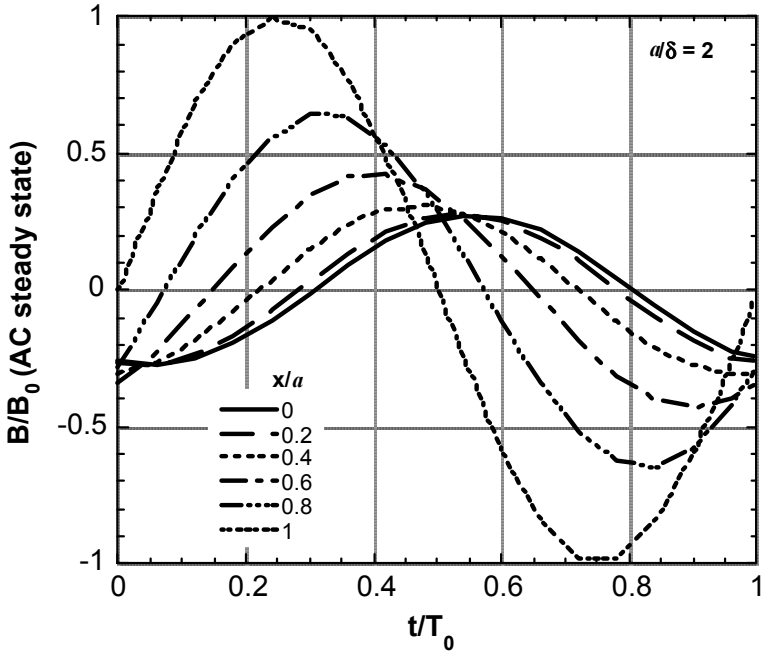

Fig. 65. AC steady-state wave form of magnetic flux density at various values of x/a when $a/\delta = 2.0$.

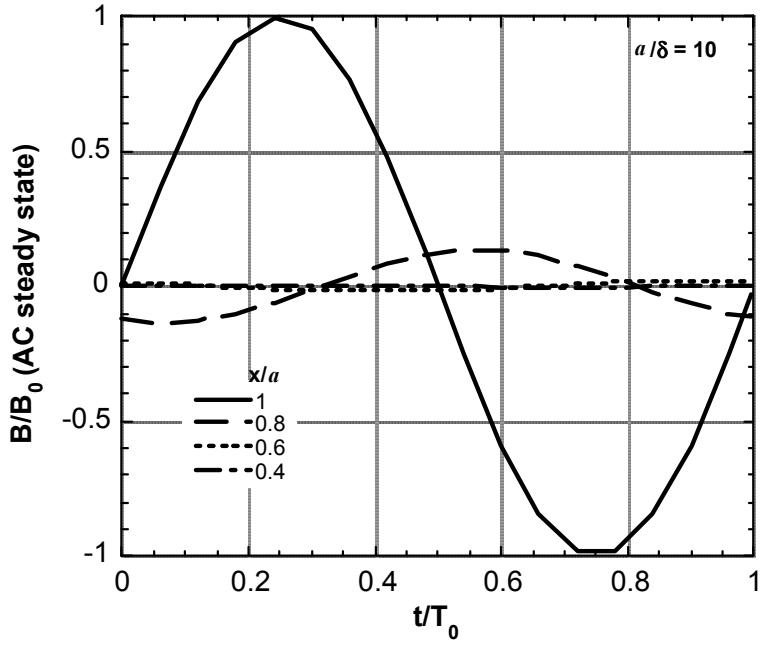

Fig. 66. AC steady-state wave form of magnetic flux density at various values of x/a when $a/\delta = 10$.

Figure 67 shows the calculated time delay (Δt) of the peak B inside the superconductor and that at the outer surface ($x/a = 1$) at various locations in the superconductor for three values of a/δ. Clearly, the time delay increases with a/δ. In other words, as the superconductor becomes more resistive, the time delay decreases. Thus, the linear magnetic diffusion model demonstrates a time delay between the applied field at the outer surface ($x/a = 1$) and the penetrated field at the inner surface ($x/a = 0$), and this time delay decreases as the resistivity of the superconductor increases. These results agree quite well with the experimental observations described previously. Figures 64-66 also clearly show that after the applied field B/B_o (at $x/a = 0$) begins to decrease after reaching its peak, the field inside the tube at $x/a = 0$ is still rising. This finding is again in agreement with the experimental observation described previously. A third experimental observation is that the penetration field increases with the current ramp rate. For a sinusoidal applied field, the ramp rate can be considered proportional to the angular frequency ω. It is shown elsewhere [23] that the applied field penetrates the tube wall more readily when a/δ is decreased. From Eq. 7,

$$a / \delta = a (\omega / 2D_m)^{1/2}. \qquad (10)$$

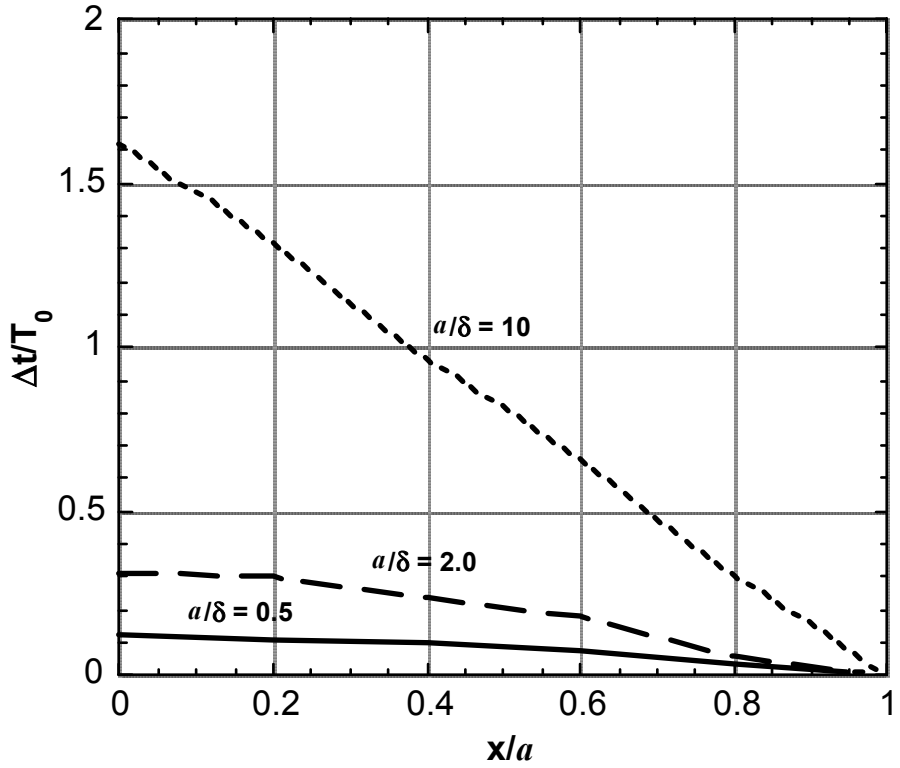

Fig. 67. Variation of time delay Δt (between peak B at x/a = 0 and that at x/a = 1) with x/a for various values of a/δ.

Thus, a/δ increases with $\omega^{1/2}$. When the ramp rate (ω) of the applied field increases, a/δ increases. This effect makes penetration of the superconductor tube by the applied magnetic field more difficult. This statement is equivalent to saying that the penetration field increases with the ramp rate of the applied field. Therefore, all three salient features of the experimental observations are explained qualitatively by the linear magnetic-diffusion model.

Having seen that a linear magnetic diffusion model explains the transient response of a superconductor tube to a pulsed magnetic field, we now consider the implications of the analytical results for fault current limiters. As described earlier, a closed-core SSCR is a resistive device under the fault condition, and its characteristics can be explained by the equivalent circuit of an ideal transformer. An equivalent circuit is a lumped-parameter model based on linear circuit elements. It does not explain what is happening inside the superconductor tube. The field equations and the properties of the superconductor, such as the flux pinning strength, govern what happens in the superconductor. As seen below, based on the results of the magnetic-diffusion model, we can explain what is happening in the superconductor tube, consistent with the lumped-parameter model of an ideal transformer.

Two experimental results that are important for the closed-core SSCR are that the device is more inductive than resistive under continuous operation at relatively low current, and it becomes resistive under fault conditions with relatively high current. At relatively low current under continuous operation, the induced current in the superconductor tube is capable of shielding the core from the external magnetic field. As a result, the applied field does not penetrate the superconductor tube and corresponds to the curves in Fig. 63 when $a/\delta > 7.5$. This indeed corresponds to the case for an inductance-, rather than resistance-, dominated device. (Ref. 24 provides an excellent account of the various limits of distributed systems). On the other hand, when the current is rapidly increasing during a fault, the superconductor tube is penetrated by the applied field, and the average resistance of the superconductor increases rapidly with time. The superconductor tube is rapidly changing from an inductance-dominated system with large a/δ (>112) to a resistance-dominated system with small $a/\delta < 0.5$. This picture is in agreement with the experimental results of a closed-core SSCR and is consistent with the lumped-parameter model of the ideal transformer [19].

These results show that a linear magnetic diffusion model can be used to explain the transient response of a superconductor tube to a pulsed magnetic field. The analytical results qualitatively explain the experimental observations that there is a time delay between the excitation current and the magnetic field in the core of the superconductor tube, the time delay decreases as the superconductor becomes more resistive, and the penetration field increases with

the ramp rate of the excitation current. Another important consequence of magnetic diffusion is that dissipation is always associated with joule heating, ρJ^2, in addition to hysteresis loss, under AC steady-state conditions. For an SSCR, the ρJ^2 loss is not only important under fault conditions, but also under continuous operation, because it affects the AC steady-state critical current of the superconductor tube. The effect of magnetic diffusion on AC losses will be described more fully in a later report.

Although the linear magnetic diffusion model qualitatively explains quite well a superconductor's transient response to a pulsed magnetic field and the important electromagnetic characteristics of a closed-core SSCR, it cannot accurately predict the time evolution of the magnetic field and current distribution in the superconductor. The model has important limitations. First, as described previously, linear magnetic diffusion cannot account for flux pinning in the superconductor (nonlinear B/H curves). Second, linear magnetic diffusion is for ohmic conductors where the resistivity is constant. For high-T_c superconductors, the resistivity is a function of current density, magnetic field, and temperature. High-T_c superconductors usually follow the so-called power law (nonlinear E/J relationship). Finally, the present treatment relates to an isothermal system, where the rate of heat generation is small, and the rate of heat transfer is adequate to keep the temperature of the superconductor constant. This situation can occur only if both the frequency and the amplitude of the applied field are small. The effects of nonlinear magnetic diffusion and heating will be discussed more completely at a later time.

References

1. O. P. Karpenko, J. C. Bilello, and S. M. Yalisove, *J. Appl. Phys.*, 82, 1397-1403 (1997).
2. A. F. Moodie and C. E. Warble, *J. Crystal Growth*, 10, 26-38 (1971).
3. R. E. Koritala, M. P. Chudzik, Z. L.uo, D. J. Miller, C. R. Kannewurf, and U. Balachandran, *IEEE Trans. On Appl. Supercond.*, 11, 3473-3476 (2001).
4. K. E. Gray, M. B. Field, and D. J. Miller, *Phys. Rev. B* **58**, 9543 [1998].
5. A. Gurevich and L. D Cooley, *Phys. Rev. B* **50**, 13563 [1994].
6. Practical Superconductor Development for Electrical Power Applications, Argonne National Laboratory Quarterly Report for period ending Dec. 31, 2000.
7. R. Wang, Y. Zhou, S. Pan, H. Zhang, X. Guo, X. Xiong, H. Lu, Z. Zhen, and G. Yang, *J. Appl. Phys.*, 84, 1994 (1998).

8. Practical Superconductor Development for Electrical Power Applications, Argonne National Laboratory Quarterly Report for period ending June 30, 2001.

9. G. Stoney, *Proc. R. Soc. London*, Ser. A 82, 172 (1909).

10. B. Ma, M. Li, Y. A. Jee, R. E. Koritala, B. L. Fisher, and U. Balachandran, in press, *Phyisca C*, 366, 27--276 (2002).

11. Practical Superconductor Development for Electrical Power Applications, Argonne National Laboratory Quarterly Report for period ending June 30, 2000.

12. Practical Superconductor Development for Electrical Power Applications, Argonne National Laboratory Quarterly Report for period ending June 30, 1999.

13. B. C. Prorok, J.-H. Park, K. C. Goretta, R. E. Koritala, U. Balachandran; and M. J. McNallan, *IEEE Trans. Applied Superconductivity*, 11, 3273-3276 (2001).

14. W. Paul, M. Lakner, J. Rhyner, P. Unternahrer, T. Baumann, M. Chen, L. Widenhorn, and A. Guerig, *Supercond. Sci. Technol.*, 10, 914-918 (1997).

15. J. Cave, D. Willen, R. Nadi, and Y. Brissette, *IEEE Trans. Appl. Supercond.*, 9, 1335-1338 (1999).

16. V. Meerovich, V. Sokolovsky, J. Bock, S. Gauss, S. Goren, and G. Jung, *IEEE Trans. Appl. Supercond.*, 9, 4666-4676 (1999).

17. J. Nakatsugawa, S. Noguchi, A. Ishiyama, H. Kado, and M. Ichikawa, *IEEE Trans. Appl. Supercond.*, 9, 1373-1376 (1999).

18. Y. S. Cha, Z. J. Kang, D. J. Evans, and J. R. Hull, *Appl. Supercond.*, 4, 173-184 (1996).

19. M. G. Ennis, T. J. Tobin, Y. S. Cha, and J. R. Hull, *IEEE Trans. Appl. Supercond.*, 11, 2050-2053 (2001).

20. Y. S. Cha and T. R. Askew, *Physica C*, 302, 57-66 (1998).

21. Y. S. Cha, D. J. Evans, and J. R. Hull, *IEEE Trans. Appl. Supercond.*, 9, 1320-1323 (1999).

22. Y. S. Cha, *Physica C*, 330, 1-8 (2000).

23. Y. S. Cha, *Physica C*, 361, 1-12 (2001).

24. T. P. Orlando and K. A. Delin, "Foundations of Applied Superconductivity," Chap. 2, Addison-Wesley, Reading, Massachusetts, 1991.

Patents: 1999-2001

Method of manufacturing a high temperature superconductor with improved transport properties
Uthamalingam Balachandran, Richard Siegel, and Thomas Askew
U.S. Patent No. 6,191,075 (February 20, 2001).

Method and apparatus for measuring gravitational acceleration utilizing a high temperature superconducting bearing
John R. Hull
U.S. Patent 6,079,267 (June 27, 2000).

Engineered flux pinning centers in BSCCO, TBCCO and Y-123 superconductors
Kenneth C. Goretta, Michael T. Lanagan, Jieguang Hu, Dean J. Miller, Suvankar Sengupta, John C. Parker, U. Balachandran, Donglu Shi, and Richard W. Siegel
U.S. Patent 5,929,001 (July 27, 1999).

Passive fault current limiting device
Daniel J. Evans and Yung S. Cha
U.S. Patent 5,892,644 (April 6, 1999).

Automatic HTS force measurement instrument
Scott T. Sanders and Ralph C. Niemann
U.S. Patent 5,889,397 (March 30, 1999).

Method and etchant to join Ag-clad BSCCO superconducting tape
Uthamalingam Balachandran, A. N. Iyer, and J. Y. Huang
U.S. Patent 5,882,536 (March 16, 1999).

Elongated Bi-based superconductors made by freeze dried conducting powders
Uthamalingam Balachandran, Milan Lelovic, and Nicholas G. Eror
U.S. Patent 5,874,384 (Feb. 23, 1999).

Thin-film seeds for melt processing textured superconductors for practical applications
Boyd W. Veal, Arvydas Paulikas, Uthamalingam Balachandran, and Wei Zhong
U.S. Patent 5,869,431 (Feb. 9, 1999).

Superconductor composite
Stephen E. Dorris, Dominick A. Burlone, and Carol W. Morgan
U.S. Patent 5,866,515 (Feb. 2, 1999).

Surface texturing of superconductors by controlled oxygen pressure
Nan Chen, Kenneth C. Goretta, and Stephen E. Dorris
U.S. Patent 5,856,277 (Jan. 5, 1999).

Publications: FY 2001

T. R. Askew (Kalamazoo College) and Y. S. Cha, Transient Response of 50-KiloAmp YBCO Rings and Ring Pairs to Pulsed Magnetic Fields, IEEE Trans. on Applied Superconductivity, Vol. 11, No. 1, March 2001, pp. 3947-3950.

P. Berghuis, D. J. Miller, D. H. Kim, K. E. Gray, R. Feenstra (ORNL), and D. K. Christen, Grain Boundary Transport Properties in YBa_2Cu_3Ox Coated Conductors, IEEE Tran. on Applied Superconductivity, Vol. 11, No. 1 (Pt. 3), March 2001, pp. 3868-3871.

Y. S. Cha and T. R. Askew (Kalamazoo College), Transient Characteristics of a High-T_c Superconductor Tube Subjected to Internal and External Magnetic Fields, IEEE Trans. on Applied Superconductivity, Vol. 11, No. 1, March 2001, pp. 2485-2488.

Y. S. Cha, Magnetic Diffusion and Dissipation in High-T_c Superconductors Subjected to Sinusoidal Applied Fields, Physica C, Vol. 361, pp. 1-12 (2001).

M. P. Chudzik, R. Koritala, Z. P. Luo, D. J. Miller, U. Balachandran; and C. R. Kannewurf (Northwestern U.), Mechanism and Processing Dependence of Biaxial Texture Development in Magnesium Oxide Thin Films Grown by Inclined-Substrate Deposition, IEEE Trans. on Applied Superconductivity, Vol. 11, No. 1, March 2001, pp. 3469-3472.

H. Claus, U. Welp, H. Zheng, L.Chen, A. P. Paulikas, B. W. Veal, K. E. Gray, and G. W. Crabtree, Critical Current Across Grain Boundaries in Melt-Textured $YBa_2Cu_3O_{7-\delta}$ Rings, Phys. Rev. B 64, 144507 (2002).

A. Deptula, W. Lada, T. Olczak (Inst. of Nuclear Chemistry, Warsaw, Poland); J. E. Ostenson (Ames Laboratory); T. A. Cruse and K. C. Goretta, Synthesis of $NdBa_2Cu_3O_x$ Powder by a Sol-Gel Technique, J. Mater. Sci. Lett. 20 (2001) 59-61.

M. G. Ennis, T. J. Tobin (S&C Electric Co.); J. R. Hull, and Y. S. Cha, Fault Current Limiter - Predominantly Resistive Behavior of a BSCCO Shielded-Core Reactor, IEEE Trans. on Applied Superconductivity, Vol. 11, No. 1, March 2001, pp. 2050-2053.

K. E. Gray, H. Claus, L. Chen, B. W. Veal, A. P. Paulikas, D. J. Miller, U. Welp, and R. Feenstra, Role of Grain Boundary Dissipation and a New Measurement Technique, Proc. 2001 Intl. Workshop on Superconductivity – 5th Joint ISTEC/MRS Workshop, "HTS Conductors, Processing, and Applications," pp. 255-256 (2001).

T. G. Holesinger, A. Ayala, R. M. Baurceanu, and V. A. Maroni, Investigation of the Initial Stages of Processing Bi-2223 Multifilamentary Tapes by Analytical Electron Microscopy, IEEE Trans. on Applied Superconductivity, Vol. 11, No. 1, March 2001, pp. 2991-2994.

J. R. Hull, Energy Storage Systems, Chapter 9.5 in "Properties, Processing, and Applications of YBCO and Related Materials," eds. W. Lo and A. M. Campbell, IEE Books, Stevenage, UK (2001).

J. R. Hull, Superconducting Bearings, Chapter 9.4 in "Properties, Processing, and Applications of YBCO and Related Materials," eds. W. Lo and A. M. Campbell, IEE Books, Stevenage, UK (2001).

J. R. Hull and T. M. Mulcahy, Magnetically Levitated Space Elevator to Low Earth Orbit, Proc. 3rd Intl. Symp. on Linear Drives for Industrial Applications, Nagano, Japan, Oct. 17-19, 2001, pp. 42-47.

J. R. Hull, Superconducting Levitation, Engineering Superconductivity, pp. 563-568 (2001), P. J. Lee, Ed., John Wiley & Sons, Inc.

J. R. Hull, Magnetic Levitation, Engineering Superconductivity, pp. 22-30 (2001), P. J. Lee, Ed., John Wiley & Sons, Inc. (New York).

Y. A. Jee, M. Li, B. Ma, V. A. Maroni, B. L. Fisher, and U. Balachandran, Comparison of Texture Development and Superconducting Properties of $YBa_2Cu_3O_X$ Thin Films Prepared by TFA and PLD Processes, Physica C, Vol. 354/4, pp. 297-303 (2001).

Y. A. Jee, B. Ma, M. Li, B. L. Fisher, and U. Balachandran, Texture Formation and Superconducting Properties of $YBa_2Cu_3O_X$ Thin Films Prepared by Solution Process on $LaAlO_3$ Single Crystals, Mat. Res. Soc. Symp. Proc. Vol. 659, High-Temperature Superconductors -- Crystal Chemistry, Processing and Properties,

pp. II9.17.1-17.6 (2001), eds. U. Balachandran, H. C. Freyhardt, T. Izumi, and D. C. Larbalestier.

Y. A. Jee, B. Ma, M. Li, V. A. Maroni, B. L. Fisher, and U. Balachandran, Texture Development and Superconducting Properties of $YBa_2Cu_3O_x$ Thin Films Prepared by a Solution Process in Low Oxygen Partial Pressure, Supercond. Sci. Technol. 14 (2001) 285-291.

R. E. Koritala, M. P. Chudzik, U. Balachandran, Z. P. Luo, D. J. Miller; and C. R. Kannewurf (Northwestern U.), Transmission Electron Microscopy Investigation of Texture Development in Magnesium Oxide Buffer Layers, IEEE Trans. on Applied Superconductivity, Vol. 11, No. 1, March 2001, pp. 3473-3476.

R. E. Koritala; U. P. Trociewitz, C. Bacaltchuk, J. Schwartz (Florida State U.); P. R. Sahm (RWTH Aachen U. of Technology) and L. Brandao (Inst. Militar De Eng.), Microstructural Development and Superconducting Properties of BaO_2-added $Bi_2Sr_2CaCu_2O_{8+x}$, IEEE Trans. Appl. Supercon., Vol. 11, No. 1 (March 2001), pp. 3054-3057.

M. Lelovic, R. Koritala, B. L. Fisher, U. Balachandran; N. Vo, V. Selvamanickam, and P. Haldar (IGC-SuperPower), Novel Technique for Improving Field Dependence in Bi-2223 Superconducting Tapes at 77 K, IEEE Trans. on Applied Superconductivity, Vol. 11, No. 1, March 2001, pp. 3349-3352.

M. Li, B. Ma, Y. A. Jee, B. L. Fisher, and U. Balachandran, Structural and Electrical Properties of Biaxially Textured $YBa_2Cu_3O_{7-x}$ Thin Films on Buffered Ni-Based Alloy Substrates, Mat. Res. Soc. Symp. Proc. Vol. 659, High-Temperature Superconductors -- Crystal Chemistry, Processing and Properties, pp. II10.2.1-2.6 (2001), eds. U. Balachandran, H. C. Freyhardt, T. Izumi, and D. C. Larbalestier.

V. A. Maroni, R. M. Baurceanu, N. N. Merchant, A. K. Fischer, and R. D. Parrella, Phase Chemistry Considerations in the Processing of State-of-theArt Ag/Bi-2223 Composite Conductor, THERMEC '2000: CDROM, Section D1, Vol. 117/3, Special Issue: Journal of Materials Processing Technology, eds. T. Chandra, K. Higashi, C. Suryanarayana, and C. Tome, Elsevier, UK (2001).

V. A. Maroni, A. K. Fischer, and K. T. Wu, The Investigation of Phase Evolution in Composite Ceramic Superconductors Using Raman microscopy Techniques, Physica C 341-348, 657-658 (2000).

T. M. Mulcahy, J. R. Hull, K. L. Uherka; R. A. Abboud, and J. Juna (UNICOM), Test Results of 2-kWh Flywheel Using Passive PM and HTS Bearings, IEEE Trans. on Applied Superconductivity, Vol. 11, No. 1, March 2001, pp. 1729-1732.

N. M. Murphy, S. E. Dorris, D. J. Miller, Z. P. Luo, H. Claus, and V. A. Maroni, Phase Formation and Superconductivity in PIT-Type (Bi,Pb)-1212, Physica C 341-348, 657-658 (2000).

B. C. Prorok, J.-H. Park, K. C. Goretta, R. E. Koritala, U. Balachandran; and M. J. McNallan (U. of Illinois), Internally Oxidized Ag/1.2 at.% Mg Sheaths for Bi-2223 Tapes, IEEE Trans. on Applied Superconductivity, Vol. 11, No. 1, March 2001, pp. 3273-3276.

T. Puig, P. Rodrigues, Jr., A. E. Carillo, X. Obradors (Institut de Ciencia der Mater. de Barcelona, Spain); H. Zheng, U. Welp, L. Chen, H. Claus, B. W. Veal, and G. W. Crabtree, Self-Seeded YBCO Welding Induced by Ag Additives, Physica C 363, 75-79 (2001).

K. Salama (Texas Center for Superconductivity); S. P. Athur, and U. Balachandran, Texturing of REBCO Using Temperature Gradient, Physica C 357-360 (2001) 11-19.

V. Selvamanickam, G. Carota, M. Funk, N. Vo, P. Haldar (IGC-SuperPower); U. Balachandran, M. Chudzik; P. Arendt, J. R. Groves, R. DePaula, and B. Newnam (LASL), High-Current Y-Ba-Cu-O-Coated Conductor Using Metal Organic Chemical-Vapor Deposition and Ion-Beam-Assisted Deposition, IEEE Trans. on Applied Superconductivity, Vol. 11, No. 1, March 2001, pp. 3379-3381.

M. Tetenbaum, V. A. Maroni, N. M. Murphy, and S. E. Dorris, Phase Stability Domans of (Bi,Pb)-2223: Data Sources, Correlation, and Assessment, Physica C 341-348, 497-498 (2000).

T. G. Truchan, M. P. Chudzik, B. L. Fisher, R. A. Erck, K. C. Goretta, and U. Balachandran, Effect of Ion-Beam Parameters on In-Plane Texture of Yttria-Stabilized Zirconia Thin Films, IEEE Trans. on Applied Superconductivity, Vol. 11, No. 1, March 2001, pp. 3485-3488.

H. Zheng, H. Claus, L. Chen, A. P. Paulikas, B. W. Veal, B. Olsson, A. Koshelev, J. Hull, and G. W. Crabtree, Transport Current Measured in Ring Samples: Test of Superconducting Weld, Physica C 350, 17-23 (2001).

Distribution for ANL–02/03

Internal:

U. Balachandran
R. Baurceanu
Y. S. Cha
G. Crabtree
S. E. Dorris
H. Drucker
B. L. Fisher
F. Y. Fradin
K. C. Goretta
K. E. Gray
J. Harmon
J. R. Hull
J. Jorgensen
M. Kirk
S. Lake
M. Li
B. Ma
V. A. Maroni
D. J. Miller
J. J. Picciolo
R. B. Poeppel
A. C. Raptis
W. J. Shack
W. W. Schertz
J. P. Singh
A. M. Wolsky
TIS Files

External:

DOE–OSTI (2)
ANL–E Library
ANL–W Library

U.S. Department of Energy, Washington:

Office of Power Technologies, Energy Efficiency and Renewable Energy:
- W. Parks
- J. Daley
- R. K. Dixon
- R. George
- M. Reed
- H. Chhabra

Basic Energy Sciences–Materials Science:
- T. J. Fitzsimmons
- R. Gottschall
- B. Strauss
- A. Dragoo

Energy Technology Division Review Committee:
- H. K. Birnbaum, University of Illinois at Urbana–Champaign
- I.-Wei Chen, University of Pennsylvania
- F. P. Ford, Rexford, NY
- S. L. Rohde, The Peter Kiewit Institute
- H. S. Rosenbaum, Fremont, CA
- S. L. Sass, Cornell University
- R. Zoughi, University of Missouri-Rolla

Other – Industry – University

S. Ahmed, Southern California Edison, Rosemead, CA
J. Badin, Energetics, Inc., Columbia, MD
P. Barnes, Air Force Research Laboratory, Wright-Patterson Air Force Base
P. Berdahl, E. O. Lawrence Berkeley National Laboratory
J. Blais, Sentech, Inc., Bethesda, MD
R. Blaugher, National Renewable Energy Laboratory
R. W. Boom, University of Wisconsin – Madison
J. Cave, Hydro Quebec, Montreal, Canada
F. Chu, Ontario HydroTechnology, Toronto, Canada
P. Chu, University of Houston
J. Clem, Ames Laboratory
P. Clem, Sandia National Laboratories
B. Currie, Pacific Northwest National Laboratory
A. Day, Boeing Corp., Seattle, WA
D. Driscoll, Rockwell Automation, Cleveland, OH
M. Eddy, Superconductor Technologies, Inc., Santa Barbara, CA
J. Ekin, National Institute of Standards and Technology, Boulder, CO
N. Eror, University of Pittsburgh
D. K. Finnemore, Ames Laboratory
A. Funkenbusch, 3M, St. Paul, MN
J. R. Gaines, Jr., Superconductive Components, Inc., Columbus, OH
J. Gill, Energetics Inc., Columbia, MD
P. Grant, EPRI, Palo Alto, CA
D. Gubser, Naval Research Laboratory
P. Haldar, University at Albany, State University of New York
R. Hammond, Laboratory for Advanced Materials, Stanford University
R. A. Hawsey, Oak Ridge National Laboratory
P. Herz, TMS, Inc., Gaithersburg, MD
R. L. Hughey, Southwire Co., Carrollton, GA
Y. Iwasa, Francis Bitter National Magnet Lab., Massachusetts Institute of Technology
J. B. Ketterson, Northwestern University
M. Klein, University of Illinois at Urbana–Champaign
D. K. Kroeger, Oak Ridge National Laboratory
D. C. Larbalestier, University of Wisconsin – Madison
A. Lauder, DuPont, Wilmington, DE
M. Levine, E. O. Lawrence Berkeley National Laboratory
M. Levy, University of Wisconsin – Milwaukee
J. Lewis, University of Illinois at Urbana–Champaign
R. Loehman, Sandia National Laboratories
A. Malozemoff, American Superconductor Corp., Westborough, MA
F. Marciano, Pirelli Cables, Columbia, SC
K. Marken, Oxford Instruments, Inc., Carteret, NJ
B. McCallum, Ames Laboratory, Ames, IA

P. J. McGinn, University of Notre Dame
S. Mehta, Waukesha Electric Systems, Waukesha, WI
M. W. Morgan, Ability Engineering Technology, Inc., South Holland, IL
J. Muehlhauser, University of Tennessee
C. Oberly, Wright Air Force Laboratory, Dayton, OH
P. Pellegrino, IGC-SuperPower, Schenectady, NY
D. Peterson, Los Alamos National Laboratory
N. Phillips, E. O. Lawrence Berkeley National Laboratory
C. Rey, DuPont, Wilmington, DE
R. A. Roehl, Commonwealth Edison Co., Downers Grove, IL
C. H. Rosner, CardioMag Imaging, Inc., Schenectady, NY
R. Russo, Lawrence Berkeley National Laboratory
R. Schiferl, Reliance Electric, Cleveland, OH
H. Schneider-Muntan, National High Magnetic Field Laboratory, Tallahassee, FL
J. Schwartz, Florida State University
G. Smith, PSC, Inc., Woodinville, WA
M. Strasik, Boeing Corp., Seattle
M. Suenaga, Brookhaven National Laboratory
B. Weinberger, United Technologies Research Center, East Hartford, CT
D. O. Welch, Brookhaven National Laboratory
W. Wong-Ng, NIST
J. Worth, Oxford Instruments, Inc., Carteret, NJ
J. Wu, Westinghouse Electric Corp., Science and Technology Center, Pittsburgh